COMPUTATIONAL SILICON NANOPHOTONIC DESIGN

by

Bing Shen

A dissertation submitted to the faculty of
The University of Utah
in partial fulfillment of the requirements for the degree of

Doctor of Philosophy

Department of Electrical and Computer Engineering

The University of Utah

May 2017

The University of Utah Graduate School

STATEMENT OF DISSERTATION APPROVAL

The dissertation of **Bing Shen**

has been approved by the following supervisory committee members:

Rajesh Menon	, Chair	**09/21/2016** Date Approved
Ajay Nahata	, Member	Date Approved
Michael A. Scarpulla	, Member	**09/21/2016** Date Approved
Valentine Zeev Vardeny	, Member	**09/21/2016** Date Approved
Jordan Gerton	, Member	**09/22/2016** Date Approved

and by **Gianluca Lazzi** , Chair/Dean of

the Department/College/School of **Electrical and Computer Engineering**

and by David B. Kieda, Dean of The Graduate School.

ABSTRACT

Photonic integration circuits (PICs) have received overwhelming attention in the past few decades due to various advantages over electronic circuits including absence of Joule effect and huge bandwidth. The most significant problem obstructing their commercial application is the integration density, which is largely determined by a signal wavelength that is in the order of microns. In this dissertation, we are focused on enhancing the integration density of PICs to warrant their practical applications.

In general, we believe there are three ways to boost the integration density. The first is to downscale the dimension of individual integrated optical component. As an example, we have experimentally demonstrated an integrated optical diode with footprint 3×3 μm^2, an integrated polarization beamsplitter with footprint 2.4×2.4 μm^2, and a waveguide bend with effective bend radius as small as 0.65 μm. All these devices offer the smallest footprint when compared to their alternatives. A second option to increase integration density is to combine the function of multiple devices into a single compact device. To illustrate the point, we have experimentally shown an integrated mode-converting polarization beamsplitter, and a free-space to waveguide coupler and polarization beamsplitter. Two distinct functionalities are offered in one single device without significantly sacrificing the footprint. A third option for enhancing integration density is to decrease the spacing between the individual devices. For this case, we have experimentally demonstrated an integrated cloak for nonresonant (waveguide) and resonant (microring-resonator) devices.

Neighboring devices are totally invisible to each other even if they are separated as small as $\lambda/2$ apart.

Inverse design algorithm is employed in demonstrating all of our devices. The basic premise is that, via nanofabrication, we can locally engineer the refractive index to achieve unique functionalities that are otherwise impossible. A nonlinear optimization algorithm is used to find the best permittivity distribution and a focused ion beam is used to define the fine nanostructures.

Our future work lies in demonstrating active nanophotonic devices with compact footprint and high efficiency. Broadband and efficient silicon modulators, and all-optical and high-efficiency switches are envisioned with our design algorithm.

To my beloved wife, Yaqiong

TABLE OF CONTENTS

Chapters

ACKNOWLEDGEMENTS

I would first express the deepest appreciation to my committee chair Dr. Rajesh Menon, who leads me into the fantastic world of optics and photonics. The dissertation could not have been done without his professional guidance. Fruitful discussions with him were also the key to successfully finishing the dissertation. I was also inspired by his enduring endeavor in exploring the beauty of optics and photonics, which will definitely be a valuable treasure in my life.

Committee members including Dr. Ajay Nahata, Dr. Zeev Valentine Vardeny, Dr. Mike Scarpulla, Dr. Gordan Gerton are also greatly acknowledged. Their valuable suggestions on doing research and making presentations will be particularly beneficial to my future research.

I also give thanks to my lab members and friends at the University of Utah. I have also received kind help from the nanofab staff. Dr. Randy Polson helped me with the nanofabrication. Instrument training from Brian Baker, Steve Pritchett, Charles Fisher, Brian van Devener, and Tony Olsen is greatly appreciated as well.

Finally, special thanks are given to my family. It is the meticulous care and unending love from my wife, Yaqiong, that helps me get through the hard times in Utah. My baby, Austin, was born when I was working on the dissertation. He has been a great gift to me and makes my life more meaningful. Great thanks are given to my parents as well for their continuous and unconditional support.

CHAPTER 1

INTRODUCTION

Moore’s law, which is the observation that the number of transistors in a dense electronic integrated circuit (EICs) doubles approximately every two years, has been proven accurate over the past fifty years. However, recent advancements in the semiconductor industry make it even harder to follow Moore’s law, especially when the 14 nm transistor process has been commercially available and heat dissipation has been the most significant problem for EIC design. When the device dimension is down to 5-7 nm according Moore’s law, which means it consists of a few atoms, whether it can be still called a “device” is worth serious consideration.

In order to overcome the bottleneck of EICs, photonic integration circuits (PICs) are now a promising candidate, receiving overwhelming attention from researchers both in academic institutes and companies. A photonic integrated circuit (PIC) is defined as a device that integrates multiple (at least two) photonic functions and as such is similar to an electronic integrated circuit. The major difference between the two is that PICs perform functions of signals imposed on optical wavelength typically in the range of 850 nm to 1650 nm. They are considered a promising alternate to EICs due to various advantages over EICs. The first and most important issue relates to the radiation heat. In EICs, the radiation heat is proportional to the operation frequency, which imposes a serious limit on the overall operation speed of EICs. In addition, the heavy radiation heat means that an advanced and bulky heat dissipation mechanism is necessary, which also imposes a cap on the integration density. However, this should no longer be a problem in PICs since optical PICs never radiate heat in principle. This is a huge advantage and means that integration circuits with larger integration density and free from heat dissipation mechanisms can be envisioned. The second advantage is the potentially much higher bandwidth. All these advantages enable PICs' promise in data communications [1], biosensing [2], nonlinear optics [3], novel light sources [4], and so on.

1.1 Photonic integration circuits and CMOS

Complementary metal–oxide–semiconductor (CMOS) is a mature technology that achieved great success in constructing integration circuits. It would be counterintuitive that the same foundry and process for electronic circuits can be used build chips that can generate, detect, modulate, and otherwise manipulate light. The electronic industries have spent billions of dollars to develop tools, processes, and facilities without considering their compatibility with photonics. It would be very lucky and cost-effective if photonics are compatible with CMOS [5].

As a matter of fact, CMOS cannot be directly used in photonics. Previous attempt to directly integrate photonic functionalities into CMOS or bipolar silicon wafers, without making any process changes, has yielded poor-performance devices. The current CMOS technology that is developed for electric circuit fabrication is actually not necessary to be compatible with silicon photonic circuits. Even if photonic chip fabrication is compatible with CMOS, it would not make economic sense. State-of-art CMOS process is now for 14nm transistors, while the feature size of photonic components is typically in the order of microns largely determined by the optical wavelength. There is no economic reason the sophisticated and expensive CMOS process is directly used to fabricate photonic chips.

Although there is no reason to envision that the electronic device fabrication process is compatible with silicon photonic circuits, it was found in a later investigation that silicon is an ideal platform for electronics and photonics and CMOS could be a promising candidate for the mass production of photonic circuit through rearranging the process flow and applying minor modification to the fabrication process to meet the particular requirement of photonic circuits. As a result, a modern semiconductor foundry that was used for the fabrication of electronic circuits could achieve mass production of photonic circuits. IME and Global Foundry are good examples.

1.2 Inverse design

In a generalized optical problem there are three parts: input, system, and output, which is illustrated in Figure 1.1. The input signal can be any kind of waves including plane wave, Gaussian wave, their combinations, etc. The optical system can be devices enabled by the traditional optical phenomena including refraction, reflection, diffraction, absorption, etc. The input wave is the processed optical input signal in the optical system.

As a result, all the optical problems fall into three categories. Forward problems, where output is derived given the known input signal and optical system; Inverse problem Type I, where the input is reversely derived given the known optical system and output signal; Inverse problem Type II, where the optical system is derived given the known input and output signal. In all our discussions throughout the dissertation, we concentrate on inverse problem Type II that we call inverse nanophotonic design.

Typically, most of the inverse nanophotonic designs fall into two categories. One is called gradient-deepest object-first inverse design, where the gradient of the topology change is derived using Green’s functions and the search proceeds to the deepest gradient to arrive at the optimized design that best matches the design object predefined. In this approach, typically a few iterations can generate a satisfying design [6,7]. However, this is not an explicit design algorithm since heavy physics is involved in the algorithm and gray area with artificial refractive index not readily achieved in reality exist in the final design that requires tricky strategy to map to a practical design. The other category employing stochastic algorithms (i.e., simulated annealing, genetic algorithm) to arrive the optimized design. The design process involves negligible physics and can be readily adapted to any regimes besides nanophotonics, although heavy calculations are needed [8]. In the following discussions, we focus on the second category due to its explicitness and versatility. In general, our devices are discretized into hundreds of pixels, each having two possible states: silicon and air. Direct binary-search (DBS) optimization is used to toggle the pixels between the two states to push the figure-of-merit (FOM) predefined. Finite-difference time-domain (FDTD) is used to evaluate the FOM of each structure. The details of our design algorithm including the DBS algorithm and FDTD settings are detailed in the second chapter.

1.3 Outline

The dissertation is outlined as follows. In the first chapter, we give a brief introduction of the background of photonic integration circuits including its landscape and fabrication. A brief introduction of inverse design is shown here.

Chapter 2 gives details of the design and experiments. The detailed design flow chart is given. And then the direct binary-search optimization and particle swarm optimization we used in our design process is carefully explained. Device fabrication steps are detailed as well. We also give a description of the characterization procedure and measurement setup for most of our devices mentioned in this dissertation.

In Chapter 3, we demonstrated nanophotonics-based metamaterials for efficient free-space-to-waveguide coupling applying the nonlinear optimization algortihm. Three couplers were designed, fabricated and characterized. The first device couples incident light into a multimode waveguide, the second device couples incident light into a single-mode waveguide directly, and the third device couples and separates two orthogonal polarizations into two multimode waveguides. All devices offer comparable or higher coupling efficiencies, are easier to fabricate, and demonstrate higher bandwidth when compared to conventional devices. Furthermore, each device is at least an order of magnitude smaller in area than previously reported devices.

In Chapter 4, broadband, efficient, all-dielectric metamaterial waveguide bends (MWBs) that redirect light by 180 degrees are experimentally demonstrated. The footprint of each MWB is 3 μm × 3 μm and redirection is achieved for single-mode waveguides spaced by 1.3 μm, which corresponds to an effective bend radius of 0.65 μm ($<\lambda_0/2$ for $\lambda_0 = 1.55$ μm). The designed and measured transmission efficiencies are >80% and ∼70%, respectively. Furthermore, the MWBs have an operating bandwidth >66 nm (design) and >56 nm (experiments).

In Chapter 5, two silicon based integrated optical diodes are experimentally demonstrated and each one works for a single polarization state. Both devices offer comparable, if not higher than, transmissions and extinction ratios with the footprint 3 μm × 3 μm, when compared to alternatives. In addition, a polarization-insensitive integrated optical diode is shown as well.

In Chapter 6, we report the use of nanophotonic cloaking to render neighboring devices invisible to one another, which allows them to be placed closer together than is otherwise feasible. Specifically, we experimentally demonstrated waveguides that are spaced by a distance of $\sim\lambda_0/2$ and designed waveguides with center-to-center spacing as small as 600nm ($<\lambda_0/2.5$). Our experiments show transmission efficiency >-2dB and extinction ratio

>15dB over bandwidth >60nm. This performance can be improved with better design algorithms and improved fabrication.

In Chapter 7, we report a silicon based integrated nanophotonic polarization beamsplitter with footprint 2.4 by 2.4 μm^2. An averaged transmission over both polarization states of ~70% is experimentally confirmed, which is ~10% lower than the theoretical value of ~80%. Furthermore, a mode-converting polarization beamsplitter that offers the combined function of mode conversion and polarization separation is demonstrated as well.

In Chapter 8, we demonstrate broadband asymmetric transmission or optical-diode behavior via a digital metasurface, that is, a surface that is digitally patterned at subwavelength dimensions. Enhanced light-matter interactions at the interfaces of the metasurface break the symmetry in the propagation direction, and enables high light-transmission in one direction, while strongly reflecting the light in the opposite direction. We measured a peak extinction ratio of 11.18 dB and peak forward transmission efficiency of 74.3% at the design wavelength of 1.55 μm. The operational bandwidth of the device was 201 nm. We further designed, fabricated, and experimentally characterized a digital metasurface that enables polarization-independent optical-diode behavior, which we believe is the first device of its kind.

In Chapter 9, we show a multilevel metamaterial linear polarizer that rotates light with polarization perpendicular to its principal axis by 90 deg. Light with polarization parallel to its principal axis is transmitted undisturbed. Thereby, such a polarizer is able to output linearly polarized light from unpolarized input with a transmission efficiency that is substantially higher than the theoretical upper limit of 50%. We experimentally confirmed that the fabricated device enhances the transmission of the desired linear polarization by 100% compared to an unpatterned film, corresponding to a transmission efficiency of ~74% at the design wavelength.

The dissertation concludes with Chapter 10. A short summary of our previous work in silicon based integrated optics and free-space optics is presented. Furthermore, metamaterials based active integrated nanophotonic devices (i.e., modulator and switch) are also envisioned.

1.4 References

[1] A. Argyris, M. Hamacher, K. Chlouverakis, A. Bogris, and D. Syvridis, "Photonic integrated device for chaos applications in communications," Phys. Rev. Lett. **100**, 194101 (2008).

[2] J. Hu, X. Sun, A. Agarwal, and L. C. Kimerling, "Design guidelines for optical resonator biochemical sensors," J. Opt. Soc. Am. B **26**, 1032–1041 (2009).

[3] M. A. Foster, A. C. Turner, M. Lipson, and A. L. Gaeta, "Nonlinear optics in photonic nanowires," Opt. Express **16**, 1300 (2008).

[4] R. E. Camacho-Aguilera, Y. Cai, N. Patel, J. T. Bessette, M. Romagnoli, L. C. Kimerling, and J. Michel, "An electrically pumped germanium laser," Opt. Express **20**(10), 11316–11320 (2012).

[5] M. Hochberg, N. Harris, R. Ding, Y. Zhang, A. Novack, C. Xuan, and T. Baehr-Jones, "Silicon photonics: The next fabless semiconductor industry," IEEE J. Solid-State Circuits **5**, 48 (2013).

[6] J. Lu and J. Vučković, "Nanophotonic computational design," Opt. Express **21**(11), 13351–13367 (2013).

[7] A. Y. Piggott, J. Lu, K. G. Lagoudakis, J. Petykiewicz, T. M. Babinec, and J. Vučković, "Inverse design and demonstration of a compact and broadband on-chip wavelength demultiplexer," Nat. Photonics **9**, 374 (2015).

[8] B. Shen, R. C. Polson and R. Menon, "Metamaterial-waveguide bends with effective bend radius $< \lambda_0/2$," Opt. Lett. **40**(24) 5750-5753 (2015).

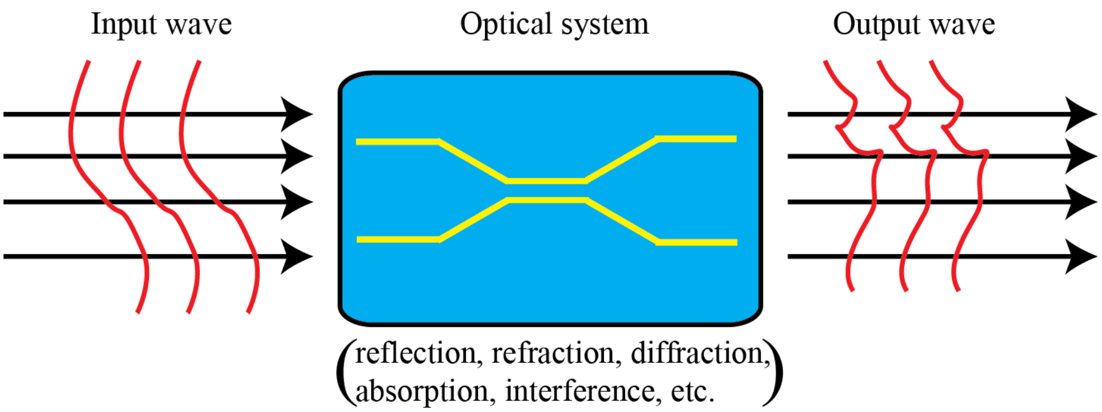

Figure 1.1. A typical optical signal processing model, including input, output and system.

CHAPTER 2

DESIGN AND EXPERIMENT

Let’s take the polarization beamsplitter we have designed and demonstrated as illustrated in Figure 2.1 to detail our design process. We first specify the dimension of the device we are trying to achieve, 2.4 by 2.4 μm^2 for our case. The device area is then discretized into hundreds of pixels, each sized 120 by 120 nm^2. For each pixel, there are two possible states, silicon denoted as “1” and air, where silicon is totally etched away, denoted as “0.” Direct binary-search (DBS) coupled with particle swarm optimization (PSO) is used to toggle the pixel states to maximize the predefined figure-of-merit (FOM). For our case, the figure-of-merit can be transmission, extinction ratio, or a combination of the two. FOM is evaluated with the finite-difference time-domain (FDTD) method. DBS and PSO exhibits the complimentary characteristics: DBS tends to arrive at premature convergence but with a few iterations; PSO is much more likely to arrive at global maximum at the cost of iterations. For our case, DBS is first used to generate a local maximum which serves as one of the initial agents of PSO. We then employ PSO to look for the global maximum via exploring a much larger search space. Both the two optimization algorithms work in an iteration fashion. For one iteration, we pick one pixel to toggle its state and FOM evaluated. The perturbation is kept if FOM is improved, otherwise discarded. A proper termination condition (e.g., maximum iterations or a particular number of changes between two subsequent iterations) is imposed to ensure convergence.

Since heavy computation is needed, Amazon’s cloud service is employed. An elastic cluster is constructed to accommodate different applications. As a result, we could possibly design devices of any size without significantly sacrificing the runtime.

Details of optimizations, device modeling and fabrication, and characterization procedures are as follows.

2.1 Optimization algorithm

2.1.1 Direct binary-search optimization

In order to solve our nonlinear problem, a direct binary search (DBS) algorithm is employed. It is well known that DBS has been employed to design holograms [1], light-trappings in solar cells [2-4], non-imaging optics [5], and integrated optics [6,7]. There are many stochastic optimization algorithms available (i.e., simulated annealing, and genetic optimization). DBS is selected for our particular case due to its simplicity and fast convergence.

The flow chart of DBS is shown as Figure 2.2. We first define initial states for all the pixels as the starting point for DBS. The starting point can be either randomly selected or predefined with intuition or physics. DBS works in an iteration fashion and one iteration ends when all the pixels are addressed. For one iteration, we first pick one pixel and toggle to its opposite state, and the FOM is evaluated. The perturbation is kept if the FOM is improved, otherwise discarded. And then the search proceeds to the next pixel until all the pixels are addressed. The order of the pixel to be toggled is determined by a random sequence, previously generated. For pixels with multiple states, both positive and negative perturbations are applied. Appropriate termination condition is applied to ensure convergence. Several different termination conditions are available for various conditions. One possible termination condition can be that the improvement of FOM is less than the predefined threshold. An alternate termination condition is that the number of pixel state change in three consecutive iterations is less than three or two. In addition, DBS is reported to be sensitive to the starting point and we repeat the optimization with several distinct starting points and pick one optimized result with the highest FOM.

2.1.2 Particle swarm optimization

As mentioned earlier, The DBS algorithm is tentative to converge to a local maximum and the possibility of encountering the global maximum is increased by careful selecting the starting point and running multiple independent optimizations simultaneously. For most of our designs, 10 independent optimizations were run simultaneously and we selected the design with the highest efficiency for experimental verification. The transmission efficiency is typically acceptable to demonstrate the proof-of-principle. In order to further approach the global maximum, Particle Swarm Optimization (PSO) is incorporated in the design algorithm to explore the limit of the insertion loss. PSO was first proposed by Eberhart et al. through simulating the social behavior of flying birds [8]. Each individual, called a particle, adjusts its flight according to both its own and its neighbor' flying experiences. The position of a particle is updated via the following equation,

$$x_{i,d} = x_{i,d} + v_{i,d} \cdot \Delta t \tag{1}$$

$$v_{i,d} = \varpi_n \cdot v_{i,d} + c_1 \cdot rand() \cdot \left(p_{i,d} - x_{i,d} \right) + c_2 \cdot rand() \cdot \left(g_{i,d} - x_{i,d} \right) \tag{2}$$

where $x_{i,d}$ is the i^{th} particle's position in the d^{th} dimension of the parameter space, and $v_{i,d}$ is the corresponding velocity. w_n is the inertial weight for n^{th} iteration and determines how likely the particle stays on its old velocity. $p_{i,d}$ and $g_{i,d}$ are individual and global best positions, respectively. c_1 and c_2 are two positive constants, and determine how much a particle is influenced by the memory of its own best position and the global best position, respectively. For our case, a large inertial weight is used to traverse most of the design space and finally a smaller inertial weight is employed for convergence. As DBS and PSO exhibits the distinct properties, that is DBS tends to converge to a local maximum with a few iterations and PSO is much more likely to converge to the global maximum but with several hundreds of iterations, we first use DBS to quickly arrive at a local maximum, which serves as the initial position of one of the particles for PSO to further improve the design. It is found that PSO typically converges with less than 20 iterations, much faster than optimization solely based on PSO that typically exhibits hundreds of iterations. The flow chart of DBS coupled with the PSO optimization algorithm is shown in Figure 2.3.

2.2 Fabrication

All of our devices are fabricated on a silicon-on-insulator (SOI) wafer. The device thickness is in the range of 250 nm to 300 nm and the thickness of the buried oxide layer is 3 μm. Although electron beam lithography would be the most promising candidate for our devices with feature size ~100 nm, we do not have access to such a tool and have to develop our own procedures with tools available at hand. Basically, we adopt a two-step fabrication procedure. Generally, we first use Heidelberg μPG101 with 3 μm resolution to make the larger structures, including input/output multimode waveguide interfacing the fiber. The second step comes with a focused ion beam for the fabrication of fine nanostructures with feature size 100nm. The detailed fabrication procedures are as follows.

1. Spin coat **HMDS 60 sec @ 6000 rpm** as an adhesion layer on the SOI wafer, and then leave in fume hood for **10 min** to evaporate.
2. Spin coat Shipley 1813 photoresist **60 sec @ 4000 rpm**. *(Recipe details: (1) dispense Shipley 1813 at* ***30 rpm*** *for* ***6 sec*** *with* ***10 rpm/sec*** *ramp; (2) spin at* ***500 rpm*** *for* ***5 sec*** *with* ***100 rpm/sec*** *ramp; (3) spin at* ***4000 rpm*** *for* ***45 sec*** *with* ***1000 rpm/sec*** *ramp).*
3. Soft bake on hotplate **1 min @ 110°C**
4. Leave in air for **10 min** for dehydration

5. Exposure by Heidelberg μPG 101. *(Detailed recipe: 1 X 1 mode, bidirectional mode, waveguides are* ***15 mm*** *long; dose is* ***10 mW*** *with duty cycle* ***65%)***
6. Development in **AZ 1:1** developer for **1 min**
7. Rinse with DI water for **2 min** and dry with **N_2**
8. RIE etch the sample with Oxford 100. The etching gas is a mixture of SF_4 and C_4F_8 with a flow rate of 40 ccm and 17.5 ccm, respectively. SF_4 is used to etch the top silicon layer and C_4F_8 is used for passivation in order to get smooth side walls.
9. Strip off photoresist with **Acetone** and **O_2** plasma.
10. Definition of fine nanostructures with Felios65 dual-beam focused ion beam. The ion beam accelerating voltage was 30 kV and the beam current used was 7.7 pA with fluence of 800 C/m^2.

2.3 Characterization

The characterization is summarized in Figure 2.4. Figure 2.4 illustrates the measurement system and panels (B)-(E) show the on-chip polarizer used in characterization. The on-chip polarizer employed here is a pretty straightforward one that consists of a straight waveguide with a vertical air slot near the center of the waveguide. The center of the air slot exhibits a 70 nm offset with regard to the center of the waveguide. The measurement process is as follows.

First, we bypass the optical components within the dotted frame by connecting the lensed fiber in the output path to the detector directly. The lensed fiber in the input path is moved to the on-chip polarizer. The polarization state of the input light is selected by rotating the polarization controller 1 (PC1) and monitoring the received power. The on-chip polarizer allows the TM mode to pass through efficiently while blocking the light of the orthogonal polarization state as illustrated in Figure 2.4 (d)-(e). As a result, the TM input mode is selected by maximizing the power detected and TE is selected by minimizing the power.

Second, the input lensed fiber is moved to a straight waveguide without any pattern on the sample and the optical components within the dotted frame is inserted to the output path. We rotate the polarization controller 2 (PC2) in the output path to align the polarization plane of the output light with that of the polarizer.

Third, we move the input lensed fiber to the cloak. The polarization components of the output light are measured via rotating the polarizer correspondingly.

2.4 Mechanism analysis

As mentioned above, the scatters of interest are typically in the size of ~100 nm, which are far smaller than the wavelength (1550 nm). Light is treated as electromagnetic waves instead of a bundle of rays, in which case refraction and interference are involved. Basics of interference and diffraction are first revisited before presenting the possible way to explain our devices.

2.4.1 Interference and diffraction

Let us consider a region in space where two waves pass through at the same time. In this case a two-dimensional (2D) region is assumed. The net displacement is simply the vector sum of the individual displacements. Interference is the combination of two or more diffraction patterns. On the other hand, if no bending occurs, the light waves continue to form a composite wave. The general idea of interference is illustrated in Figure 2.5. The superposition of the waves exhibits a maximum and minimum when a particular phase difference is met, which are named constructive and destructive interference, respectively.

Another property of light we should encounter in our device is diffraction, which is the bending of waves as they pass by an object, also called a scatterer. The phenomena can be explained via *Huygens's law* which states that every unobstructed point on a wavefront will act as a source of secondary spherical waves. The new wavefront is the surface tangent to all the secondary spherical waves. The light propagation based on Huygens's law is illustrated in Figure 2.6.

2.4.2 Preliminary explanation

For our devices discussed below, the interactions between waveguide modes and silicon pillars size of ~100 nm are dominant. In order to gain some insight into the physics of our devices, the interaction between a monochromatic plane wave and a symmetric cylinder is first analyzed as a simple case. In the following analysis, we assume an *x*-polarized incident wave with an amplitude E_0 and propagation constant β_0 traveling in the *z* direction, then the incident wave can be expressed as:

$$\overrightarrow{E}_{inc} = E_0 e^{i\beta_0 z} x. \tag{2.1}$$

Employing proper boundary conditions for the dielectric cylinder, the interaction between the incident wave and the cylinder scatterer is governed by Maxwell's equation:

$$\begin{gathered} \nabla \times \left(\nabla \times \overrightarrow{E} \right) = \omega^2 \varepsilon_{x,y} \mu \overrightarrow{E} \\ \varepsilon_{x,y} = \begin{cases} \varepsilon, x^2 + y^2 < r^2 \\ \varepsilon_m, x^2 + y^2 \geq r^2 \end{cases}. \end{gathered} \tag{2.2}$$

By assuming that an arbitrary wave can be represented by a linear combination of characteristic vector functions, the scattered electric field can be derived from the equations mentioned above:

$$\vec{E}_{scat} = \frac{k_m}{\omega^2 \varepsilon_m \mu} \sum \left[A_{l,m} a_l \vec{M}_{l,m} + B_{l,m} b_l \vec{N}_{l,m} \right]. \tag{2.3}$$

Here, $\vec{N}_{l,m}$ and $\vec{M}_{l,m}$ are the vector spherical harmonics, a_l and b_l are the scattering coefficients. $A_{l,m}$ and $B_{l,m}$ are the expression coefficient which is characteristic for a particular incident beam and expressed as:

$$A_{l,m} = \int M_{l,m}^{*} \vec{E}_{inc} d\Omega$$

$$B_{l,m} = \int N_{l,m}^{*} \vec{E}_{inc} d\Omega. \tag{2.4}$$

Above mentioned is the analytical solution for a monochromatic plane wave normal incident on a cylinder scatterer.

However, our case is much more complicated since the input mode is the eigenmode of silicon waveguide that can not be assumed as a plane wave. The incident beam can be expressed as:

$$\vec{E}_y = \mathrm{Re} \sum_{m=1}^{\infty} \sum_{n=1}^{\infty} \left(A_{mn}^{+} e^{-j\beta_{mn} y} + A_{mn}^{-} e^{j\beta_{mn} y} \right) \sin\left(\frac{m\pi}{a} \mathrm{x} \right) \sin\left(\frac{n\pi}{\varpi} z \right) e^{j\omega t} y \tag{2.5}$$

Here a TM case is shown as an example. Applying the similar case mentioned above, we could in principle get the expression for scattered wave by a rectangle silicon pixel. However, with the complicated expression for the input modes and the geometry of the scatterer, the analytical solution is tricky to derive. Instead, we use a numerical method (finite-difference time-domain) to derive a scattered electric field from a silicon pillar illuminated by the fundamental mode (both TE and TM) of the silicon waveguide (shown in Figure 2.7).

As shown in Figure 2.7, the scattered field can be represented by a combination of semispherical harmonics. According to Huygens's law, the scattered field that is a combination of semispherical harmonics can be considered as the new source that illuminates the following scatterers. Again, with Maxwell's equation and the given epsilon distribution of the following scatterers, we could derive the new scattered field. Under such iteration fashion, we could in principle analytically derive the scattered field pattern after a series of scatters with complicated geometries. As a result, we could in principle tailor the geometries of the scatterers to achieve a particular scattered field and thus enable devices of unique functionalities.

To gain a better understanding of our devices, we take the example of our integrated polarization beamsplitter, the geometry of which is shown in Figure 2.8. As shown here, the silicon pillars in the red dashed rectangle directly interact with the mode from the silicon waveguide. We may consider the four silicon/air pillars as the first scatterer to excite light in the fine nanostructures. Based on the epsilon distribution of the scatterer, the expressions of the input waveguide mode, and Maxwell's equations, we could in principle get the analytical expression of the scattered field. However, solving the equation is not simple and again we numerically get the scattered field pattern from the first scatters, which is shown in Figure 2.9.

Compared to the scattered field from a single pillar, the scattered field from the first four silicon/air pillars is somewhat distorted, particular in the region immediately near the scatterer. The field away from the scatterer can also be considered as a combination of semispherical harmonics. The scattered field then can be considered as the new source for the silicon/air pillars that surround the first scatterer. In an iteration fashion, we can finally derive the scattered field after the entire nanostructures.

Above mentioned shows a blueprint of how we can analytically explain our devices in an iteration fashion to get the scattered field from the total nanostructures. However, due to the complexity of the problem, the analytical expression is difficult to derive now, which should be the focus of future work.

2.5 Numerical modeling

In this part, details of the numerical model and the assumption made are presented. The model is illustrated in Figure 2.10. The top view and cross-section of the simulation region are shown in Figure 2.10 (a) and (c), respectively. Perfect matching layers (PML) are implemented to surround the structure in X, Y, and Z directions, which represents the free-space. The dispersion relations of silicon and silica used in our model are shown in Figure 2.10 (b). The absorption of silicon and silica is ignored in our case since they exhibit negligible absorption in the wavelength of interest (1550 nm), which is one of the approximations in our simulation model. Maxwell's equation is implemented throughout the simulation region. Finite-difference time-domain (FDTD) is used to numerically solve Maxwell's equation. A uniform mesh grid is used. In this case, it is assumed that the electric field is constant all through one mesh cube and the electric field can be represented by the value right in the center of the cube. As a result, the derivative in Maxwell's equation could be represented by the division. This is the second approximation in our model, which is also the fundamental assumption in FDTD. The fundamental TE and TM modes for silicon waveguide of this particular geometry, which are calculated through MPB [9], serves as the input.

In conclusion, the features of the simulation model can be summarized as: (1) Only Maxwell's equation are implemented in the simulation model with no other approximation; (2) materials used are normal dielectric material without nonlinearity; (3) two assumptions are made including: (i) The absorption of silicon and silica is sufficiently small to be neglected; (ii) the electric field within one mesh cube is constant and can be represented by that in the center of the cube.

2.6 References

[1] M. A. Seldowitz, J. P. Allebach, and D. W. Sweeny, “Synthesis of digital holograms by direct binary search,” Appl. Opt. **26**, 2788 (1987)

[2] P. Wang and R. Menon, “Optimization of generalized dielectric nanostructures for enhanced light trapping in thin-film photovoltaics via boosting the local density of optical states,” Opt. Express **22**(S1), A99–A110 (2014).

[3] P. Wang and R. Menon, “Optimization of periodic nanostructures for enhanced light-trapping in ultra-thin photovoltaics,” Opt. Express **21**(5), 6274–6285 (2013).

[4] B. Shen, P. Wang, and R. Menon, “Optimization and analysis of 3D nanostructures for power-density enhancement in ultra-thin photovoltaics under oblique illumination,” Opt. Express **22**(52) A311-A319 (2014).

[5] Ganghun Kim and R. Menon, “An ultra-small 3D computational microscope,” Appl. Phys. Lett. **105**, 061114 (2014).

[6] B. Shen, R. C. Polson, and R. Menon, “Metamaterial-waveguide bends with effective bend radius < $\lambda_0/2$,” Opt. Lett. **40**(24) 5750-5753 (2015).

[7] B. Shen, P. Wang, R. C. Polson and R. Menon, “Integrated metamaterials for efficient, compact free-space-to-waveguide coupling,” Opt. Express **22**(22) 27175-27182 (2014).

[8] J. Kennedy and R. Eberhart, "Particle swarm optimization," Proc. IEEE Int. Conf. Neural Netw. **4**, 1942 (1995).

[9] MIT Photonic-Bands (MPB) package that is a free program for computing the band structures (dispersion relations) and electromagnetic modes. http://ab-initio.mit.edu/wiki/index.php/MIT_Photonic_Bands

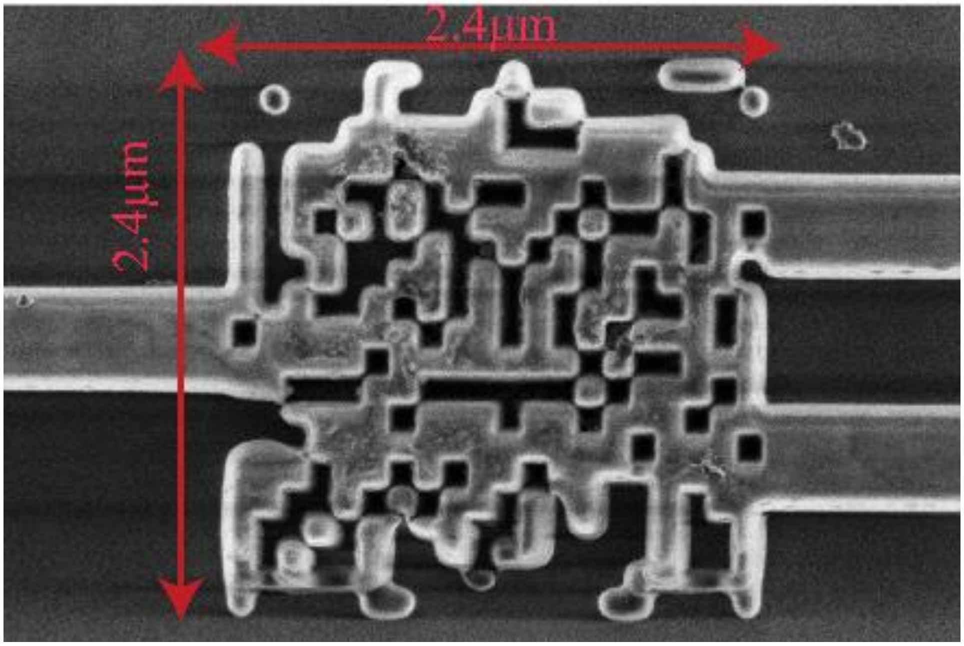

Figure 2.1. Scanning electron micrograph of an integrated SOI based polarization beamsplitter.

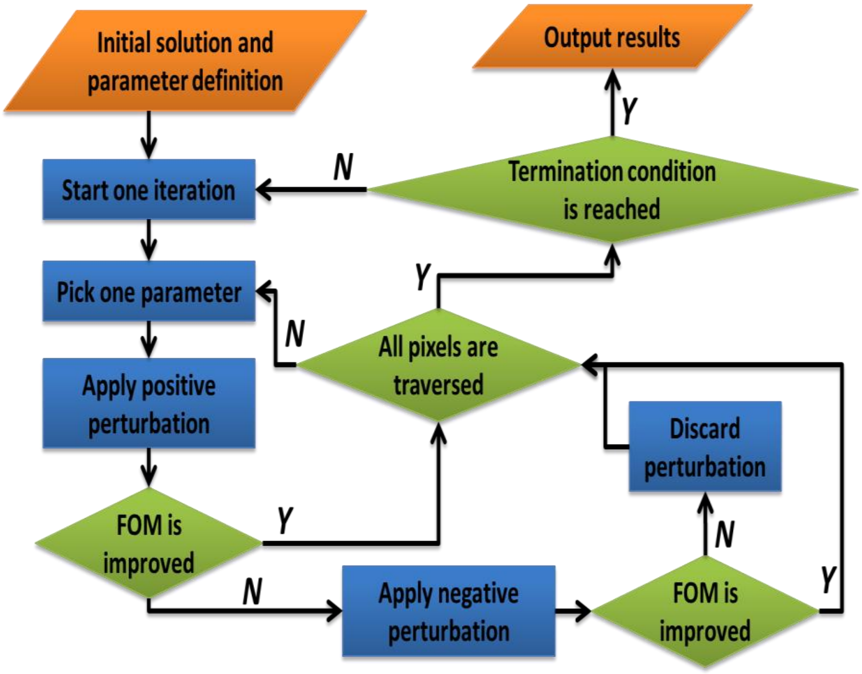

Figure 2.2. Flow chart of the DBS algorithm.

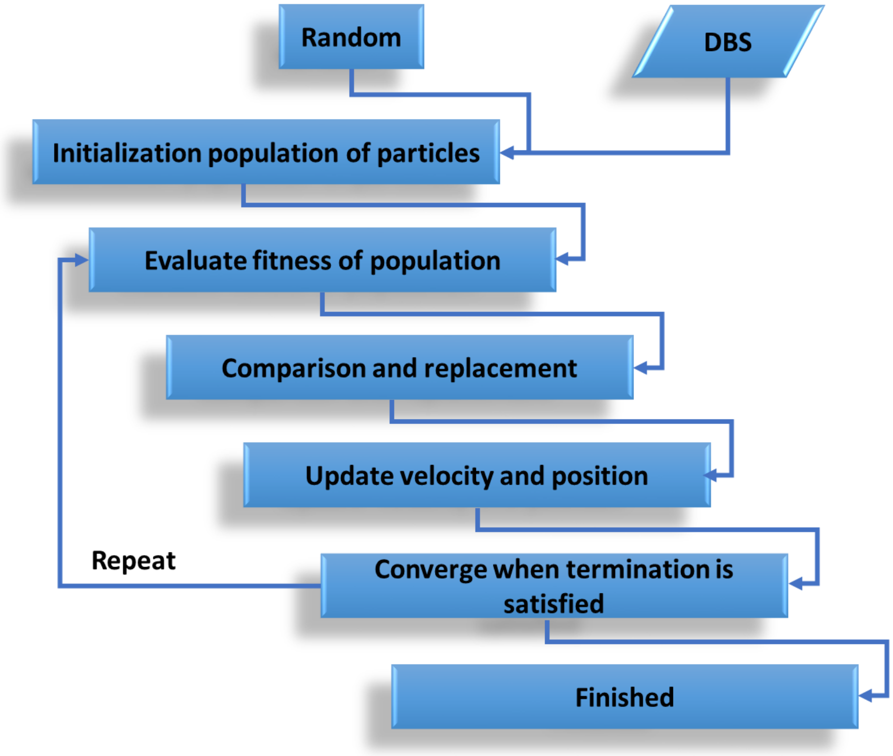

Figure 2.3. Flow chart of the DBS coupled with PSO optimization algorithm.

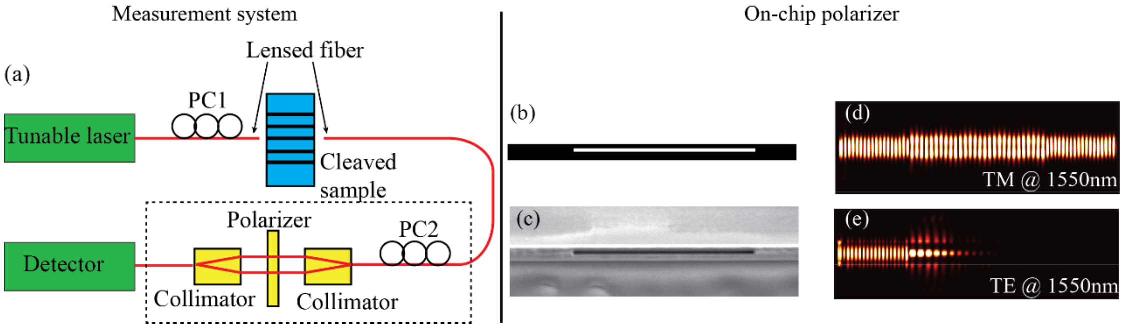

Figure 2.4. Characterization. (a) Measurement system. (b) Design and (c) Scanning-electron micrographs (SEM) of the on-chip polarizer. Steady-state field intensity pattern of (d) TM and (e) TE mode for the on-chip polarizer.

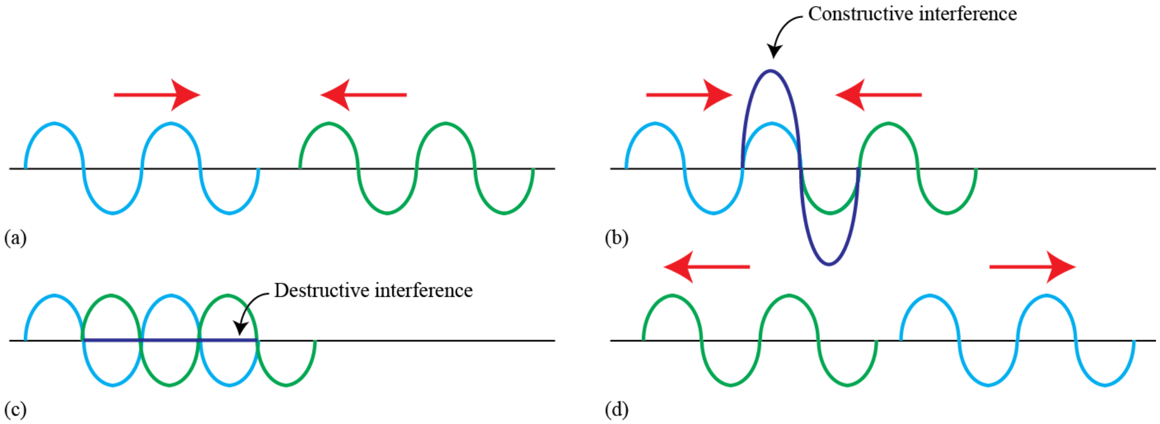

Figure 2.5. Superposition of waves. (b) Constructive interference, and (c) destructive interference. Light blue and green lines illustrate constituent waves, while dark blue shows the resulting wave.

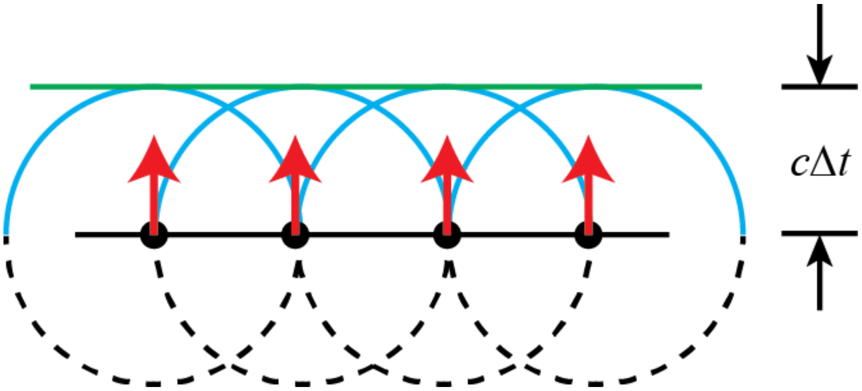

Figure 2.6. Propagation of wave based on Huygens’s law.

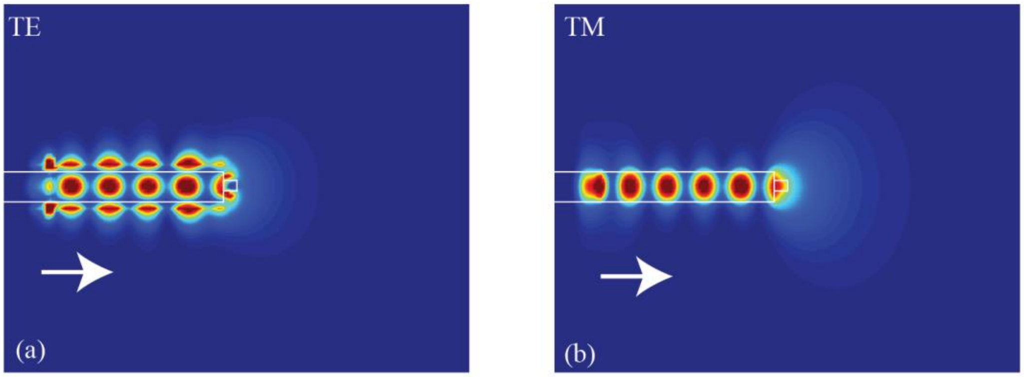

Figure 2.7. Time-averaged electric field pattern for a silicon pillar illuminated by (a) TE and (b) TM mode from a silicon waveguide. The white lines show the profile of the geometry. The white arrows indicate the light propagation direction.

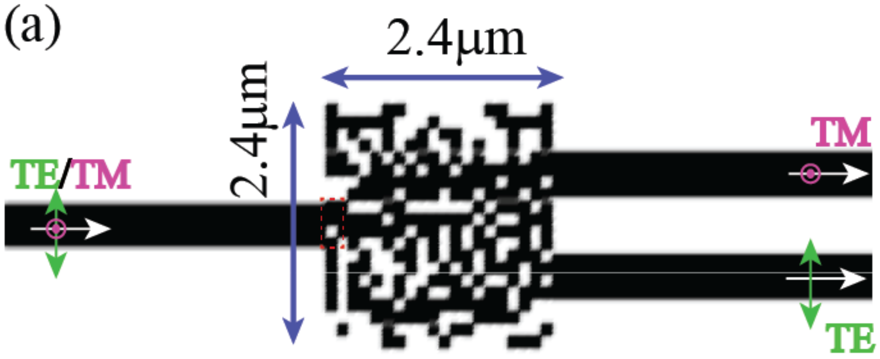

Figure 2.8. Epsilon distribution of an integrated polarization beamsplitter. The pixels within the red dashed rectangle represent the first scatterer that directly interacts with the mode from the silicon waveguide.

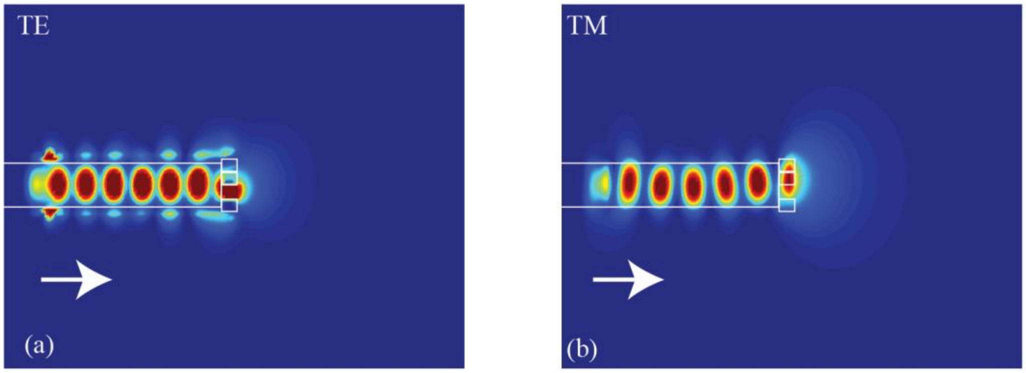

Figure 2.9. Time-averaged electric field pattern for the first four silicon pillars of integrated polarization beamsplitter illuminated by (a) TE and (b) TM mode from a silicon waveguide. The white lines show the profile of the geometry. The white arrows indicate the light propagation direction.

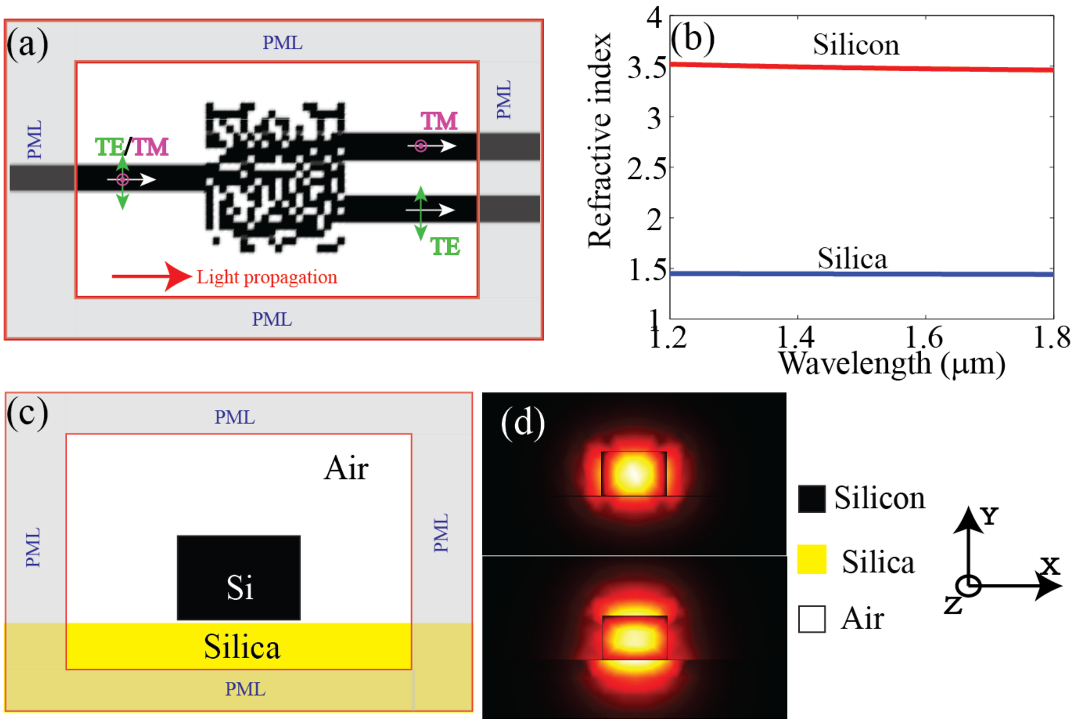

Figure 2.10. Numerical model. (a) Top view and (c) cross-section of the simulation model. (b) Dispersion relations of silicon and silica used in the model. (d) Fundamental modes of silicon waveguide for TE and TM.

CHAPTER 3

EFFICIENT, COMPACT FREE-SPACE-TO-WAVEGUIDE COUPLER

Reprinted and adapted with permission from [B. Shen, P. Wang, R. C. Polson, and R. Menon, “Integrated metamaterials for efficient, compact free-space-to-waveguide coupling,” Opt. Express 22(22) 27175-27182 (2014).]. ©2014 Optical Society of America.

3.1 Abstract

We applied nonlinear optimization to design nanophotonics-based metamaterials for efficient free-space-to-waveguide coupling. Three devices were designed, fabricated, and characterized. The first device couples incident light into a multimode waveguide, the second device couples incident light into a single-mode waveguide directly, and the third device couples and separates two orthogonal polarizations into two multimode waveguides. All devices offer comparable or higher coupling efficiencies, are easier to fabricate, and demonstrate higher bandwidth when compared to conventional devices. Furthermore, each device is at least an order of magnitude smaller in area than previously reported devices. The highly efficient single-mode waveguide-coupler is a unique device that has not been experimentally demonstrated before. We further performed careful simulations to underscore the tolerance of these devices to fabrication errors. Their robustness is primarily a result of the large number of coupled guided-mode resonances that are responsible for each device performance.

3.2 Introduction

Silicon on insulator (SOI) is a promising material for high-density photonic-integrated circuits because of the large refractive-index contrast. However, coupling light from free space onto a photonic chip is highly inefficient. This is primarily due to the large area-mismatch between the free-space mode from an optical fiber (~78 μm^2) and that in an SOI waveguide (~0.125 μm^2). Furthermore, in order to match the momentum of the wave vectors, subwavelength diffractive structures are required. Several methods have been proposed to solve this problem [1–16]. Among them, the subwavelength grating coupler has arguably been the most successful [6]. Various types of grating couplers, including dual grating-assisted directional coupling [9], metal mirrors [10,16], distributed-Bragg reflectors (DBRs) [11], and apodized gratings [12–15], have been proposed to increase the coupling efficiency. The highest coupling efficiency of a grating coupler reported is −0.62 dB and the size of this device is 15 μm × 15.2 μm [16]. However, this device required a separate backside metal mirror, which complicates the fabrication process. Furthermore, the standard grating couplers require a separate aligned lithography and etching step, since the depth of the grating is typically smaller than that of the waveguides themselves. Related forms of mode converters with coupling efficiency of −0.5 dB have also been proposed [1,3]. However, these devices are very large (a few hundred micrometers in length), which greatly limit their applicability in integrated photonics. In addition to that, shallow etching is employed, which means that two-step etching process is employed.

Free-form metamaterials offer a new degree of design freedom, which can enable unique and efficient integrated-photonic applications in a very compact area [17]. The basic premise of this approach is that via nanofabrication, one can control the local refractive index of the device. By spatial engineering of the refractive index, it is possible to design devices such as the free-space-to-waveguide coupler with much higher performance that is otherwise possible.

3.3 Methods

In this paper, we design, fabricate, and characterize three metamaterial couplers. In each device, the input is normally incident from out of plane. The output is coupled into one or more waveguides. All devices are designed for λ_0 = 1550nm and are fabricated on a SOI substrate with a silicon thickness of 300nm and an oxide thickness of 3 μm. The first device is illustrated in Figure 3.1(a). This device is comprised of 30 × 30 square pixels, each of size 100 nm × 100 nm, resulting in a total device area of 3 μm × 3 μm. Linearly polarized (electric field along Y) incident light is coupled into the multimode waveguide (width = 3 μm) with a simulated efficiency of −0.65 dB, only slightly lower than the best reported efficiency to date for such a device. The simulated time-averaged intensity distribution is shown in Figure 3.1(b). The field distributions seem to indicate that the mode coupling is primarily enabled by the excited guided-mode resonances in the structures. The refractive index variation introduced by the metamaterial coupler creates a perturbation of the incoming wave front. As a result, multiple guided-mode resonances are excited so as to match the wave vectors of the waveguide-propagation modes. In Figure 3.1(a), the white regions represent air, where the silicon has been etched away (black regions represents unetched silicon) and the etch depth is the same as the depth of the waveguide, 300nm. In other words, the device can be fabricated at the same time as the waveguides, and a separate lithography and etch step is no longer required. Note that in the previous best device, the grating is shallower than the waveguide, necessitating a separate aligned lithography and etch step [16]. Furthermore, the previous best device also requires a backside metal mirror, which is not required in our device.

The second device is illustrated in Figure 3.1(c). Normally incident linearly polarized (electric field along Y) light is coupled directly into a single-mode waveguide (width = 400nm) as illustrated by the simulated time-averaged intensity distribution in Figure 3.1(d). This device exhibits a simulated coupling efficiency of -3dB, which is far higher than the efficiency reported previously [19]. The device reported in ref [19] requires a gold grating and is substantially larger than our device. A theoretical design was also previously described with a coupling efficiency of about -3dB [18]. However, this design is extremely challenging to fabricate due to the required continuous contours. In conventional integrated photonics, a very long adiabatic taper (millimeters in length) is required to do mode conversion from a multimode to a singlemode waveguide [8]. The third device shown in Figure 3.1(e) is a combined coupler and polarization splitter. The incident light is again normally incident but is comprised of two orthogonal polarizations. The device couples one polarization into one multimode waveguide and the other polarization into the second multimode waveguide, as illustrated by the simulated time-averaged intensity distributions in Figures. 3.1(f) and 1(g) for Ex and Ey polarizations, respectively. The simulated coupling efficiency averaged over both polarizations for this device is -1.5 dB, which is higher than that for a comparable device reported previously (~ -3.2 dB) [17]. In conclusion, employing our method, we could either shrink the footprint of conventional devices with minor penalty on the efficiency, or achieve novel functions.

3.4 Experiments

Our devices are fabricated on a silicon-on-insulator (SOI) wafer with a silicon thickness of 300 nm. Although the devices could be patterned using a single lithography and etch step, since we do not have access to a tool that has the requisite resolution over millimeter-sized areas, we opted for a two-step fabrication process. We first used the Heidelberg MicroPG 101 (laser pattern generator) to pattern the 3μm-wide waveguide patterns in positive photoresist (Shipley 1813) deposited on top of the silicon layer. The exposure power was 10mW at 65% duration factor and bi-directional mode was employed. Standard 352B developer was used to develop the photoresist for 1min. Then, an Oxford 100 reactive-ion etcher (RIE) was used to etch the silicon. The gas was a mixture of SF_6 with a flow rate of 40 ccm and C_4F_8 with a flow rate of 17.5 ccm. SF_6 is used for etching the silicon, while C_4F_8 is used for passivation during etching in order to get straight sidewalls. For our sample, the total etch time was 240 seconds that corresponds to an etch rate of 1.25 nm per second. Then, we used the dual-beam focused-ion-beam (FEI, Helios 650) system to define the metamaterial couplers, the single-mode waveguide and any associated tapers. The metamaterial couplers have a minimum feature size of 100 nm. The ion beam accelerating voltage was 30 kV for all devices. For the metamaterial couplers, the beam current used was 7.7 pA with fluence of 800 C/m^2. Alignment marks were used to ensure that the metamaterial couplers were appropriately aligned with the waveguides. We also fabricated reference devices with conventional grating couplers for comparison with the metamaterial couplers [22]. The reference grating coupler was etched to a shallower depth (80nm) using the FIB and the corresponding beam current was 24 pA with a fluence of 220 C/m^2.

Since all output light measurements were performed using butt-coupling, we also designed and fabricated a 4μm-long taper from the single-mode waveguide (for the device in Figure 3.1(c)) to a 3μm-wide multi-mode waveguide. Scanning-electron micrographs of the 3 devices are shown in Figures 3.2(a)–3. 2(c). The measured sizes of the pixels in the metamaterials devices range from 95 nm to 110 nm.

For measurement, we used a fiber-coupled laser with center wavelength of 1550 nm. The light output from a fiber collimator was normally incident on each metamaterial coupler. The mode-field diameter of the collimated beam is 0.9 mm. The output light was measured by butt-coupling from a multi-mode waveguide (width = 3μm) using a lensed fiber. A polarizer was used at the input to check the response of the device for each polarization separately. The reference device was comprised of a waveguide of width =

3μm and the same overall length as the waveguides used with the metamaterial couplers. The reference grating coupler had a period of 700 nm, duty cycle of 50% and an etch depth of 80nm [22]. The reference coupler was fabricated using FIB but a lower dose was used compared to the metamaterial couplers. An incident angle of ~8° was used for the reference grating coupler as this configuration achieved the highest coupling efficiency [23]. We measured the output power from the metamaterial couplers relative to the reference grating coupler. Then, we used the simulated coupling efficiency spectrum of the reference device to estimate the absolute coupling efficiencies of the metamaterial devices. Furthermore, for the single-mode coupler, we accounted for the taper loss via simulations. The resulting experimental and simulated coupling efficiencies as a function of the incident wavelength are plotted in Figures 3.3(a)-3.3(c) for the 3 devices in Figures 3.2(a)-3.2(c), respectively.

The measured efficiencies are slightly lower than the expected values, but otherwise agree well overall. The discrepancies are likely due to the fabrication errors and edge roughness in the devices. These can be mitigated in the future by optimizing the patterning and etching processes. The ripples in the measured efficiencies are likely due to the Fabry-Perot resonance between light reflection from the fiber and that from the fabricated devices. Nevertheless, we measured peak-coupling efficiencies of −1.25 dB and −3.9 dB for the multi-mode and single-mode couplers, respectively. The measured peak-coupling efficiencies for the coupler/polarization splitter device are −1.97 dB for Ex and −2.63 dB for Ey, respectively.

3.5 Discussion

From the simulated efficiency plot in Figure 3.3(a), we can estimate the 1dB bandwidth of the device as 64 nm (1519 nm to 1583 nm). The 1 dB bandwidth for the free-space to single-mode coupler is 49 nm (1527 nm to 1576 nm). In the case of the polarization-separating coupler, the 1dB bandwidth is 56 nm (1524 nm to 1574 nm) for Ex and 55 nm (1519 nm to 1574 nm) for Ey. In comparison, the previous best grating coupler exhibits a 1 dB bandwidth of ~40 nm [16]. Our devices exhibit a larger bandwidth due to the fact the mechanism of multiple coupled guided modes is responsible for the coupling. The multiple resonances enable the device to be less sensitive to wavelength shifts. In contrast, with single resonant-mode devices (like the conventional grating couplers), a small shift in wavelength will result in mode-mismatch and severely lower coupling efficiency. Therefore, adjusting the tilt angle of the fiber is needed to correct any wavelength shift. The dispersion data for silicon used in the simulations is taken from ref [24].

We also numerically investigated the robustness of our designs to fabrication errors. Specifically, we varied the thickness of the device (determined by the etch depth of the pixels). The resulting coupling efficiency plots are shown in Figures 3.3(d)–3.3(f) for the 3 devices, respectively. As expected, the efficiencies drop as the device thickness changes from the design value of 300nm. If we are able to tolerate an efficiency drop of 20% from the peak value, we can determine the appropriate specification for variation in device thickness. This allowable thickness variation is 59 nm (−20 nm to + 39 nm) for the free-space to multi-mode coupler, 63 nm (−25 nm to + 38 nm) for the free-space to single-mode coupler and 67 nm (−27 nm to + 40 nm) for the coupler/polarization-splitter. In addition, we used simulations to study the impact of the alignment error between the waveguides and the couplers. We conclude that a 100 nm alignment error results in ~0.3 dB drop of the coupling efficiency for each polarization state.

We also simulated the time evolution of the electric fields within this device in order to visualize the performance of the device. The input plane wave is normally incident on each device as discussed earlier. Due to the subwavelength structures within each device, evanescent modes are excited. These evanescent modes act in a concerted fashion and give rise to multiple resonant modes that are propagating in the plane of the device. The multiple resonant modes result in mode excitation in the output waveguide. The geometry of each metamaterial coupler is optimized to enhance the overall power transfer from the incident light into the appropriate output waveguide.

3.6 Conclusion

We designed metamaterial couplers that efficiently redirect light from free-space into integrated waveguides using a novel extension of the direct-binary-search algorithm. The algorithm is able to incorporate fabrication constraints, which results in practical and error-tolerant devices. The devices themselves are compatible with conventional optical lithography used to manufacture CMOS devices, and the coupler thickness is the same as the waveguide thickness. Due to the limitations of the tools available to us, we used a combination of optical lithography and focused-ion-beam lithography to fabricate our devices. We characterized the devices and experimentally demonstrated coupling efficiencies of −1.25 dB for a free-space to multi-mode waveguide coupler, −3.9 dB for a free-space to single-mode waveguide coupler and −1.97 dB and −2.63 dB for a free-space to multi-mode waveguide coupler and polarization splitter for Ex and Ey polarizations, respectively. The efficiency of each device is at least comparable to, if not larger than that of previously reported devices. This is achieved even though our devices are considerably smaller than the previous ones. In addition, our devices demonstrate higher bandwidths and better robustness to fabrication errors. Our design technique is readily extended to many other standard and unique passive integrated-photonic devices and can be applied to not only enhance efficiency but also increase the device-integration density and functionality.

3.7 References

[1] T. Shoji, T. Tsuchizawa, T. Watanabe, K. Yamada, and H. Morita, “Low loss mode size converter from 0.3 μm square Si wire waveguides to singlemode fibers,” Electron. Lett. **38**(25), 1669–1670 (2002).

[2] S. McNab, N. Moll, and Y. Vlasov, “Ultra-low loss photonic integrated circuit with membrane-type photonic crystal waveguides,” Opt. Express **11**(22), 2927–2939 (2003).

[3] N. Fang, Z. Yang, A. Wu, J. Chen, M. Zhang, S. Zou, and X. Wang, “Three-dimensional tapered spot-size converter based on (111) silicon-on-insulator,” IEEE Photon. Technol. Lett. **21**(12), 820–822 (2009).

[4] M. Pu, L. Liu, H. Ou, K. Yvind, and J. M. Hvam, “Ultra-low-loss inverted taper coupler for silicon-on-insulator ridge waveguide,” Opt. Commun. **283**(19), 3678–3682 (2010).

[5] R. Takei, M. Suzuki, E. Omoda, S. Manako, T. Kamei, M. Mori, and Y. Sakakibara, “Silicon knife-edge taper waveguide for ultralow-loss spot-size converter fabricated by photolithography,” Appl. Phys. Lett. **102**(10), 101108 (2013).

[6] D. Taillaert, W. Bogaerts, P. Bienstman, T. F. Krauss, P. Van Daele, I. Moerman, S. Verstuyft, K. De Mesel, and R. Baets, “An out-of-plane grating coupler for efficient butt-coupling between compact planar waveguides and single-mode fibers,” IEEE J. Quantum Electron. **38**(7), 949–955 (2002).

[7] D. Taillaert, W. Bogaerts, and R. Baets, “Efficient coupling between submicron SOI-waveguides and singlemode fibers,” in *Proceedings of Symposium IEEE/LEOS Benelux Chapter, Enschede, The Netherlands* (IEEE, 2003), pp. 289–292.

[8] W. Bogaerts, D. Taillaert, B. Luyssaert, P. Dumon, J. Van Campenhout, P. Bienstman, D. Van Thourhout, R. Baets, V. Wiaux, and S. Beckx, “Basic structures for photonic integrated circuits in silicon-on-insulator,” Opt. Express **12**(8), 1583–1591 (2004).

[9] G. Z. Masanovic, G. T. Reed, W. Headley, B. Timotijevic, V. M. Passaro, R. Atta, G. Ensell, and A. G. Evans, “A high efficiency input/output coupler for small silicon photonic devices,” Opt. Express **13**(19), 7374–7379 (2005).

[10] F. Van Laere, G. Roelkens, M. Ayre, J. Schrauwen, D. Taillaert, D. Van Thourhout,

T. F. Krauss, and R. Baets, “Compact and highly efficient grating couplers between optical fiber and nanophotonic waveguides,” J. Lightwave Technol. **25**(1), 151–156 (2007).

[11] S. K. Selvaraja, D. Vermeulen, M. Schaekers, E. Sleeckx, W. Bogaerts, G. Roelkens, P. Dumon, D. Van Thourhout, and R. Baets, “Highly efficient grating coupler between optical fiber and silicon photonic circuit,” in Conference on Lasers and Electro-Optics, Baltimore, Maryland (2009), CTuC6.

[12] X. Chen, C. Li, C. K. Fung, S. M. Lo, and H. K. Tsang, “Apodized waveguide grating couplers for efficient coupling to optical fibers,” IEEE Photon. Technol. Lett. **22**(15), 1156–1158 (2010).

[13] A. Mekis, S. Gloeckner, G. Masini, A. Narasimha, T. Pinguet, S. Sahni, and P. De Dobbelaere, “A grating coupler-enabled CMOS photonics platform,” IEEE J. Sel. Top. Quantum Electron. **17**(3), 597–608 (2011).

[14] A. Mekis, S. Abdalla, D. Foltz, S. Gloeckner, S. Hovey, S. Jackson, Y. Liang, M. Mack, G. Masini, M. Peterson, T. Pinguet, S. Sahni, M. Sharp, P. Sun, D. Tan, L. Verslegers, B. P. Welch, K. Yokoyama, S. Yu, and P. M. De Dobbelaere, “A CMOS photonics platform for high-speed optical interconnects,” in *Proceedings of IEEE Photonics Conference* (IEEE, 2012), pp. 356–357.

[15] C. Zhang, J.-H. Sun, X. Xiao, W.-M. Sun, X.-J. Zhang, T. Chu, J.-Z. Yu, and Y.-D. Yu, “High efficiency grating coupler for coupling between single-mode fiber and SOI waveguides,” Chin. Phys. Lett. **30**(1), 014207 (2013).

[16] W. S. Zaoui, A. Kunze, W. Vogel, M. Berroth, J. Butschke, F. Letzkus, and J. Burghartz, “Bridging the gap between optical fibers and silicon photonic integrated circuits,” Opt. Express **22**(2), 1277–1286 (2014).

[17] J. Lu and J. Vučković, “Nanophotonic computational design,” Opt. Express **21**(11), 13351–13367 (2013).

[18] F. Van Laere, T. Claes, J. Schrauwen, S. Scheerlinck, W. Bogaerts, D. Taillaert, L. O’Faolain, D. Van Thourhout, and R. Baets, “Compact focusing grating couplers for silicon-on-insulator integrated circuits,” IEEE Photon. Technol. Lett. **19**(23), 1919–1921 (2007).

[19] G. Kim, J.-A. Dominguez-Caballero, H. Lee, D. J. Friedman, and R. Menon, “Increased photovoltaic power output via diffractive spectrum separation,” Phys. Rev. Lett. **110**(12), 123901 (2013).

[20] P. Wang and R. Menon, “Optimization of generalized dielectric nanostructures for enhanced light trapping in thin-film photovoltaics via boosting the local density of optical states,” Opt. Express **22**(S1), A99–A110 (2014).

[21] B. Shen, P. Wang, and R. Menon, “Optimization and analysis of 3D nanostructures

for power-density enhancement in ultra-thin photovoltaics under oblique illumination," Opt. Express **22**(S2), A311–A319 (2014).

[22] X. Wang, W. Shi, S. Grist, H. Yun, N. A. F. Jaeger, and L. Chrostowski, "Narrow-band transmission filter using phase-shifted bragg gratings in SOI waveguide," in *Proceedings of IEEE Photonics Conference* (IEEE, 2011), pp. 869–870.

[23] Y. Li, D. Vermeulen, Y. De Koninck, G. Yurtsever, G. Roelkens, and R. Baets, "Compact grating couplers on silicon-on-insulator with reduced backreflection," Opt. Lett. **37**(21), 4356–4358 (2012).

[24] Refractive index for silicon and silica, http://refractiveindex.info/.

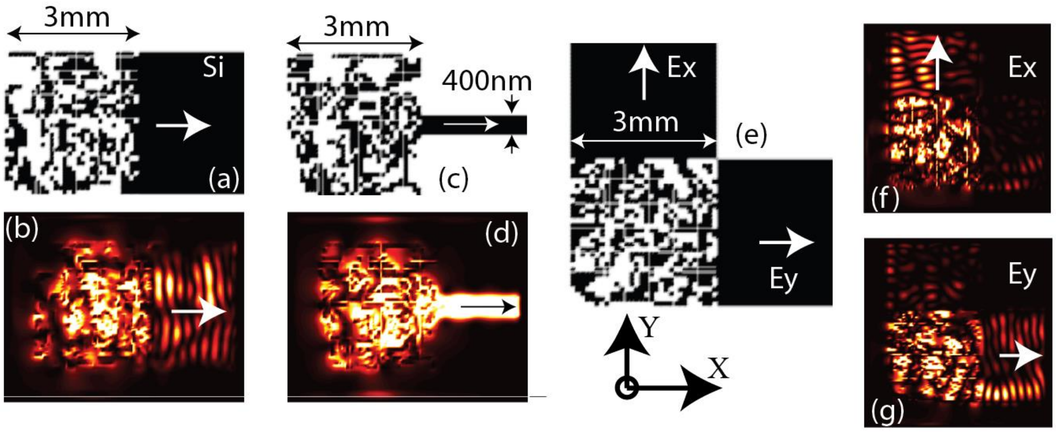

Figure 3.1. Metamaterial coupler designs. (a) Free-space to multimode waveguide coupler and (b) corresponding simulated time-averaged intensity distribution. (c) Free-space to single-mode waveguide coupler and (d) corresponding simulated time-averaged intensity distribution. (e) Free-space to multimode waveguide coupler and polarization splitter. Simulated time-averaged intensity distribution for light polarized along X and that polarized along Y are shown in (f) and (g), respectively. For (b) and (d), light is linearly polarized along Y-axis, while for (f) and (g), light is randomly polarized. In all cases, λ_0 = 1550 nm and light is normally incident from out of the plane of the figure. The arrows represent direction of light propagation in the waveguides.

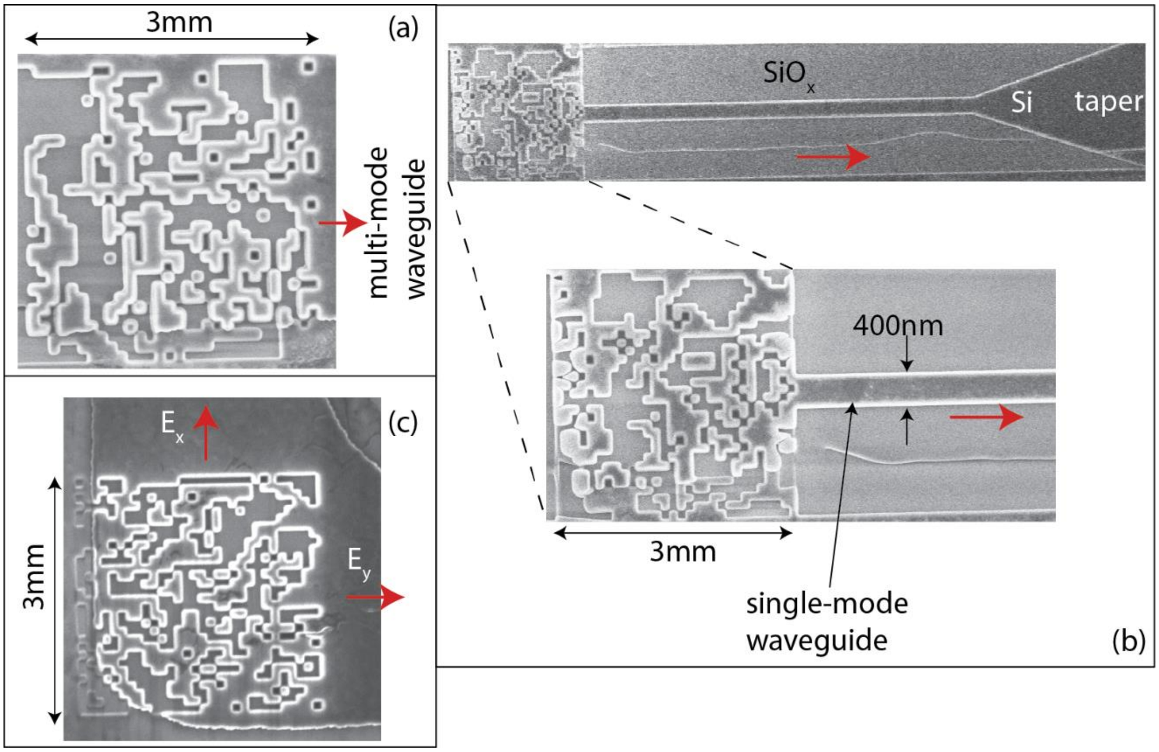

Figure 3.2. Scanning-electron micrographs of fabricated devices. (a) Free-space to multimode waveguide coupler. (b) Free-space to single-mode waveguide coupler. Note the taper from single-mode to multimode waveguide to facilitate butt coupling in order to measure the output. (c) Free-space to multimode waveguide coupler and polarization splitter. Red arrows indicate the direction of coupled (output) light flow.

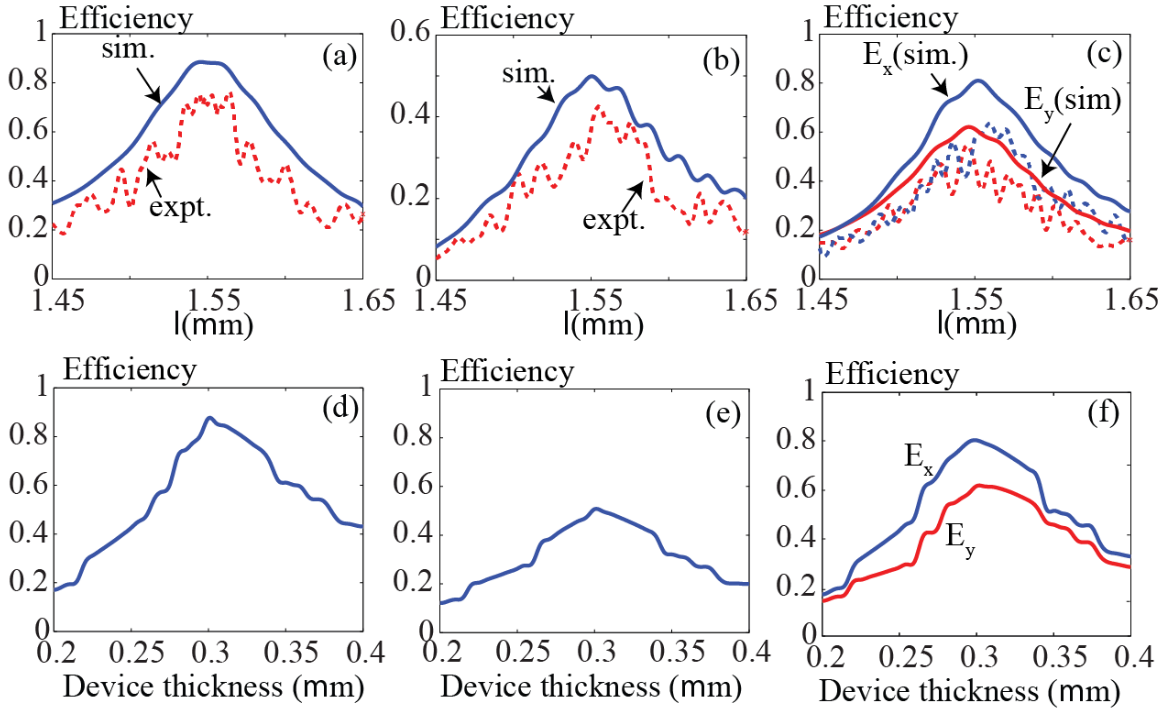

Figure 3.3. Measured (expt.) and simulated (sim.) efficiencies of (a) free-space to multimode coupler, (b) free-space to single-mode coupler and (c) free-space to multimode coupler and polarization splitter. In (c), the X and Y polarizations are shown in blue and red, respectively. In all plots, the simulation and experimental data are shown using solid and dashed lines, respectively. Simulated efficiencies as a function of the device thickness for (d) free-space to multimode coupler, (e) free-space to single-mode coupler and (f) free-space to multimode coupler and polarization splitter.

CHAPTER 4

METAMATERIAL-WAVEGUIDE BENDS WITH EFFECTIVE BEND-RADIUS < $\lambda_0/2$

Reprinted and adapted with permission from [B. Shen, R. C. Polson, and R. Menon, “Metamaterial-waveguide bends with effective bend radius < $\lambda_0/2$,” Opt. Lett. **40**(24) 5750-5753 (2015).]. ©2015 Optical Society of America.

4.1 Abstract

We designed, fabricated, and characterized broadband, efficient, all-dielectric metamaterial-waveguide bends (MWBs) that redirect light by 180 deg. The footprint of each MWB is 3 μm × 3 μm and redirection is achieved for single-mode waveguides spaced by 1.3 μm, which corresponds to an effective bend radius of 0.65 μm ($<\lambda_0/2$ for $\lambda_0 =$ 1.55 μm). The designed and measured transmission efficiencies are >80% and ∼70%, respectively. Furthermore, the MWBs have an operating bandwidth >66 nm (design) and >56 nm (experiments). Our design methodology that incorporates fabrication constraints enables highly robust devices. The methodology can be extended to the general routing of light in tight spaces for large-scale photonic integration.

4.2 Introduction

Ferrying optical signals in complex geometric configurations in the plane of a photonic-integrated circuit (PIC) is critical for many applications. It is notoriously difficult to execute sharp turns efficiently using conventional waveguides. Many methods have been proposed previously to realize sharp waveguide bends by exploiting plasmonics [1–8], photonic crystals [9–18], metamaterials [19,20] and microring resonators [21,22]. Both two-dimensional (2D) [1,3–8] and three-dimensional (3D) [2] plasmonic waveguide bends have been numerically shown. Unfortunately, these devices suffer not only from large ohmic losses from metals, but their fabrication is challenging because several alternating metal and dielectric layers are required [3–8]. Waveguide bends based on photonic crystals can exhibit large transmission efficiency. However, the footprint of such devices is very large because photonic crystals exhibit insufficient localization of the electromagnetic waves [9–18]. Furthermore, the coupling efficiency between the conventional silicon ridge waveguide and the photonic-crystal waveguide is typically low. Reflectionless waveguide bends using epsilon-near-zero (ENZ) effects enabled by metamaterials were previously demonstrated in the microwave regime [20]. However, ENZ effects require features that are smaller than $\lambda/30$, which makes fabrication very challenging at the infrared wavelengths for silicon photonics. Silicon microring resonators are also capable of achieving sharp and efficient waveguide bends [21,22]. Xu et al. demonstrated a silicon microring resonator with a radius as small as 1 μm but with a quality factor Q>1000 [21]. The Q-factor translates into bending losses per 180 deg bend of less than 1% and ~20% when the radius scales down to that of our case - 0.65 μm. However, one critical problem with these devices is that their bandwidths are typically less than 1 nm. Furthermore, they are very sensitive to fabrication errors and, therefore, additional compensating mechanisms are required. In addition to these, alternative methods enabling sharp waveguide bends have also been proposed [23,24]. Using a silver mirror, Ishida et al. achieved a 180-deg-bend structure over an area of ~100 μm × 300 μm with a transmission efficiency of ~35% [23]. The facet of the mirror has to be ultrasmooth to minimize scattering losses, which complicates the fabrication. Qian et al. realized a low-loss, 90-deg bend using an air trench filled with SU-8, which exhibits a footprint of tens of microns [24].

Free-form metamaterials offer a new approach to designing compact and power efficient integrated-photonic devices [25]. By nanostructuring a dielectric (silicon in our case) with features that are smaller than the wavelength, it is possible to engineer the device response to input electromagnetic waves in a manner that allows the device to be much smaller than is otherwise impossible. We have previously applied this idea to ultraefficient polarizers [25], light-trapping structures for solar cells [26], polarization beam splitters

[27], and other integrated-photonic devices [28–30]. The inverse design approach, by structuring silicon with subwavelength structures, has been discussed previously [11,14,16,31]. However, there are some notable advantages for our method. Some previous work is mostly based on periodic patterns (photonic crystals) [11,14], which makes these devices rather large compared with ours. Second, our methodology utilizes discrete topology, which improves the robustness of our devices [31].

4.3 Methods

In this Letter, we apply our principle to a 180-deg, metamaterial-waveguide bend (MWB) with an effective bend radius of only 650 nm for $\lambda_0 = 1550$ nm, while still maintaining transmission efficiency of >80% (simulation) and ~70% (experiments). Specifically, we designed, fabricated, and measured two MWB devices, one for each polarization state as illustrated in Figure 4.1. In both devices, linearly polarized light that is launched in the input waveguide [bottom waveguide as shown in Figures 4.1(a) and 4.1(b)] is coupled to the output waveguide [top waveguide as shown in Figures 4.1(a) and 4.1(b)] with a 180-deg bend facilitated by the MWB. Both devices were designed for $\lambda_0 =$ 1550 nm and were fabricated on a silicon-on-insulator (SOI) substrate. In Figures 4.1(a) and 4.1(b), the black regions represent silicon (Si), while white regions represent air where the Si is etched away. The simulated steady-state, electric-field intensity patterns for the two devices are shown in Figures 4.1(c) and 4.1(d). An ensemble of evanescent modes is excited within each MWB, which, in turn, excites the fundamental mode in the output waveguide. The calculated transmission efficiency at $\lambda_0 = 1550$ nm is 84% and 86% for TE and TM, respectively. In comparison, a simple semicircle bend would result in transmission efficiencies of only 13% and 14% for TE and TM, respectively. The epsilon distribution of the semicircle waveguide bend and the simulated steady-state intensity patterns for TE and TM at $\lambda = 1550$ nm are shown in Figure 4.2. Note that each MWB is only 3 μm × 3 μm and corresponds to an effective bend radius of only 650 nm.

The MWBs were designed using nonlinear optimization, and the design process has been described previously [27–30]. The 3 μm by 3 μm device is discretized into 30 × 30 pixels and the figure of merit for optimization is the transmission efficiency.

4.4 Experiments and results

Our devices are fabricated as explained in our previous publications [27–30]. The substrate is a SOI wafer with silicon thickness of 250 nm and buried oxide thickness of 3 μm. The devices and the single-mode waveguides were patterned using a FEI Helios NanoLab 650 dual-beam focused-ion-beam (dbFIB). The accelerating voltage was 30 kV and the beam current was 7.7 pA with fluence of 800 $\mathrm{C/m^2}$. To facilitate butt coupling and measurements, larger waveguides were patterned using laser-scanning lithography. Appropriate tapers were added to mate the larger waveguides to the single-mode waveguides using focused-ion-beam lithography. Alignment marks were used in order to ensure that the patterns generated by the two lithography processes were correctly aligned with each other. Note that the devices can be patterned using a single optical lithography step. Since we do not have access to the appropriate tools, we chose the two-patterning-step process.

Scanning-electron micrographs of the two devices are shown in Figures. 4.2(a) and 4.2(b). A closer look at the micrographs reveals that the devices are a little overetched because the color of the bottom of air pillars is not the same as that of the surrounding oxide. We further confirmed this by creating a through section and imaging it. The overetching is due to the fact that FIBL is not very selective to etching silicon compared to silicon oxide. As a result, we also numerically investigated the devices' sensitivity to silicon thickness in the following discussion.

The measurement system is illustrated in Figure 4.2(c), and the procedure is identical to what was described previously [32]. Butt coupling was used to couple light into the waveguide from a lensed fiber. The edge of the wafer was polished by diamond polishing to enhance the coupling efficiency. The polarization controllers (PC1 and PC2) were first calibrated using an on-chip polarizer. The structure and performance of the on-chip polarizer were described in [29]. We first adjust PC2 to enable alignment between the output polarization plane and the polarizer. The polarization component of the output light is selected by rotating the polarizer accordingly. In order to account for coupling and scattering losses, a waveguide without any metamaterial structures was used as reference, normalizing the measured transmission efficiency for the device with the MWB to that of the reference accounts for extraneous coupling and scattering losses. The reference transmission efficiency used in the normalization is the average of two reference waveguides. The normalized transmission-efficiency spectra for the two devices are shown in Figures 4.3(a) and 4.3(b). There is good agreement between simulation and experiments with small discrepancies primarily attributed to edge roughness of the waveguides, in-plane misalignment between input/output waveguides and the MWBs, and pixel-size and pixel-thickness errors. The measurements confirm transmission efficiency of 65% and 73% at $\lambda_0 = 1550$ nm for TE and TM, respectively.

The simulated efficiencies shown in Figures 4.3(a) and 4.3(b) predict a 1 dB bandwidth (i.e., where the transmission efficiency is higher than 80% of the peak value) of 82 nm and

66 nm for TE and TM polarizations, respectively. The experiments indicate that the measured 1 dB bandwidth for TE and TM polarizations are 67 nm and 56 nm, respectively. Although the TE device is designed for $\lambda = 1550$ nm, the peak transmission is observed at $\lambda = 1568$ nm. We believe that the fabrication errors, including pixel-size errors and device-thickness variations, are responsible for this shift. As has been pointed out previously, the ensemble nature of the coupled resonances assures a relatively large bandwidth for our devices.

We also investigated the sensitivity of our devices to fabrication errors using simulations. Both in-plane geometric error (misalignment between the input waveguide and the MWBs) and out-of-plane fabrication error (device-thickness variations) were considered. For the investigation of misalignment errors, we shifted the position of the input waveguide vertically (in-plane and orthogonal to the light propagation direction) and evaluated the transmitted power in the output waveguide. The resulting transmission efficiencies for the two devices are shown in Figure 4.3(c). Efficiencies remain nearly unchanged within ± 75 nm, a range that is half the width of the waveguide (300 nm). We next analyzed its sensitivity to device-(silicon) thickness variation (this is not generally important in a conventional CMOS process, but it is specific to our particular fabrication method as mentioned earlier). The simulated transmission efficiencies as a function of device thickness are shown in Figure 4.3(d) for the two devices. Note that the designed device thickness was 250 nm. The transmission efficiency is sufficiently preserved for a device-thickness variation of ± 25 nm, which is 10% of the design thickness. Note that there is a large drop off in efficiency for device thickness below 240 nm, because such a waveguide is unable to support any propagating modes. More specifically, for a 1 dB (20%)

drop in transmission efficiency from its peak, the device thickness can vary by as much as 60 nm for the TE device and 32 nm for the TM device. As we have seen previously, our design methodology results in extremely tolerant devices, and we attribute this to the incorporation of fabrication constraints during the design process.

4.5 Conclusion

In conclusion, we applied the principle of digital metamaterials to demonstrate two MWBs, one for each polarization. These MWBs enable the bending of light in single-mode, nanowire waveguides spaced by 1.3 μm over an angle of 180 deg, which corresponds to an effective bend radius of only 0.65 μm, smaller than half the design wavelength. Each MWB occupies an area of only 3 μm × 3 μm, corresponding to about $2\lambda_0 \times 2\lambda_0$. Most importantly, the bending of light is achieved with simulated peak-transmission efficiencies of over 80%. Our fabrication technologies limited the measured peak-transmission efficiencies to ~70%. Our devices are not only compatible with the conventional CMOS process, but they are also very tolerant to fabrication errors as illustrated by our numerical analysis. These designs can be extended to almost any waveguiding topology, which will enable the efficient in-plane routing of light for large-scale photonic integration.

4.6 References

[1] M. A. Sefunc, M. Pollnau, and S. M. García-Blanco, "Low-loss sharp bends in polymer waveguides enabled by the introduction of a thin metal layer," Opt. Express **21**, 29808-29817 (2013).

[2] W. Shin, W. S. Cai, P. B. Catrysse, G. Veronis, M. L. Brongersma, and S. H. Fan, “Broadband sharp 90-degree bends and T-splitters in plasmonic coaxial waveguides,” Nano Lett. **13**, 4753–4758 (2013).

[3] G. Veronis and S. H. Fan, “Bends and splitters in metal-dielectric-metal subwavelength plasmonic waveguides,” Appl. Phys. Lett. **87**, 131102 (2005).

[4] H. S. Chu, E. P. Li, P. Bai, and R. Hegde, “Optical performance of single-mode hybrid dielectric-loaded plasmonic waveguide-based components,” Appl. Phys. Lett. **96**, 221103 (2010).

[5] G. Veronis, Z. Yu, S. E. Kocabas, D. A. B. Miller, M. L. Brongersma, and S. Fan, “Metal-dielectric-metal plasmonic waveguide devices for manipulating light at the nanoscale,” Chin. Opt. Lett. **7**, 302–308 (2009).

[6] M. Z. Alam, J. Meier, J. S. Aitchison, and M. Mojahedi, “Propagation characteristics of hybrid modes supported by metal-low-high index waveguides and bends,” Opt. Express **18**, 12971–12979 (2010).

[7] D. J. Dikken, M. Spasenovic, E. Verhagen, D. van Oosten, and L. K. Kuipers, “Characterization of bending losses for curved plasmonic nanowire waveguides,” Opt. Express **18**, 16112–16119 (2010).

[8] D. F. P. Pile and D. K. Gramotnev, “Plasmonic subwavelength waveguides: next to zero losses at sharp bends,” Opt. Lett. **30**, 1186–1188 (2005).

[9] L. Jiang, H. Wu, W. Jia, and X. Li, “Optimization of low-loss and wide-band sharp photonic crystal waveguide bends using the genetic algorithm,” Optik **124**, 1721–1725 (2013).

[10] D. C. Tee, Y. G. Shee, N. Tamchek, and F. R. M. Adikan, “Structure tuned, high transmission 180° waveguide bend in 2D planar photonic crystal,” IEEE Photon. Technol. Lett. **25**, 1443–1446 (2013).

[11] P. I. Borel, A. Harpøth, L. H. Frandsen, M. Kristensen, P. Shi, J. S. Jensen, and O. Sigmund, "Topology optimization and fabrication of photonic crystal structures," Opt. Express **12**, 1996-2001 (2004).

[12] A. Chutinan and S. Noda, "Highly confined waveguides and waveguide bends in three-dimensional photonic crystal," Appl. Phys. Lett. **75**, 3739-3741 (1999).

[13] S. Kim, G. P. Nordin, J. Jiang, J. Cai, "High efficiency 90° silica waveguide bend using an air hole photonic crystal region," IEEE Phot. Technol. Lett. **16**, 1846-1848 (2004).

[14] J. S. Jensen, O. Sigmund, L. H. Frandsen, P. I. Borel, A. Harp∅th, and M. Kristensen, “Topology design and fabrication of an efficient double 90° photonic crystal waveguide bend,” IEEE Photonics Technol. Lett. **17**, 1202–1204 (2005).

[15] P. Strasser, G. Stark, F. Robin, D. Erni, K. Rauscher, R. Wüest, and H. Jäckel, “Optimization of a 60° waveguide bend in inp-based 2d planar photonic crystals,” J. Opt.

Soc. Am. B **25**, 67–73 (2008).

[16] L. Frandsen, A. Harp0th, P. Borel, M. Kristensen, J. Jensen, and O. Sigmund, "Broadband photonic crystal waveguide 60° bend obtained utilizing topology optimization," Opt. Express **12**, 5916-5921 (2004).

[17] E. Chow, S.Y. Lin, J.R. Wendt, S.G. Johnson, J.D. Joannopoulos, "Quantitative analysis of bending effiency in photonic crystal wavgeuide bends at $\lambda = 1.55\mu m$ wavelengths," Opt. Lett. **26**, 286-288 (2001).

[18] J. Smajic, C. Hafner, and D. Erni, “Design and optimization of an achromatic photonic crystal bend,” Opt. Express **11**, 1378-1384 (2003).

[19] B. Donderici and F. L. Teixeira, “Metamaterial blueprint for reflectionless waveguide bends,” IEEE Microw. Wirel. Compon. Lett. **18**, 233–235 (2008).

[20] B. Edwards, A. Alu, M. G. Silveirinha, and N. Engheta, “Reflectionless sharp bends and corners in waveguides using epsilon-near-zero effects,” J. Appl. Phys. **105**, 044905 (2009).

[21] M. Ishida, Y. Ikuma, T. Suzuki, and H. Tsuda, “180-degree-bend structures using light reflection at double elliptic mirror in slab waveguide,” Jpn. J. Appl. Phys. **46**, 168-174 (2007).

[22] Y. Qian, S. Kim, J. Song, and G. P. Nordin, “Compact and low loss silicon-on-insulator rib waveguide 90° bend,” Opt. Express **14**, 6020–6028 (2006).

[23] B. Shen, P. Wang, R. Polson, and R. Menon, “Ultra-high-efficiency metamaterial polarizer,” Optica **1**, 356–360 (2014).

[24] B. Shen, P. Wang, and R. Menon, “Optimization and analysis of 3D nanostructures for power-density enhancement in ultra-thin photovoltaics under oblique illumination,” Opt. Express **22**, A311–A319 (2014).

[25] B. Shen, P. Wang, R. Polson, and R. Menon, “An integrated-nanophotonics polarization beamsplitter with $2.4 \times 2.4\ \mu m^2$ footprint,” Nat. Photonics **9**, 378–382 (2015).

[26] B. Shen, P. Wang, R. Polson, and R. Menon, “Integrated metamaterials for efficient and compact free-space-to-waveguide coupling,” Opt. Express **22**, 27175–27182 (2014).

[27] B. Shen, R. Polson, and R. Menon, "Integrated digital metamaterials enables ultra-compact optical diodes," Opt. Express **23**, 10847-10855 (2015).

[28] B. Shen, R. C. Polson and R. Menon, “Broadband asymmetric light transmission via all-dielectric digital metamaterials,” Opt. Express **23**, 20961-20970 (2015).

[29] L. Liu, Y. Ding, K. Yvind, and J. M. Hvam, “Efficient and compact TE-TM polarization converter built on silicon-on-insulator platform with a simple fabrication process,” Opt. Lett. **36**, 1059–1061 (2011).

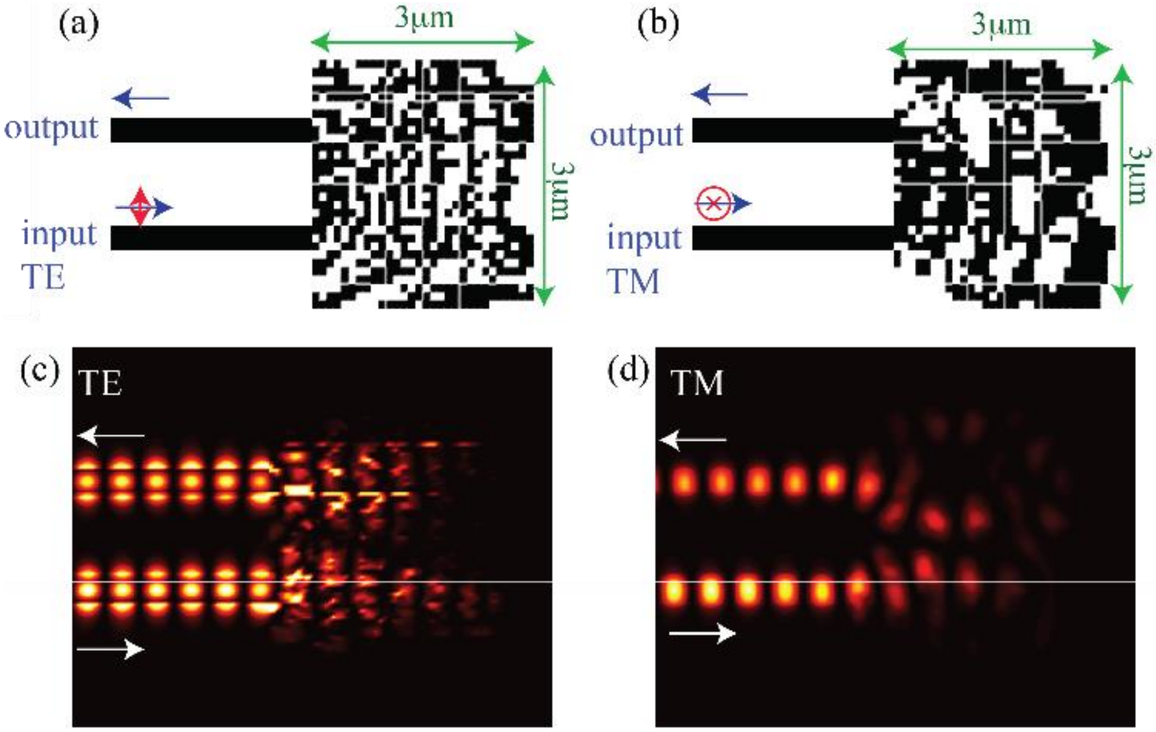

Figure 4.1. 180-degree metamaterial-waveguide bends for (a) TE and (b) TM polarizations. The spacing between the waveguides is 1.3 μm, and the equivalent bend radius is 0.65 μm. Blue arrows indicate the light propagation directions and red curves indicate the polarization states. Steady-state light intensity distribution for the (c) TE and (d) TM devices.

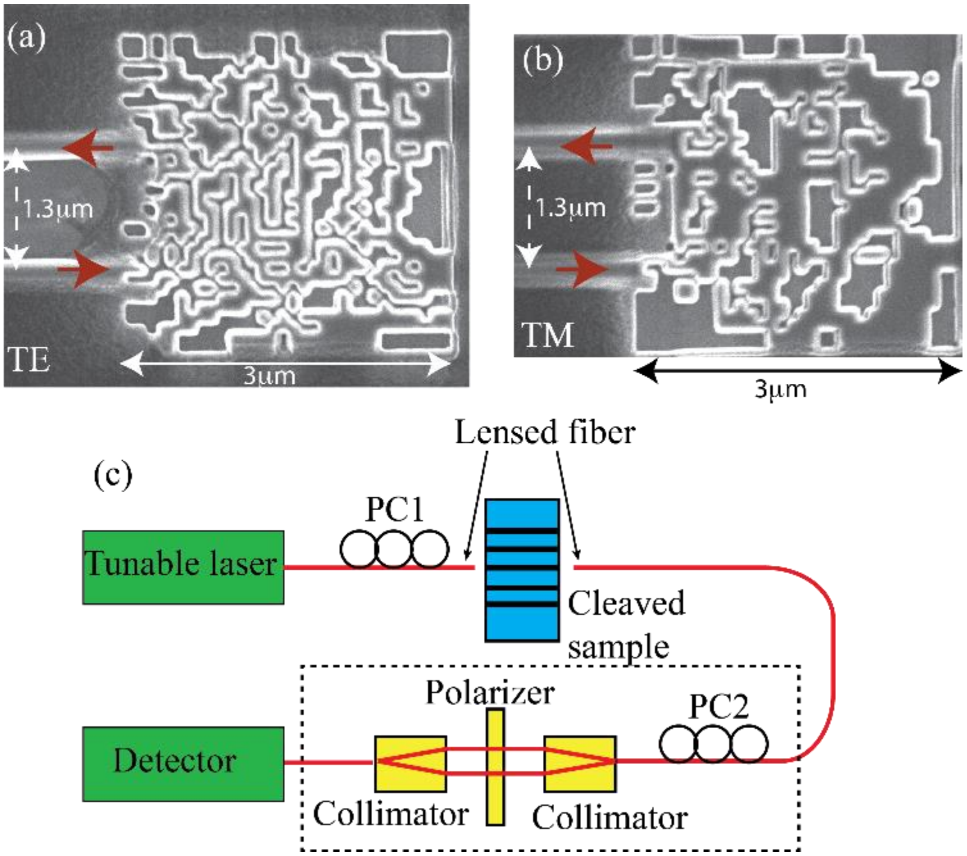

Figure 4.2. Experiment. Scanning electron micrographs of the fabricated devices for (a) TE and (b) TM polarizations. (c) Details of the measurement system set-up.

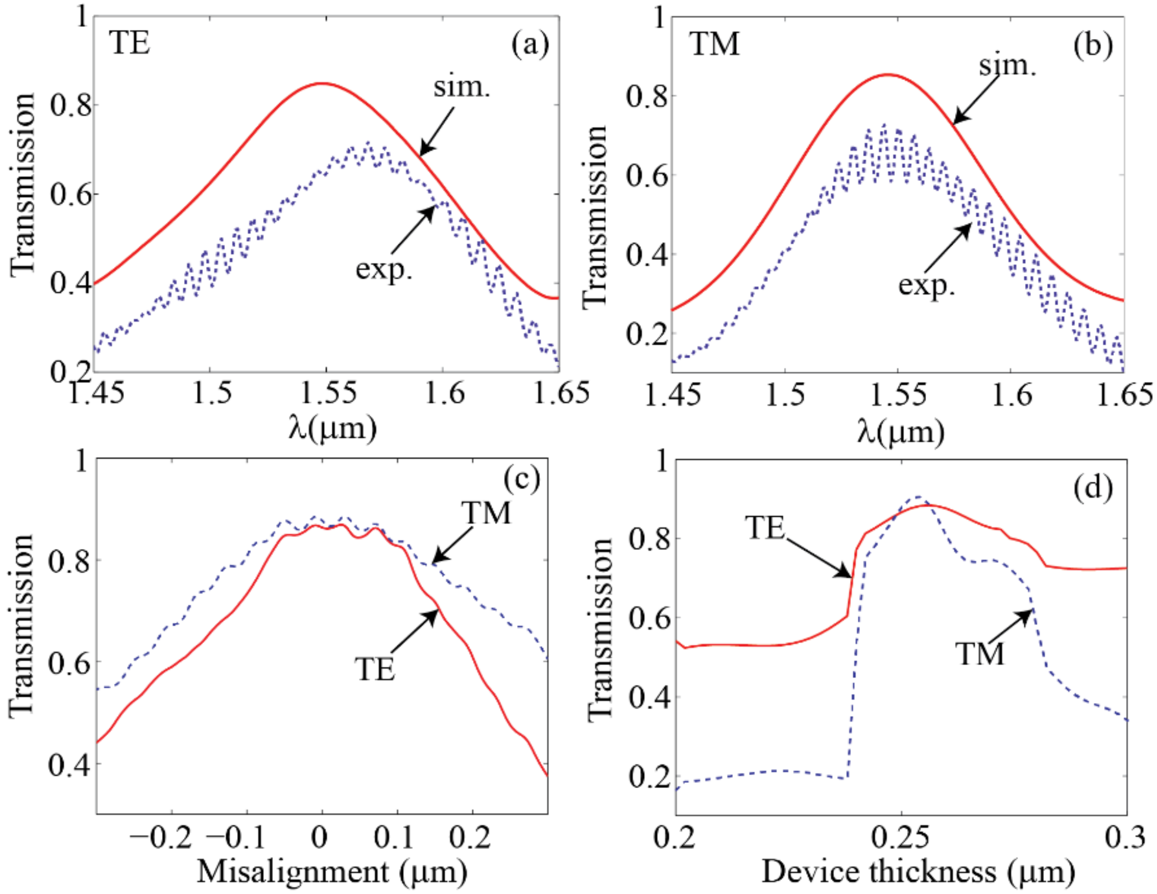

Figure 4.3. Experimental and simulated performance of the MWBs. Transmission efficiency spectrum for (a) TE and (b) TM devices. Measured (exp.) and simulated (sim.) data are shown using dashed and solid lines, respectively. (c) Simulated transmission efficiency as a function of misalignment between the input waveguide and the MWB for TE (solid-red curve) and TM (dashed-blue curve) polarizations. The misalignment is defined as shifting the position of input waveguide vertically that is orthogonal to the light propagation direction. (d) Simulated transmission efficiency as a function of silicon thickness for the TE (solid-red curve) and TM (dashed-blue curve) MWBs.

CHAPTER 5

INTEGRATED DIGITAL METAMATERIALS ENABLES ULTRACOMPACT OPTICAL DIODES

Reprinted and adapted with permission from [B. Shen, R. C. Polson, and R. Menon, “Integrated digital metamaterials enables ultra-compact optical diodes,” Opt. Express **23**, 8, 10847-10855 (2015).]. ©2015 Optical Society of America.

5.1 Abstract

We applied nonlinear optimization to design integrated digital metamaterials in silicon for unidirectional energy flow. Two devices, one for each polarization state, were designed, fabricated, and characterized. Both devices offer comparable or higher transmission efficiencies and extinction ratios, are easier to fabricate, exhibit larger bandwidths and are more tolerant to fabrication errors, when compared to alternatives. Furthermore, each device footprint is only 3 μm × 3 μm, which is the smallest optical diode ever reported. To illustrate the versatility of digital metamaterials, we also designed a polarization-independent optical diode.

5.2 Introduction

Devices that enable asymmetric light transmission, that is, light transmits in one direction, but doesn't transmit in the opposite direction, are extremely useful for a variety of photonic applications. However, their implementation in integrated devices is challenging [1]. This functionality can be achieved by breaking the Lorentz symmetry condition, typically via various nonlinearities. Examples of such nonreciprocal devices include those that use magneto-optic materials [2–6], metamaterials [7] or indirect interband photonic transitions [8]. Devices that utilize combinations of metal and dielectric or magneto-optical materials are not compatible with CMOS fabrication technologies. Furthermore, such nonreciprocal devices tend to be large and require significant power input. Although nonreciprocal devices are necessary for certain applications such as optical isolation, asymmetric light transmission (or optical diode behavior) can be achieved with much simpler passive devices via spatial symmetry breaking as long as the functionality is limited to a finite number of input modes [9]. Such devices are simpler to fabricate and are significantly smaller than their non-reciprocal counterparts. Examples of such devices include those based on metamaterials [10], photonic crystals [11–14], metallic-silicon waveguide [15], and ring resonators [16]. Recently, an ultra-compact optical diode (size ~3 μm × 5 μm) that utilizes a combination of photonic crystal and gratings was proposed [13]. However, this device operates only for TM polarization and for frequencies outside the telecommunications band. Achieving polarization insensitive optical diodes is challenging and most of the devices presented previously are polarization dependent. This is due to the fact that photonic crystals can typically manipulate only one polarization state. By combining waveguides with metasurfaces, a polarization independent optical diode was recently demonstrated in the microwave regime [10]. This device is not readily extended to the telecommunications band due to the complexity of fabrication.

5.3 Methods

Here, we overcome previous limitations by applying the concept of digital metamaterials [17,18], that is, devices where the local permittivity is engineered in a fabrication-constrained fashion in order to achieve desired mode-conversion functionality. Specifically, we designed, fabricated and characterized integrated, all dielectric (silicon on silicon-dioxide) optical diodes each with dimension of 3 μm × 3 μm, which is the smallest such device ever reported. We experimentally verified the performance of two such devices, one for each polarization state. We also designed a third device, which exhibits polarization independent diode behavior at the expense of slightly higher insertion loss. Digital metamaterials is a subset of free-form metamaterials, where mode conversion is achieved by optimized 3D or 2D nanophotonic geometries [19,20]. By imposing fabrication constraints, we ensure that the devices are not only CMOS compatible and easy to fabricate, but are also robust to fabrication errors.

Each device is comprised of 30 × 30 square "pixels" of size 100nm × 100nm, resulting in a total area of 3 μm × 3 μm. Light enters and exits the device via 3μm-wide multimode waveguides as illustrated in Figure 5.1. Polarized light launched from left to right propagates through the device, while that launched in the opposite direction is reflected. All devices are designed for λ_0 = 1550nm and are fabricated on a silicon-on-insulator (SOI) substrate with top silicon thickness of 300nm and an oxide thickness of 3 μm. The device for TE polarization is illustrated in Figure 5.1(a) and that for TM polarization is illustrated in Figure 5.1(d). The white regions represent air, where the silicon has been etched away (black regions represent unetched silicon) and the etch depth is the same as the depth of the waveguide, 300nm. This further implies that the device can be fabricated at the same time as the waveguides, and a separate lithography step is not required. For TE, the simulated forward (from left to right) transmission efficiency is 71.1% and the backward efficiency is 1.8%. While for TM, the simulated forward and backward transmission efficiencies are 91.1% and 3.2%, respectively. These efficiencies are comparable to those reported for previous devices, but our devices are significantly smaller. The simulated steady-state intensity distributions for both devices are shown in Figures 5.1(b)-5.1(c) and Figures 5.1(e)-5.1(f) for TE and TM polarizations, respectively. The field distributions indicate that mode conversion is primarily enabled by coupled guided-mode resonances in the nanostructures. The refractive index variation introduced by the metamaterial device creates a perturbation of the input mode. As a result, multiple guided-mode resonances are excited so as to create a transmission band for the forward propagation direction but a forbidden band in the backward direction.

Digital metamaterials may be designed using a variety of optimization algorithms. Here, we applied a relatively simple variation of the direct-binary-search (DBS) algorithm. DBS was previously used to design broadband nonimaging optics [21,22], free-space polarizers [18], integrated devices [17], and nanophotonic light-trapping structures [23,24]. Here, we further adapt the algorithm to design the digital metamaterials illustrated in Figures 5.1(a) and 5.1(d). The 3 μm × 3 μm device is first discretized into 30 × 30 pixels and each pixel could exist in two possible states: silicon or air. Different pixel-state distributions will exhibit different permittivity distributions and thereby, distinct electromagnetic properties. DBS is then implemented to optimize the pixel-state distribution that gives us the desired electromagnetic properties. Here, DBS tried to increase the forward transmission efficiency, while minimizing the backward one. The search algorithm was described previously in ref [17]. All the 900 binary pixels are traversed in random order within each iteration. Proper termination conditions such as a minimum improvement in FOM and maximum iteration numbers are imposed to guarantee numerical convergence. Because of the algorithm’s tendency of premature convergence to local maxima, we repeated the same optimization process with several randomly generated initial candidates, among which the best optimized solution was chosen. In addition, we parallelized the algorithm and used Amazon’s EC2 service to expedite the optimization. Using one micro cluster composed of three virtual machines, each with 32 virtual CPUs, the optimization time was ~270 hours. An open-source finite-difference time domain (FDTD) solver (MEEP) was used to simulate the full 3D distribution of electromagnetic fields within our designs [25].

5.4 Experiments and results

Although the devices illustrated in Figure 5.1 could be fabricated via a single-lithography step, we adopted a two-step process, since we do not have access to high-resolution optical-projection lithography. Heidelberg MicroPG 101 (laser pattern generator) was first used to pattern 3μm-wide waveguide, and the Oxford 100 reactive-ion etcher (RIE) with a gas mixture of SF_6 and C_4F_8 was used to etch the silicon. The second step, which defines the metamaterial diode used the dual-beam focused-ion-beam (FIB, FEI, Helios 650) system. Fiducial marks were used to enable alignment between the two steps. Other details of the fabrication process was described in [17]. The scanning-electron micrographs of the final devices are shown in Figures 5.2(a) and 5.2(b).

The measurement system is sketched in Figure 5.2(c) [26] and measurement steps were similar to the ones described in [17]. The polarization controllers (PC1 and PC2) were first calibrated using the on-chip polarizer. The on-chip polarizer consists of a straight waveguide with a vertical air slot near the center of the waveguide. The center of the air slot has a 70nm offset with respect to the center of the waveguide. For the on-chip polarizer, TM is transmitted efficiently, while TE is blocked. The on-chip polarizer allows us to control the input mode (TE or TM). The alignment between the output polarization plane and the polarizer was achieved by adjusting PC2. The polarization components of the output light could be selected by rotating the polarizer accordingly.

In order to rule out the impact from butt coupling loss between the lensed fiber and the waveguide as well as the propagation loss of silicon waveguide, a straight 3μm-wide waveguide without any patterns was used as a reference. Normalizing the measured transmission efficiency for the waveguide containing the optical diode against that for the unpatterned waveguide provides the measured transmission efficiency for our metamaterial device. The measured forward and backward transmission efficiencies for both devices are shown in Figures 5.2(d) and 5.2(e). The measured spectra are close to the simulated ones. Small differences between them are probably due to the edge roughness of the waveguide and small errors in alignment among the 2 lithography steps. We measured forward and backward transmission efficiencies of 62.1% and 2.8% for TE, and 79.8% and 10.4% for TM.

5.5 Discussion

For true optical isolation, the backward transmission efficiency for modes of any order should be zero [9]. This can be achieved only by devices that break Lorentz symmetry (reciprocity). Magneto-optical or optical nonlinear materials are the most common choices for such nonreciprocal devices. However, as stated earlier, such materials are not compatible with CMOS technology, and these devices tend to be much larger and require power. On the other hand, passive optical diodes are reciprocal devices and as such cannot be optical isolators in the general sense. Their diode function is only valid typically for a single input mode [10–13]. Our devices are also reciprocal and passive, but because of the generality of their design can exhibit diode functionalities for more than 1 input mode. We numerically investigated the performance our TE diode under illumination by higher order modes and the results are summarized in Figure 5.3. In Figure 5.3(a), we plot the extinction ratio, defined as the ratio between forward and backward transmission efficiencies, as a function of the incident mode order. Since our device is designed for the fundamental mode, the highest extinction ratio is observed when the mode order is 1 and it deteriorates at higher orders. However, the deterioration for the second order mode is small and optical diode behavior is sufficiently preserved as illustrated by the steady-state light-intensity distributions in Figures 5.3(c) and 5.3(d). When the same simulation is performed for the 3rd order mode (Figure 5.3(e)), the diode behavior is not seen (see Figures 5.3(f) and 5.3(g)). Thus, our device is an effective diode for the first two TE modes.

We numerically investigated the robustness of our designs to fabrication errors. Specifically, we varied the device (silicon) thickness that is determined by the etching depth of the pixels. The resulting forward and backward transmission efficiencies for the two devices are shown in Figures 5.3(h) and 5.3(i), respectively. As expected, the efficiency drops as the thickness changes from the design value of 300 nm. If we are able to tolerate an efficiency drop of 20% from the peak value, we can specify the allowable thickness variation as ± 26 nm.

We also simulated the time evolution of the electric field within the two devices in order to visualize their performance. Due to the subwavelength structures within each device, evanescent modes are excited. For the forward transmission, these evanescent modes constructively interfere and give rise to multiple resonant modes that are propagating in the plane of the device. When the TE diode is illuminated in the backward direction, the excited evanescent modes interfere destructively, leading to negligible light in the output waveguide. When the TM diode is illuminated in the backward direction, the evanescent modes interfere so as to excite resonant modes that are coupled out of instead of into the output waveguide. The asymmetry in the spatial distribution of refractive indices gives rise to the drastic difference in transmission in the two directions. In addition, we performed a 2D discrete Fourier transformation (DFT) of our nanophotonic structures (diode Ez) to gain further insight into the physics. For comparison, a similar nanophotonic structure but with random pattern is also analyzed. The results are summarized in Figure 5.4. The left column shows the permittivity distribution of the device and the right column shows the 2D DFT results. It is found that the random (Figure 5.4(a)) pattern yields wavevectors that are too diffuse, which means that input energy is transferred to almost any supported mode, most of which cannot radiate efficiently into the output waveguide. However, for our optimized device, the wavevectors are substantially limited to the central area denoted by the red circle in Figure 5.4(b), which correspond to modes that can radiate efficiently into the output waveguide. This means input energy could be efficiently transferred to the propagation modes in the output waveguide.

5.6 Polarization-independent optical diode

We can apply the concept of digital metamaterials to design a polarization-independent optical diode. The resulting device geometry is illustrated in Figure 5.5(a) and the simulated steady-state light-intensity distributions for both polarization states at the design wavelength (1.55 μm) are shown in Figures 5.5(c)-5.5(f). The simulated forward and backward transmission efficiencies for the 2 polarization states are summarized in Figure 5.5(b). Although the insertion loss is higher, the device operates as a reasonable diode for both polarizations. In particular, we simulated an extinction ratio of 8.9 dB and 10.5 dB for TM and TE, respectively. Our device is particularly interesting because it is thousands of times smaller than an alternative polarization independent device proposed recently [10].

5.7 Conclusion

We designed, fabricated, and characterized ultracompact integrated reciprocal optical diodes, devices that efficiently transmit light in one direction, while blocking it in the opposite direction. These devices are an example of digital metamaterials that enable fabrication-friendly, yet highly functional devices that are significantly smaller than alternatives. To the best of our knowledge, our optical diodes are the smallest such devices ever reported. We measured forward and backward transmission efficiencies of 62.1% and 2.8% for the TE diode and 79.8% and 10.4% for the TM diode, respectively. Furthermore, numerical studies indicate that the TE diode maintains its performance for the first 2 incident orders. Finally, we also designed a polarization-independent optical diode that is only 3 μm × 3 μm in size. It is important to point out that digital metamaterials can enable almost any linear mode-convertor, and can be optimized for functionality, size and ease of fabrication.

5.8 References

[1] M. Soljačić and J. D. Joannopoulos, “Enhancement of nonlinear effects using photonic crystals,” Nat. Mater. **3**(4), 211–219 (2004).

[2] R. L. Espinola, T. Izuhara, M. C. Tsai, R. M. Osgood, Jr., and H. Dötsch, “Magneto-optical nonreciprocal phase shift in garnet/silicon-on-insulator waveguides,” Opt. Lett. **29**(9), 941–943 (2004).

[3] M. A. Levy, “Nanomagnetic route to bias-magnet-free, on-chip Faraday rotators,” J. Opt. Soc. Am. B **22**(1), 254–260 (2005).

[4] T. R. Zaman, X. Guo, and R. J. Ram, “Faraday rotation in an InP waveguide,” Appl. Phys. Lett. **90**(2), 023514 (2007).

[5] H. Dötsch, N. Bahlmann, O. Zhuromskyy, M. Hammer, L. Wilkens, R. Gerhardt, P. Hertel, and A. F. Popkov, “Applications of magneto-optical waveguides in integrated optics: review,” J. Opt. Soc. Am. B **22**(1), 240–253 (2005).

[6] L. Bi, J. Hu, P. Jiang, D. H. Kim, G. F. Dionne, L. C. Kimerling, and C. A. Ross, “On-chip optical isolation in monolithically integrated non-reciprocal optical resonators,” Nat. Photonics **5**(12), 758–762 (2011).

[7] M. Mutlu, A. E. Akosman, A. E. Serebryannikov, and E. Ozbay, “Diodelike asymmetric transmission of linearly polarized waves using magnetoelectric coupling and

electromagnetic wave tunneling," Phys. Rev. Lett. **108**(21), 213905 (2012).

[8] Z. Yu and S. Fan, "Complete optical isolation created by indirect interband photonic transitions," Nat. Photonics **3**(2), 91-94 (2009).

[9] D. Jalas, A. Petrov, M. Eich, W. Freude, S. Fan, Z. Yu, R. Baets, M. Popović, A. Melloni, J. D. Joannopoulos, M. Vanwolleghem, C. R. Doerr, and H. Renner, "What is and what is not an optical isolator," Nature Photon. **7**, 579–582 (2013).

[10] Y. D. Xu, C. D. Gu, B. Hou, Y. Lai, J. S. Li, and H. Y. Chen, "Broadband asymmetric waveguiding of light without polarization limitations," Nat. Commun. **4**, 2561 (2013).

[11] C. Wang, C. Z. Zhou, and Z. Y. Li, "On-chip optical diode based on silicon photonic crystal heterojunctions," Opt. Express **19**(27), 26948-26955 (2011).

[12] V. Liu, D. A. B. Miller, and S. Fan, "Ultra-compact photonic crystal waveguide spatial mode converter and its connection to the optical diode effect," Opt. Express **20**(27), 28388-28397 (2012).

[13] Y. Zhang, Q. Kan, and G. P. Wang, "One-way optical transmission in silicon grating-photonic crystal structures," Opt. Lett. **39**(16), 4934-4937 (2014).

[14] C. Wang, X. Zhong, and Z. Li, "Linear and passive silicon optical isolator," Sci. Rep. **2**, 1–6 (2012).

[15] L. Feng, M. Ayache, J. Huang, Y.-L. Xu, M.-H. Lu, Y.-F. Chen, Y. Fainman, and A. Scherer, "Nonreciprocal light propagation in a silicon photonic circuit," Science **333**(6043), 729–733 (2011).

[16] L. Fan, J. Wang, L. T. Varghese, H. Shen, B. Niu, Y. Xuan, A. M. Weiner, and M. H. Qi, "An all-silicon passive optical diode," Science **335**(6067), 447–450 (2012).

[17] B. Shen, P. Wang, R. Polson, and R. Menon, "Integrated metamaterials for efficient and compact free-space-to-waveguide coupling," Opt. Express **22**(22), 27175-27182 (2014).

[18] B. Shen, P. Wang, R. Polson, and R. Menon, "Ultra-high-efficiency metamaterial polarizer," Optica **1**(5), 356-360 (2014).

[19] J. Lu and J. Vučković, "Nanophotonic computational design," Opt. Express **21**(11), 13351–13367 (2013).

[20] A. Y. Piggott, J. Lu, T. M. Babinec, K. G. Lagoudakis, J. Petykiewicz, and J. Vučković, "Inverse design and implementation of a wavelength demultiplexing grating coupler," Sci. Rep. **4**, 7210 (2014).

[21] G. Kim, J.-A. Dominguez-Caballero, H. Lee, D. J. Friedman, and R. Menon, “Increased photovoltaic power output via diffractive spectrum separation,” Phys. Rev. Lett. **110**(12), 123901 (2013).

[22] G. Kim and R. Menon, “An ultra-small three dimensional computational microscope,” Appl. Phys. Lett. **105**(6), 061114 (2014).

[23] P. Wang and R. Menon, “Optimization of generalized dielectric nanostructures for enhanced light trapping in thin-film photovoltaics via boosting the local density of optical states,” Opt. Express **22**(S1), A99–A110 (2014).

[24] B. Shen, P. Wang, and R. Menon, “Optimization and analysis of 3D nanostructures for power-density enhancement in ultra-thin photovoltaics under oblique illumination,” Opt. Express **22**(S2), A311–A319 (2014).

[25] A. F. Oskooi, D. Roundy, M. Ibanescu, P. Bremel, J. D. Joannopoulos, and S. G. Johnson, “MEEP: A flexible free-software package for electromagnetic simulations by the FDTD method,” Comput. Phys. Commun. **181**(3), 687–702 (2010).

[26] L. Liu, Y. Ding, K. Yvind, and J. M. Hvam, "Efficient and compact TE–TM polarization converter built on silicon-on-insulator platform with a simple fabrication process," Opt. Lett. **36**(7), 1059-1061 (2011).

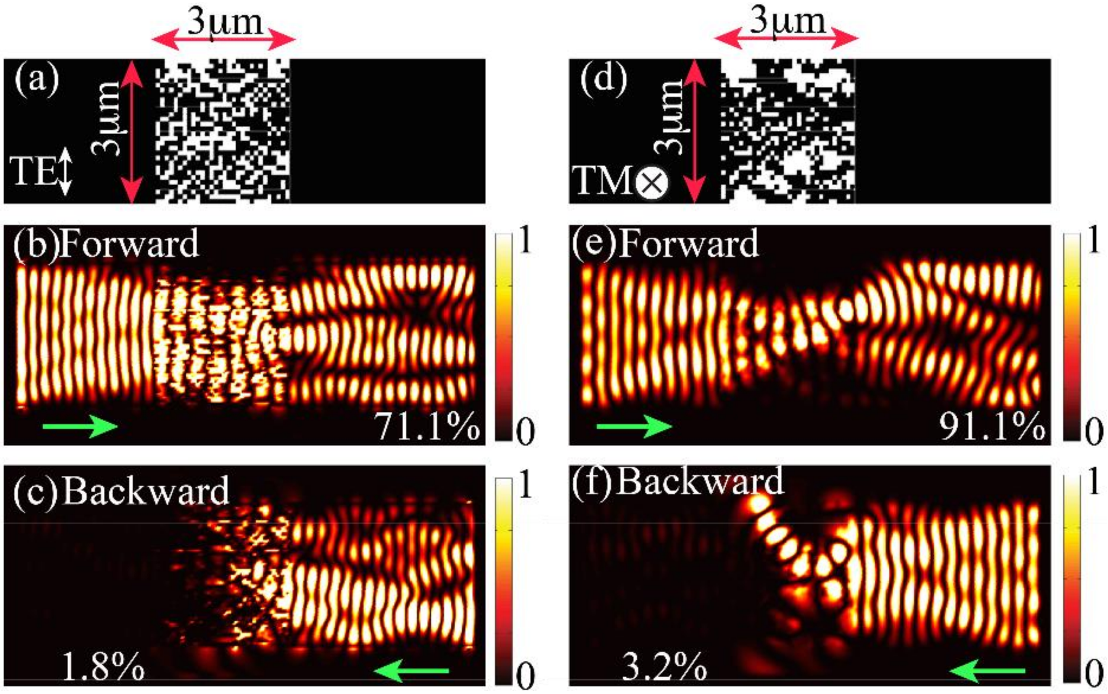

Figure 5.1. Ultracompact integrated optical diodes. (a) Geometry of the device for TE. Steady-state light intensity distribution in the (b) forward and (c) backward directions for TE. (d) Geometry of the device for TM. Steady-state light intensity distributions in the (e) forward and (f) backward directions for TM. Green arrows indicate the incident light propagation directions.

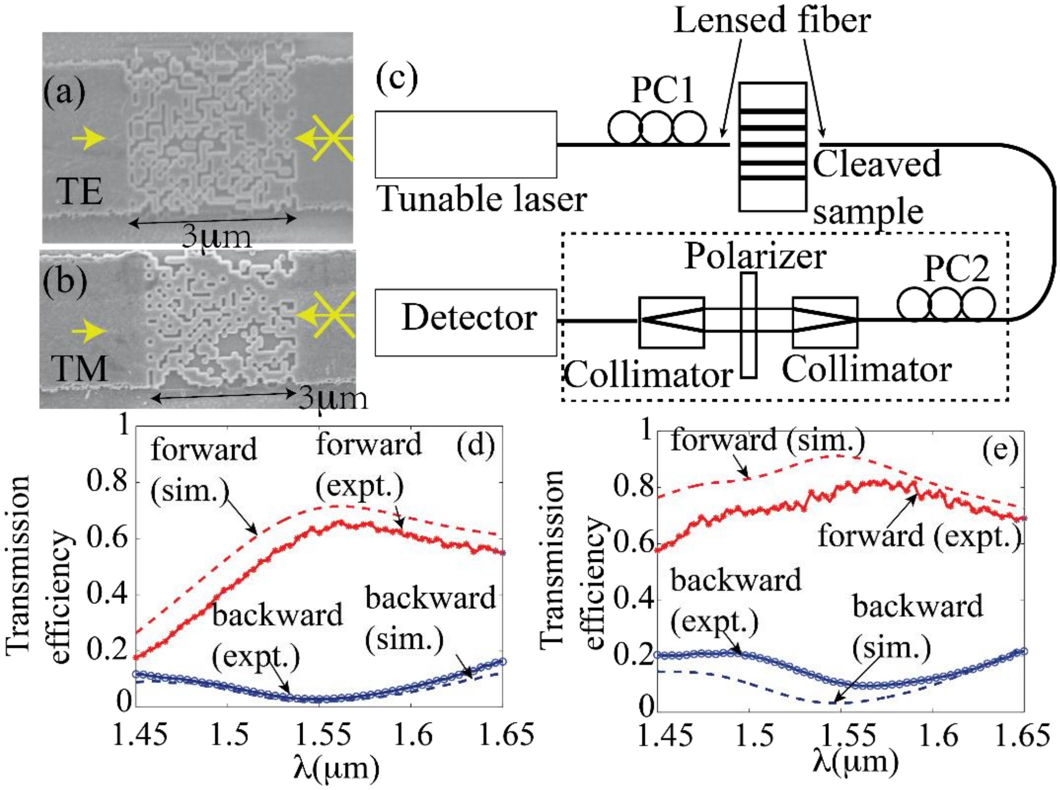

Figure 5.2. Scanning-electron micrograph of fabricated devices designed for (a) TE and (b) TM polarizations. (c) Schematic of the measurement system. Measured and simulated forward and backward transmission efficiencies as a function of wavelength for the optical diode designed for (d) TE and (e) TM polarizations. In (d) and (e), forward and backward efficiencies are denoted by red and blue lines, respectively. The experimental and simulation data are represented using solid and dashed lines, respectively.

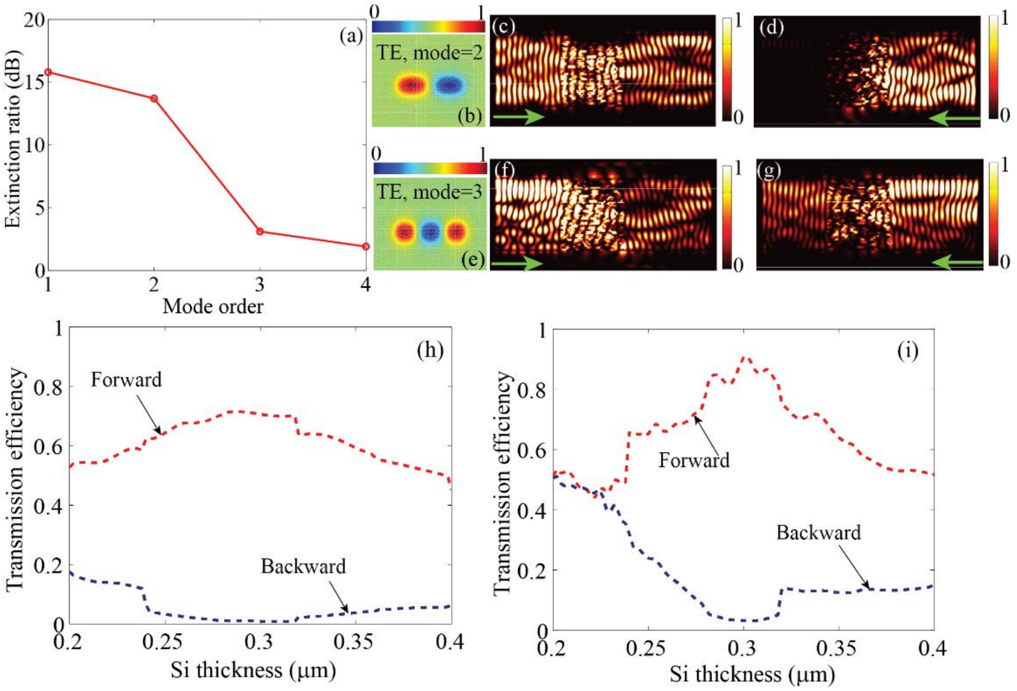

Figure 5.3. (a) Simulated extinction ratio as a function of mode order. (b) The profile of input mode of second order and its corresponding intensity pattern in the (c) forward and (d) backward directions. (e) The profile of input mode of third order and its corresponding intensity pattern in the (f) forward and (g) backward directions. Green arrows indicate the incident light propagation direction. Simulated transmission efficiency as a function of the silicon thickness for the diodes designed for (h) TE and (i) TM polarizations.

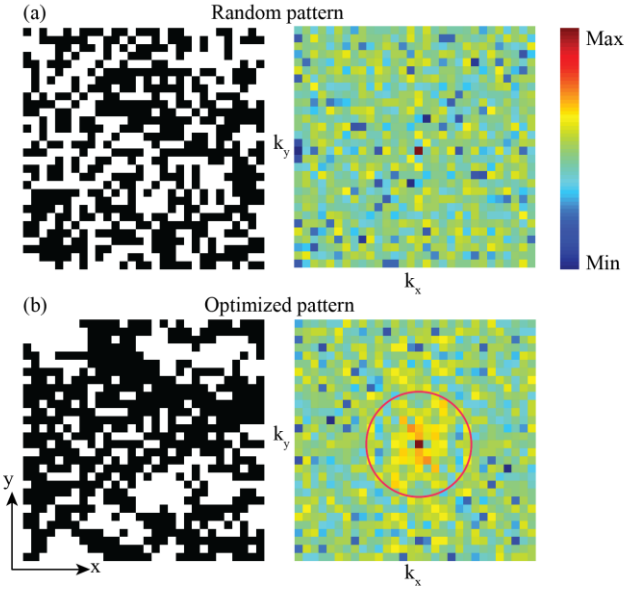

Figure 5.4. Fourier transforms of a metamaterials with pixels arranged in (a) random pattern and (b) pattern optimized for optical diode in Ez. (a) The wave-vectors of the random pattern are very diffuse compared to (b) those of the optimized pattern. The size of each device is 3 μm × 3 μm.

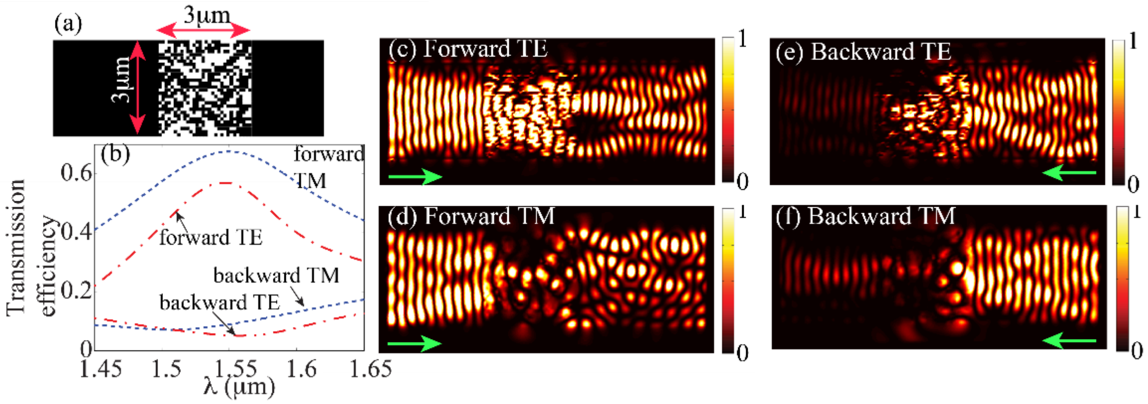

Figure 5.5. Polarization-independent optical diode. (a) Geometry of the optimized device. (b) Simulated transmission efficiencies for both polarization states in the forward and backward directions. (c) - (f) Steady-state light-intensity distributions for both polarization states in forward and backward directions. Green arrows indicate the incident light propagation directions.

CHAPTER 6

INCREASING THE DENSITY OF PASSIVE PHOTONIC-INTEGRATED CIRCUITS VIA NANOPHOTONIC CLOAKING

Reprinted and adapted with permission from [B. Shen, R. C. Polson, and R. Menon, “Increasing the density of passive photonic-integrated circuits via nanophotonic cloaking,” Nature Communications **7**, 13126 (2016).]. ©2016 Nature Publishing Group.

6.1 Abstract

Photonic-integrated devices need to be spaced apart to prevent signal crosstalk. This fundamentally limits their packing density. Here, we report the use of nanophotonic cloaking to render neighboring devices invisible to one another, which allows them to be placed closer together than is otherwise feasible. Specifically, we experimentally demonstrated waveguides that are spaced by a distance of ~$\lambda_0/2$ and designed waveguides with center-to-center spacing as small as 600nm (<$\lambda_0/2.5$). Our experiments show transmission efficiency >-2 dB and extinction ratio >15dB over bandwidth >60 nm. This performance can be improved with better design algorithms and improved fabrication. The nanophotonic cloak relies on multiple guided-mode resonances, which render such devices very robust to fabrication errors. Our devices are broadly CMOS compatible, have a minimum pitch of 200 nm and can be fabricated with a single lithography step. The nanophotonic cloaks are generally applicable and can be readily applied to all passive integrated photonics.

6.2 Introduction

Planar lightwave circuits (PLC) have significant advantages over electronic circuits such as large bandwidth [1,2], absence of Joule effect [1,2], higher immunity to interference, among many others. However, the main disadvantage of PLC is their considerably lower density compared to integrated electronics. There are several options to increase the integration density of PLC. One can shrink the footprint of the component devices. Various methods have been proposed to decrease device dimensions including the application of plasmonics [3-5] or of nanophotonics [6-9]. We have previously demonstrated an integrated nanophotonic polarization beamsplitter (PBS) with a footprint

2.4 × 2.4 μm^2, which is at least an order of magnitude smaller than comparable integrated devices that have been demonstrated experimentally before [7]. A second option to increase integration density is to combine the function of multiple devices into a single compact device. Examples of such multi-functional devices include polarization-splitting grating couplers [10], mode-converting polarization splitters [7], and a transformation-optics-based beam shifter [11]. A third option for enhancing integration density is to decrease the spacing between the individual devices. Waveguiding of light in the plane of the PLC is one of the most fundamental functions. However, the integration density of waveguiding is limited by the leakage of light from one waveguide to its neighbor (crosstalk), if the spacing between them is too small. Song, et al. proposed a method to decrease this spacing without considerably increasing crosstalk [12]. However, a general method to decrease the spacing between various devices has not been demonstrated.

Here, we apply cloaking to shield the closely-spaced devices so as to enable them to be integrated at a much higher density that is otherwise feasible. Furthermore, our approach is generally applicable to various integrated photonic components. Cloaking to prevent detection has been proposed using numerous technologies [13-15]. Zografopoulo, et al. proposed a method for integrated cloaking based on plasmonics, which however, exhibits considerable parasitic absorption losses due to metal [16]. Integrated all-dielectric cloaks employing conformal mapping were experimentally demonstrated before [17,18]. However, the cloaks typically exhibit footprints of hundreds of microns.

6.3 Results

The concept of “digital metamaterials” that we previously demonstrated was applied to design integrated cloaking devices. The design algorithm is detailed in our previous publications [19-22]. In general, we discretize the device area, say 7 μm × 0.5 μm, into hundreds of pixels, each pixel of size 100 nm × 100 nm. There are two possible states for each pixel: silicon denoted as “1” or air where silicon is etched away and denoted as “0.” As a result, our device can be exclusively represented by a binary sequence. By toggling the subwavelength pixels between the two states using an iterative optimization technique, we are able to design photonic devices with useful functions. The 100 nm feature size can be readily achieved with advanced photolithography used in the semiconductor industry and our devices are CMOS compatible. Here, we apply this design technique to two different device scenarios. First, we design a nanophotonic cladding-cloak that prevents the crosstalk between two closely-spaced single-mode waveguides. We experimentally demonstrate that waveguides with a center-to-center spacing as small as 0.8 μm (λ_0/1.94) are feasible. This would effectively double the integration density of PLC, since the conventional minimum center-to-center spacing between parallel waveguides is ~1.5 μm [23]. In the second scenario, we designed a nanophotonic cloak that prevents crosstalk between a single-mode waveguide and a closely-spaced micro-ring resonator. This device configuration is commonly used for filters and such cloaks can be quite useful for integrating multiple filters into a small area.

6.4 Experiments

The nanophotonic cloaks for closely spaced waveguides along with the reference waveguides are illustrated in Figure 6.1. The cross-section of each waveguide is 0.3 μm × 0.3 μm, the center-to-center spacing between the two parallel waveguides is 0.8 μm and the design wavelength, λ_0 = 1550 nm. The signal is launched in the bottom waveguide from the left propagating to the right. In order to prevent the signal from leaking to the neighboring (top) waveguide, we designed a nanophotonic cloak in the cladding region (between the two waveguides). The cloak is confined in an area of 0.5 μm × 7 μm. The minimum feature size of the cloak is 100 nm × 100 nm. The devices for the TE and TM polarizations are illustrated in Figures 6.1(a) and 6.1(c), respectively. The corresponding steady-state intensity distributions in the waveguides are illustrated in Figures 6.1(b) and 6.1(d), respectively. In both cases, it is clear that there is no light leakage from the bottom waveguide to the top, even though the center-to-center spacing between them is almost $\lambda_0/2$. In other words, the nanophotonic cloak essentially renders the bottom waveguide invisible to the top waveguide.

As reference, we also simulated the devices when no nanophotonic cloak is present as illustrated in Figures 6.1(e) and 6.1(g) for the TE and TM polarizations, respectively. The corresponding steady-state intensity distributions are illustrated in Figures 6.1(f) and 6.1(h), respectively. As expected, a large fraction of the light launched in the bottom waveguide (from left to right) is coupled into the top waveguide.

Devices were fabricated using a combination of optical lithography and focused-ion-beam lithography as described previously [7]. Optical patterning via the Heidelberg μPG 101, is used to generate the pattern for the large structures including the input/output multimode waveguides interfacing the lensed fiber, multimode to single-mode tapers, etc. Dual-beam focused-ion beam lithography tool, FEI Helios 650, is used for fabricating the fine features. Scanning-electron micrographs of the fabricated devices are shown in Figures 6.2(a) and 6.2(b) for TE and TM polarizations, respectively.

The measurement setup used to characterize the devices is similar to that described in our previous paper [7]. In general, light from an IR laser goes through a polarization controller (PC) before being coupled to the waveguide via a lensed fiber. The PC in the input path is used to rotate the input polarization state and we use an on-chip polarizer to confirm the polarization state of the light coupled to the waveguide [7]. After transmitting the device, the light is collected by another lensed fiber and goes through another PC and polarizer before being absorbed by the photodetector. The PC in the output path is used to align the polarization plane of the output light with the polarizer and the polarizer is used to select the polarization component of the output light to be measured. Normalizing the transmission of the cloaked waveguides to those of the reference waveguides provides the transmission efficiency. In each figure, we have plotted the transmission efficiency, which is defined as the efficiency with which a signal launched at port 1 (left, bottom waveguide) reaches its intended destination, port 2 (right, bottom waveguide) as a function of wavelength. Dashed-red lines denote the measured spectra, while solid-blue lines show the corresponding simulations. We have also plotted the crosstalk spectrum, defined as the fraction of light launched at port 1 that ends up at the unintended destinations, port 3 (right, top waveguide) and port 4 (left, top waveguide). The green error bars in each figure illustrate the fluctuation of measurement data primarily due to low signal-to-noise ratio (SNR). Sidewall roughness in the waveguides also introduces a certain level of uncertainty in our measurements, which will be mitigated when these devices are fabricated using commercial lithographic processes.

The measured TE transmission efficiency at the design wavelength (1550nm) is -1.519 dB, while the corresponding simulated value is -0.362 dB. The simulated cross-talk at design wavelength (1550 nm) is -28.5 dB averaged over both directions (1→4 and 1→3), while measurement confirms an average cross-talk of -21.1 dB. The measured average TM transmission efficiency at the design wavelength (1550 nm) is -0.336 dB, compared to the simulated value of -0.0071 dB. The measured average TM crosstalk at λ = 1550 nm is -22.9 dB, while the simulated value is -35.87 dB.

The nanophotonic cloak was designed to render the bottom waveguide invisible to the top waveguide. However, we noticed that for the TM device the same cloak is able to render the top waveguide invisible to the bottom waveguide. In other words, if the signal is launched from port 4 (left, top waveguide), we confirmed using measurements that the vast majority of the signal ends up at its intended destination, port 3. Details of these measurements and simulations are included in the supplementary information. For TE-cloak, the simulated transmission efficiency is greater than -1.169 dB within the bandwidth of 60 nm. The transmission efficiency for TM-cloak remains unchanged within the band of interest, which is approaching 100%. Such a large operating bandwidth is possible because a number of guided-mode resonances (rather than a single resonance) are responsible for the cloaking effect.

Numerically evaluated transmission efficiencies for TE- and TM-cloak under various device thicknesses (Figures 6.2(e) and 6.2(f)) demonstrate their strong robustness to fabrication errors. Specifically, the TE-cloak can tolerate variation in device thickness of 83 nm (-32 nm to +51 nm), if the transmission efficiency is allowed to fall 1 dB from the value at design thickness (0.3 μm). The corresponding device thickness range for the TM-cloak is larger than 140 nm (-40 nm to over +100 nm). Performance for the TM-cloak with device thickness below 0.26 μm is not evaluated, since TM mode is not supported in such waveguides.

6.5 Symmetric cloaks for waveguides

As a next step, we designed cloaks that render both waveguides invisible to one another, the so-called symmetric case. The results are summarized in Figure 6.3. The average TE transmission efficiency (port 1 to port 2 or port 4 to port 3) is over -0.969 dB over a bandwidth >30 nm as indicated in Figure 6.3(j). The corresponding TM transmission efficiency is > -0.458 dB over the entire bandwidth (150 nm) as indicated in Figure 6.3(k). In both cases, the cross-talk (port 1 to port 3, port 1 to port 4, port 4 to port 1 or port 4 to port 2) is less than -12.8 dB over the entire bandwidth from 1.5 μm to 1.65 μm and the cross-talk at the design wavelength is below -22 dB.

6.6 Increasing the waveguide propagation length

Although the cloak is designed for a finite length of waveguide, we could extend the waveguides to any length simply by repeating the cloaks. To illustrate this principle, the nanophotonic cloak from Figure 6.3(d) is repeated three times with a gap of 3.3 μm, which gives a total length of 32.6 μm as shown in Figure 6.3(g). The corresponding steady-state intensity distributions are shown in Figures 6.3(h) and 6.3(i) for TM polarization with signal launched in the top (port 4) and bottom (port 1) waveguides, respectively. The signal energy is confined in the corresponding waveguide without being coupled to the neighbor even after a propagation length of 32.6 μm. The simulated transmission efficiency at 1550 nm is -0.872 dB and -0.101 dB for signal launched in the top (port 4 to port 3) and bottom (port 1 to port 2) waveguides, respectively. In both cases, the crosstalk at 1550 nm is less than -16 dB. Such propagation length and extinction ratio are sufficiently large to warrant its practical applications in PLCs. As discussed in the supplementary information, the smallest spacing between waveguides that we were able to achieve so far is 0.3 μm for TE polarization with a center-to-center spacing of 0.6 μm.

6.7 Improved optimization algorithm

As mentioned above, a propagation length of tens of microns is demonstrated without significant energy loss. Such cloak designs can find many useful applications where short cloaking distance is needed, for example in connections between neighboring integrated photonic devices or two arms of a Mach–Zehnder interferometer. We can further improve the performance by upgrading the design algorithm to a particle-swarm-based technique as described in the supplementary information. As a result, we were able to design devices with transmission efficiency as high as -0.1739 dB and -0.0017 dB for TE and TM polarizations, respectively. The -0.0017 dB transmission corresponds to a propagation loss as low as 1.41 dB/cm. These results are summarized in Figure 6.4, where the center-to-center spacing is 0.8 μm, the same as our previous devices. The simulated cross-talk is -33.8 dB and -36.9 dB for TE and TM polarizations, respectively.

Further analysis reveals that the transmission efficiency is almost independent of the length of the cloaking regions. In principle, we could design a millimeters-long cloaking region with negligible insertion loss as long as the correspondingly large computation capability is available.

6.8 Cloaking ridge waveguides

For the cloak designs mentioned above, fully etched waveguides were used. This is due to the fact that the cloak patterns can be fabricated at the same time as the waveguides, necessitating only a single lithography step. Furthermore, these are easier to fabricate, since chemical dry etching can stop at the oxide layer once the top silicon layer is etched away.

However, totally etching away the top silicon layer may be a problem when extending our method to active devices, where a thin slab layer underneath the silicon nanowire is needed to form a PN junction. In order to demonstrate the versatility of our method, cloak designs based on a ridge waveguide with a slab layer underneath are demonstrated as follows. The thicknesses of the ridge and the slab layers are 250 nm and 50 nm, respectively [25]. The center-to-center spacing of the waveguides is 0.8 μm. The designs and performance are summarized in Figure 6.5. A transmission efficiency of -0.201 dB and -0.087 dB at design wavelength (1550 nm) is achieved for TE and TM polarizations, respectively. The corresponding cross-talk is well below -23 dB for both cases. In summary, the performance is comparable to that of the fully etched waveguide-based cloaks.

6.9 Cloaking microring resonator

In addition to waveguides, the nanophotonic cloaking principle can be readily extended to resonators, to enable their very-large-scale integration. To illustrate the generality of our method, we designed a nanophotonic cloak that can render a waveguide invisible to a neighboring microring resonator. Microring resonators are commonly used in integrated channel-drop or channel-add filters [23,26-27]. In most applications, light is coupled into the resonator via a waveguide that is placed in close vicinity to the ring. However, if another waveguide is placed close to the microring, the two optical components would work as a coupled system with functionality that is different from that of either one working independently, which is illustrated in Figures 6.6(a)-(b).

We designed a nanophotonic cloak that allows a waveguide to be placed at a gap of only 300 nm from the microring and essentially renders the waveguide invisible to the micro-ring. The geometry of the device is illustrated in Figure 6.6(c). The footprint of the cloak is 0.3 μm × 6 μm. The steady-state intensity distribution for a signal launched at port 1 is shown in Figure 6.6(d). Compared to the case without the cloak (Figure 6.6(b)), almost no light is coupled into the microring. The transmission efficiency, which is defined as the fraction of light that reaches port 2, when a signal is launched at port 1 is plotted in Figure 6.6(e) as a function of wavelength (green dot-dashed line). In this case, the crosstalk is the fraction of light that reaches either port 3 or port 4, when the signal is launched at port 1. The simulated cross-talk spectra in both cases are plotted in Figure 6.6(f). The transmission efficiency at 1550 nm is 91.5%, while the corresponding crosstalk is less than 0.5%. Furthermore, the transmission efficiency is over 87.4% over the entire bandwidth ranging from 1500 nm to 1650 nm.

It is important to verify that the cloak does not interfere with the proper function of the filter for the right waveguide. The blue dashed curve in Figure 6.6(e) represents the fraction of the signal reaching port 3 when the source is at port 4. The red solid curve represents the same efficiency in the case of a microring resonator without a left waveguide. Compared to this reference, the nanophotonic cloak causes a small shift in the resonance frequency (~2 nm) and a slight change in the extinction ratio (~3 dB lower). The wavelength shift can be compensated thermally [23,27]. Although the cloak was designed to hide the microring from the left waveguide, our simulations indicate that it is fairly effective in reducing any light coupling from the right waveguide to the left waveguide through the microring.

6.10 Discussion

The mechanism of operation of our devices can be explained as follows. Evanescent waves play a key role in the coupling between neighboring optical devices. Neighboring devices can be decoupled and thus invisible to each other by minimizing the evanescent wave's penetration depth into the surrounding medium. For a light wave penetrating into the cladding layer (medium 2) as illustrated in Figure 6.7(a), the dispersion relation is [28],

$$\frac{\left(k_x^{\parallel}\right)^2}{\varepsilon_y}+\frac{\left(k_y^{\perp}\right)^2}{\varepsilon_x}=\left(k_0\right)^2 , \tag{3}$$

where $k_x^{\parallel}$ and $k_y^{\perp}$ are the parallel and perpendicular components of the wave vector in medium 2, respectively. ε_x and ε_y are the dielectric constants of the medium 2 parallel and perpendicular to the interface, respectively. k_0 is the wave vector in freespace. The evanescent wave decay constant in medium 2 is given by

$$k_y^{\perp}=\sqrt{\frac{\varepsilon_x}{\varepsilon_y}}\cdot\sqrt{\varepsilon_x\left(k_0\right)^2-\left(k_x^{\parallel}\right)^2}. \tag{4}$$

The decay rate of the evanescent waves can be enhanced by maximizing the ratio of the dielectric constant parallel to the interface to that perpendicular to the interface in the cladding layer (medium 2). The nonuniform silicon/air pillars are able to create an anisotropic cladding layer as shown in Figures 6.1(a) and 6.1(c), and our nonlinear optimization algorithm aims to maximize this ratio and thereby, minimize the evanescent wave's penetration depth into the cladding layer.

To illustrate the point, the cross-section of the electric field intensity pattern in Figure 6.4(b) as well as that of a single waveguide without the cloaking regions are shown in insets of Figure 6.7(b). The electric field intensity distributions along a straight line (blue dashed lines in the insets of Figure 6.7(b)) through the center of the waveguides are shown in Figure 6.7(b). Green shaded regions indicate the positions of waveguides. As can be seen clearly, the introduction of the anisotropic cladding layer enables the evanescent wave outside the waveguide to decay much faster and a much smaller penetration depth into the surrounding medium is observed. The mode length, given by $L_m = \int_{-\infty}^{\infty} W(x)\,dx / \max\{W(x)\}$ where $W(x)$ is the energy density of the mode [29], is 8.4 and 3.9 for waveguide with and without cloaks, respectively. This quantitatively demonstrates the anisotropic cladding layer's strong capability in suppressing the penetration of the evanescent components into the cladding layer.

6.11 Conclusion

In this paper, we designed and experimentally demonstrated the application of nanophotonic cloaking to increase the density of integrated photonics. We were able to place two single-mode waveguides at a distance of almost $\lambda_0/2$ and observe no discernible crosstalk. Furthermore, we were able to design nanophotonic cloaks that allow the placement of a single-mode waveguide next to a microring resonator at a distance less than $\lambda_0/2$ with very low crosstalk. These two examples illustrate the generality of our methodology and we emphasize that all passive devices can be cloaked in this manner, enabling a significant increase in the achievable integration density of photonic devices. The cloak design can also be used to reduce the footprint of many individual devices, e.g. integrated Mach–Zehnder interferometer with two waveguide arms by reducing the spacing between the arms.

6.12 References

[1] R. Nagarajan, C. H. Joyner, R. P. Schneider, J. S. Bostak, T. Butrie, A. G. Dentai, V. G. Dominic, P. W. Evans, M. Kato, M. Kauffman, D. J. H. Lambert, S. K. Mathis, A. Mathur, R. H. Miles, M. L. Mitchell, M. J. Missey, S. Murthy, A. C. Nilsson, F. H. Peters, S. C. Pennypacker, J. L. Pleumeekers, R. A. Salvatore, R. K. Schlenker, R. B. Taylor, M. F. Huan-Shang Tsai, J. Van Leeuwen, M. Webjorn, D. Ziari, J. Perkins, S. G. Singh, M. S.

Grubb, D. G. Reffle, F. A. Mehuys, Kish, and D. F. Welch, “Large-scale photonic integrated circuits,” IEEE J. Sel. Top. Quantum Electron. **11**(1), 50–65 (2005).

[2] L. A. Coldren and S. W. Corzine, *Diode Lasers and Photonic Integrated Circuits* (Wiley, New York, 1995).

[3] V. J. Sorger, Z. Ye, R. F. Oulton, Y. Wang, G. Bartal, X. Yin, and X. Zhang, “Experimental demonstration of low-loss optical waveguiding at deep sub-wavelength scales,” Nat. Commun. **2**, 331 (2011).

[4] W. Shin, W. S. Cai, P. B. Catrysse, G. Veronis, M. L. Brongersma, and S. H. Fan, “Broadband sharp 90-degree bends and T-splitters in plasmonic coaxial waveguides,” Nano Lett. **13**(10), 4753–4758 (2013).

[5] G. Veronis and S. H. Fan, “Bends and splitters in metal-dielectric-metal subwavelength plasmonic waveguides,” Appl. Phys. Lett. **87**(13), 131102 (2005).

[6] B. Shen, R. Polson, and R. Menon, “Integrated digital metamaterials enables ultra-compact optical diodes,” Opt. Express **23**, 10847-10855 (2015).

[7] B. Shen, P. Wang, R. Polson, and R. Menon, “An integrated-nanophotonics polarization beamsplitter with 2.4×2.4 μm^2 footprint,” Nat. Photonics **9**(6), 378–382 (2015).

[8] B. Shen, R. Polson, and R. Menon, “Metamaterial-waveguide bends with effective bend radius < λ0/2,” Opt. Lett. **40**, 5750-5753 (2015).

[9] V. J. Sorger, N. D. Lanzillotti-Kimura, R.-M. Ma, and X. Zhang, “Ultra-compact silicon nanophotonic modulator with broadband response,” Nanophotonics **1**(1), 1–6 (2012).

[10] W. S. Zaoui, A. Kunze, W. Vogel, and M. Berroth, “CMOS-compatible polarization splitting grating couplers with a backside metal mirror,” IEEE Photonics Technol. Lett. **25**(14), 1395–1397 (2013).

[11] T. Zentgraf, J. Valentine, N. Tapia, J. Li, and X. Zhang, “An optical ‘Janus’ device for integrated photonics,” Adv. Mater. **22**(23), 2561–2564 (2010).

[12] W. Song, R. Gatdula, S. Abbaslou, M. Lu, A. Stein, W. Y.-C. Lai, J. Provine, R. F. W. Pease, D. N. Christodoulides, and W. Jiang, “High-density waveguide superlattices with low crosstalk,” Nat. Commun. **6**, 7027 (2015).

[13] W. Cai, U. K. Chettiar, A. V. Kildishev, and V. M. Shalaev, “Optical cloaking with metamaterials,” Nat. Photonics **1**, 224 (2007).

[14] J. Li and J. B. Pendry, “Hiding under the Carpet: A New Strategy for Cloaking,”

Phys. Rev. Lett. **101**(20), 203901 (2008).

[15] X. Ni, Z. J. Wong, M. Mrejen, Y. Wang, and X. Zhang, "An ultrathin invisibility skin cloak for visible light," Science **349**, 1310–1314 (2015).

[16] D. C. Zografopoulos and K. P. Prokopidis, "Transparent nanoprobes in integrated plasmonic circuits based on plasmonic cloaking," Phys. Rev. Applied **2**, 064009 (2014).

[17] J. Valentine, J. Li, T. Zentgraf, G. Bartal, and X. Zhang, "An optical cloak made of dielectrics," Nat. Mater. **8**(7), 568–571 (2009).

[18] L. H. Gabrielli, J. Cardenas, C. B. Poitras, and M. Lipson, "Silicon nanostructure cloak operating at optical frequencies," Nat. Photon. **3**, 461–463 (2009).

[19] B. Shen, P. Wang, and R. Menon, "Optimization and analysis of 3D nanostructures for power-density enhancement in ultra-thin photovoltaics under oblique illumination," Opt. Express **22**(S2), A311–A319 (2014).

[20] B. Shen, P. Wang, R. Polson, and R. Menon, "Ultra-high-efficiency metamaterial polarizer," Optica **1**(5), 356–360 (2014).

[21] B. Shen, P. Wang, R. Polson, and R. Menon, "Integrated metamaterials for efficient and compact free-space-to-waveguide coupling," Opt. Express **22**(22), 27175–27182 (2014).

[22] B. Shen, R. Polson, and R. Menon, "Broadband asymmetric light transmission via all-dielectric digital metasurfaces," Opt. Express **23**, 20961-20970 (2015).

[23] L. Pavesi and G. Guillot, *Optical Interconnects - the Silicon Approach* (Springer-Verlag, Heidelberg, 2006).

[24] J. Kennedy and R. Eberhart, "Particle swarm optimization," Proc. IEEE Int. Conf. Neural Netw. 4, 1942-1948 (1995).

[25] Q. Xu, B. Schmidt, S. Pradhan, and M. Lipson, "Micrometre-scale silicon electrooptic modulator," Nature **435**, 325–327 (2005).

[26] S. T. Chu, B. E. Little, W. Pan, T. A. Kaneko, S. A. Sato, and Y. A. Kokubun, "An eight-channel add-drop filter using vertically coupled microring resonators over a cross grid," Photonics Technology Letters, IEEE **11**, 691–693 (1999).

[27] N. Sherwood-Droz, H. Wang, L. Chen, B. G. Lee, A. Biberman, K. Bergman, and M. Lipson, "Optical 4x4 hitless slicon router for optical networks-on-chip (NoC)," Opt. Express **16**(20), 15915–15922 (2008).

[28] S. Jahani and Z. Jacob, "Transparent subdiffraction optics: nanoscale light

confinement without metal," Optica **1**(2), 96–100 (2014).

[29] R. F. Oulton, V. J. Sorger, D. A. Genov, D. F. P. Pile, and X. Zhang, "A hybrid plasmonic waveguide for subwavelength confinement and long-range propagation," Nat. Photonics **2**, 496–500 (2008).

[30] L. H. Frandsen, Y. Elesin, L. F. Frellsen, M. Mitrovic, Y. Ding, O. Sigmund, and K. Yvind, "Topology optimized mode conversion in a photonic crystal waveguide fabricated in silicon-on-insulator material," Opt. Express **22**(7), 8525–8532 (2014).

[31] L. H. Frandsen, Y. Elesin, O. Sigmund, J. S. Jensen, and K. Yvind, "Wavelength selective 3D topology optimized photonic crystal devices," CLEO 2013 OSA Technical Digest CTh4 L.6 (OSA, 2013).

[32] A. Y. Piggott, J. Lu, K. G. Lagoudakis, J. Petykiewicz, T. M. Babinec, and J. Vučković, "Inverse design and demonstration of a compact and broadband on-chip wavelength demultiplexer," Nat. Photonics **9**, 374–377 (2015).

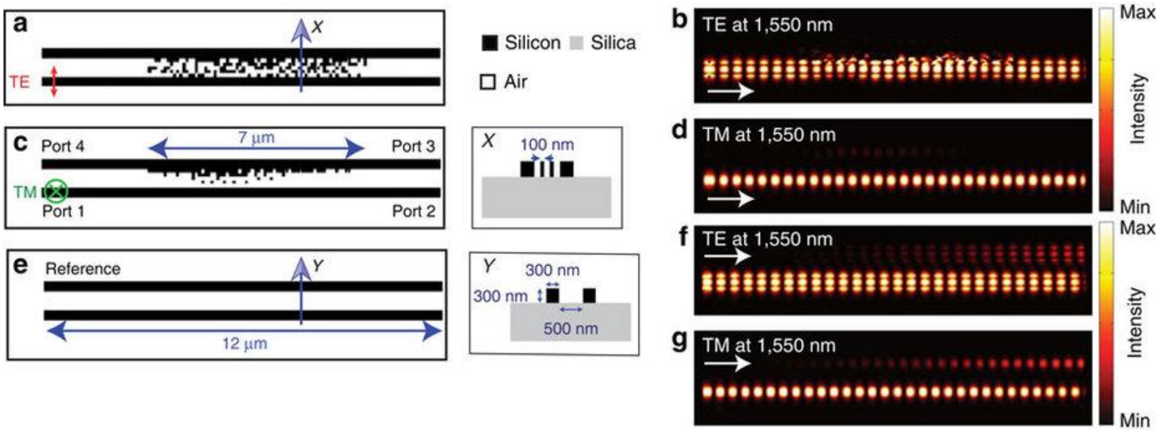

Figure 6.1. Nanophotonic cloaks for closely spaced waveguides. The geometry and the simulated steady-state intensity distribution at $\lambda_0 = 1550$ nm are shown for TE (in-plane) (a) and (b), and for TM (out-of-plane) (c) and (d) polarizations, respectively. The inset in (a) shows the cross-section of the waveguide and the nano-pillars. The corresponding images for the reference devices (without the nanophotonic cloaks) are shown in (e)-(h). In each case, light is launched in the bottom waveguide propagating from left to right. The white arrows in each figure indicate the light propagation direction.

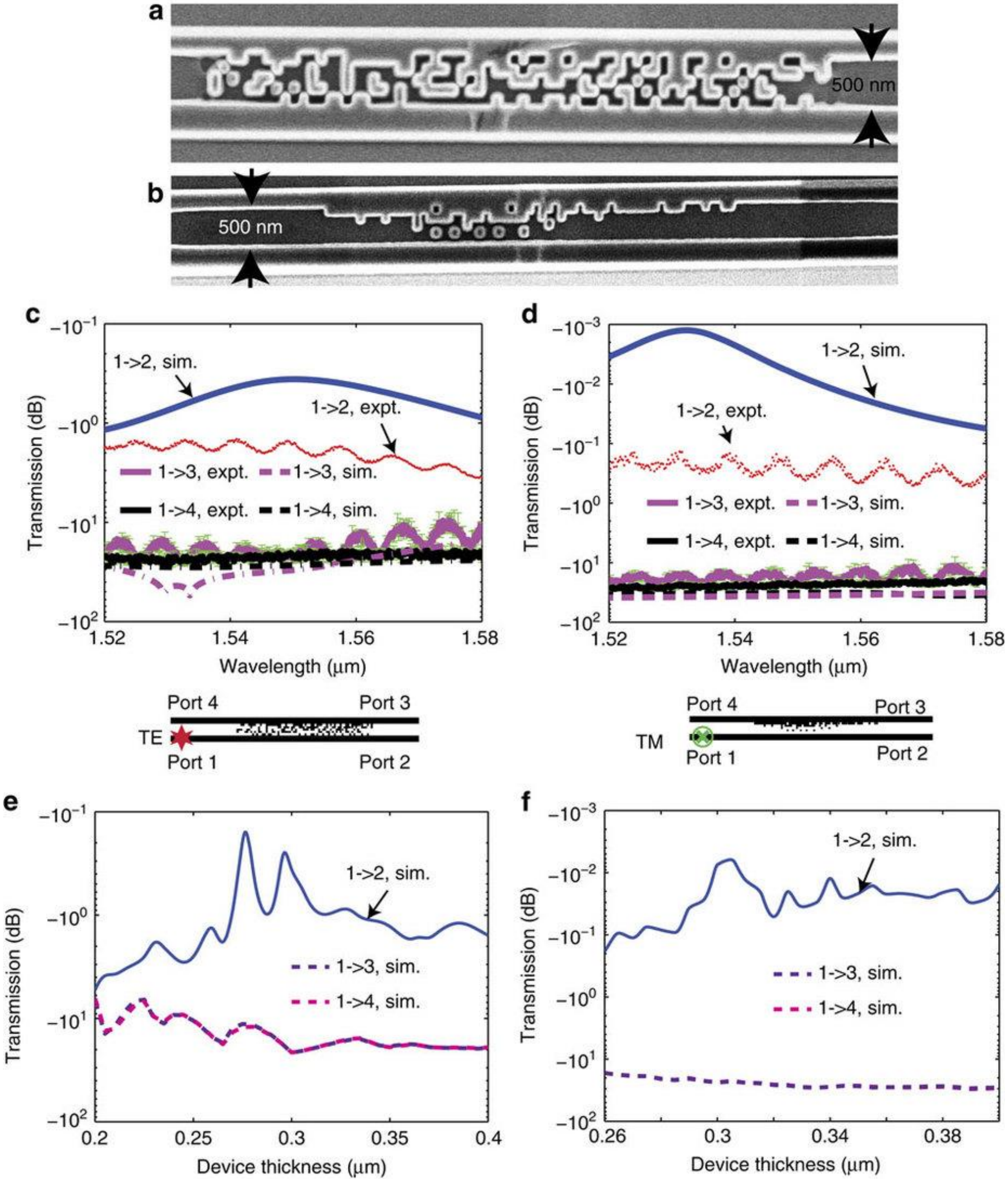

Figure 6.2. Experimental results. Scanning-electron micrographs of cloaked waveguide pairs for (a) TE and (b) TM polarizations. Simulated and measured transmission efficiencies for (c) TE- and (d) TM-cloak. Simulated transmission efficiencies for various device thicknesses for (e) TE- and (f) TM-polarizations. The naming of each port and source position is illustrated in the insets in the bottom of (c) and (d). The green error bars in (c) and (d) illustrate the fluctuation of measurement data.

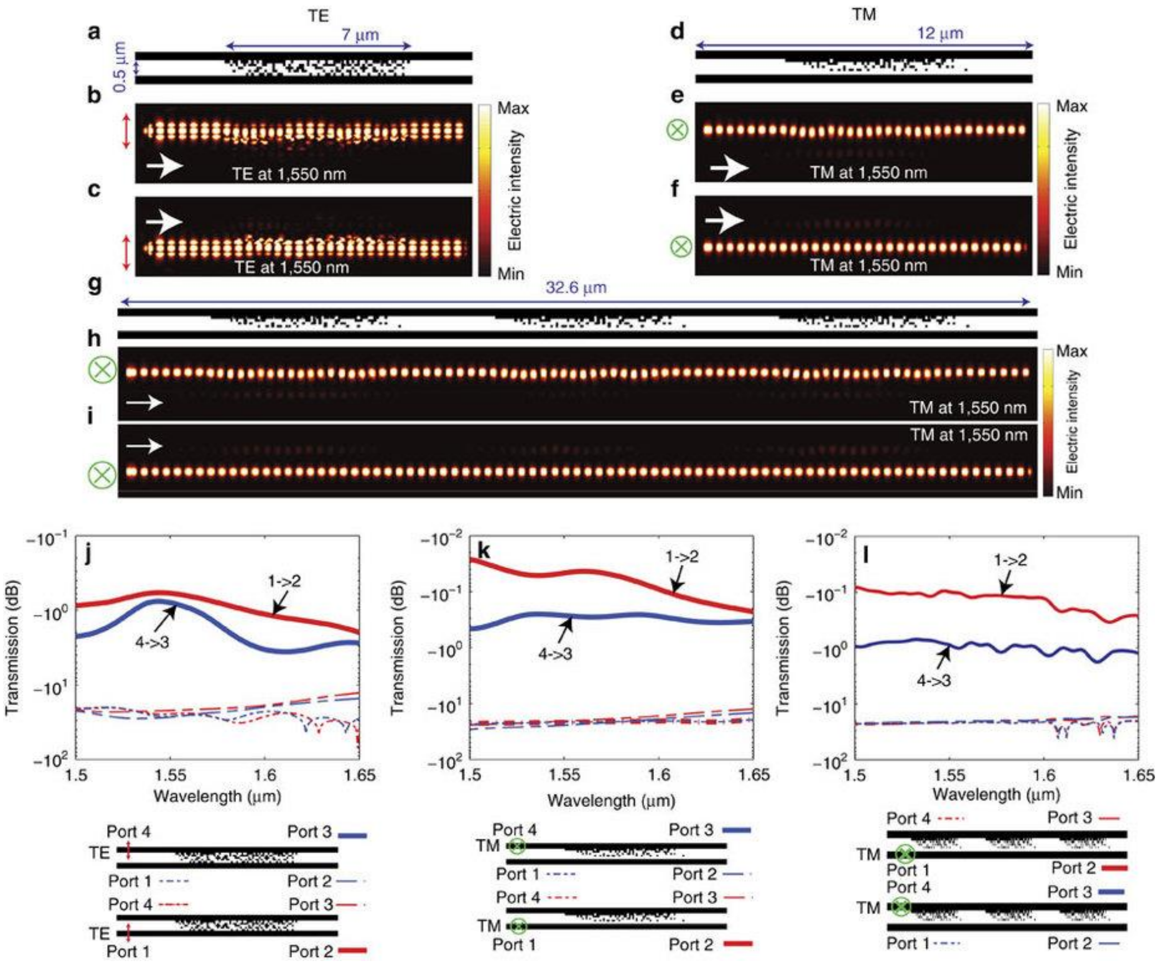

Figure 6.3. Symmetric nanophotonic cloaks for dense waveguides. The geometries of the devices are shown in (a) and (d) for TE and for TM polarizations, respectively. The simulated steady-state intensity distributions at $\lambda_0 = 1550$ nm are shown for (b) TE input at port 4, (c) TE input at port 1, (e) TM input at port 4, and (f) TM input at port 1. The simulated efficiencies are shown in (j) and (k), for TE and TM polarizations, respectively. (g) The geometry of the cloak for waveguides with three repeated units. The simulated steady-state intensity distribution at $\lambda_0 = 1550$ nm for such repeated cloaks are shown for (h) TM input at port 4, and (i) TM input at port 1. The simulated efficiencies are shown in (l). In each case, light is propagating from left to right.

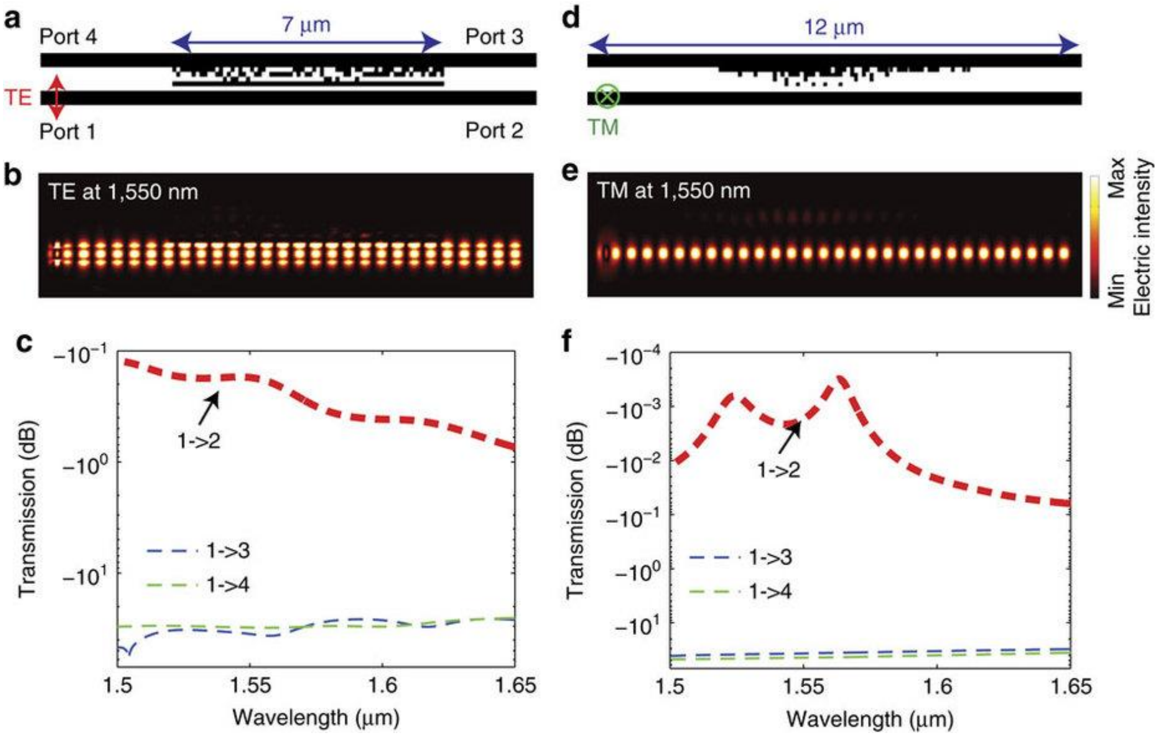

Figure 6.4. Cloak designs with upgraded algorithm. The geometry, the simulated steady-state intensity distribution at λ_0 = 1550 nm, and wavelength dependent transmission efficiencies are shown for TE (in-plane) (a), (b) and (c), and for TM (out-of-plane) (d), (e) and (f) polarizations, respectively.

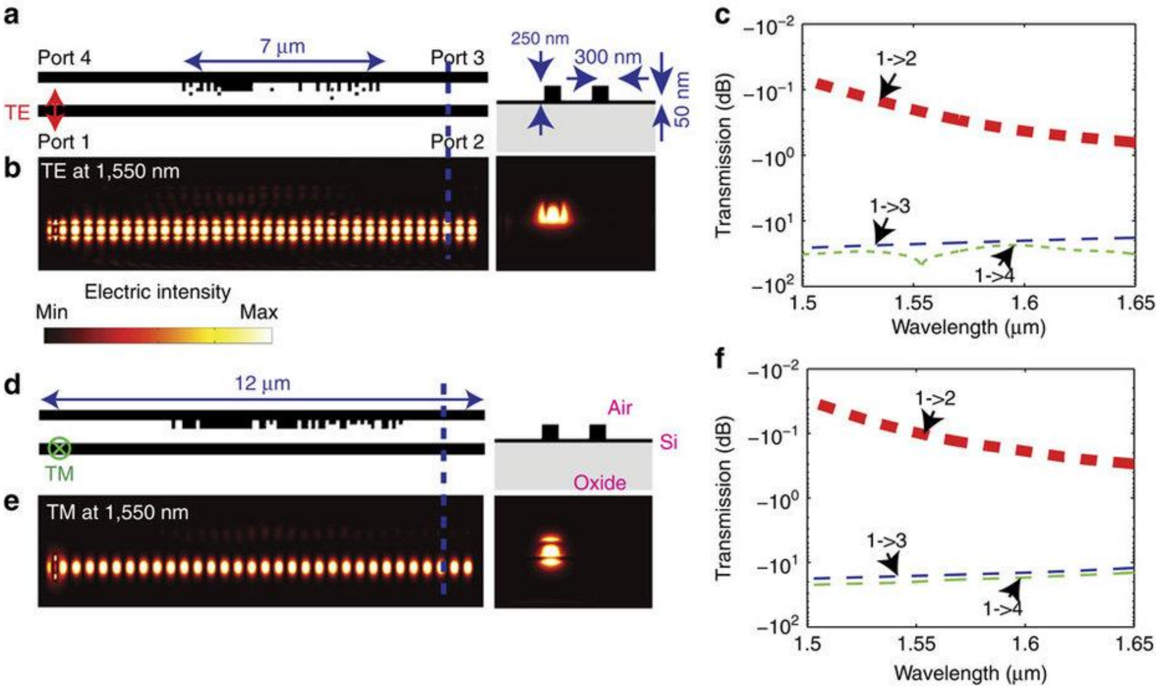

Figure 6.5. Cloak designs for ridge waveguide with a slab layer underneath. The geometries, the simulated steady-state intensity distributions at $\lambda_0 = 1550\,\text{nm}$ and wavelength-dependent transmission efficiencies are shown for TE (in-plane) (a–c) and for TM (out-of-plane) (d–f) polarizations, respectively.

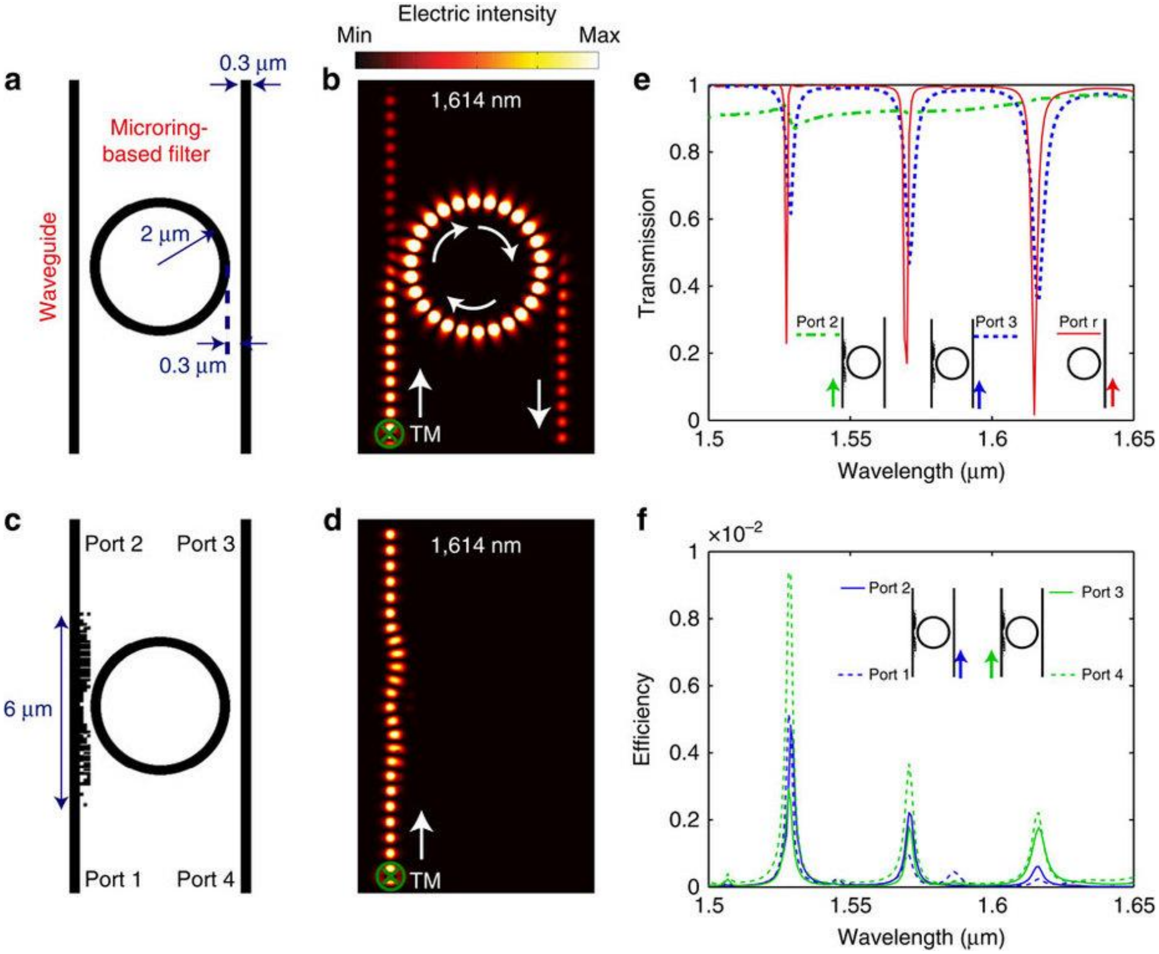

Figure 6.6. Cloak for microring resonator. (a) Geometry of the reference coupled system composed of a waveguide and a micro-ring filter. (b) Simulated steady-state intensity distribution for a when TM source is launched in the left waveguide. (c) Geometry of a system composed of a waveguide, a nanophotonic cloak and a microring. (d) Steady-state intensity distribution for the system in c when TM source is launched in the left waveguide. (e) Transmission spectra of the system in c and an individual microring filter as reference. (f) Cross-talk for the system in c.

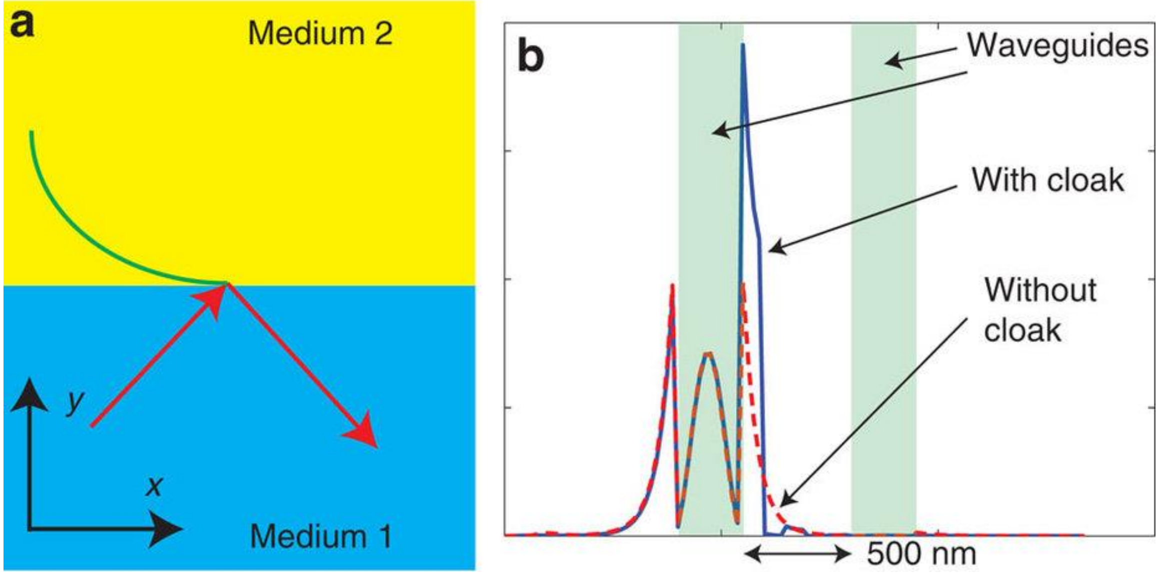

Figure 6.7. Mechanism analysis. (a) Illustration of wave propagating along a waveguide with evanescent wave penetrating from the core (medium 1) to the cladding (medium 2). (b) Steady-state intensity distribution along a line through the centre of waveguide perpendicular to the wave propagation direction. Blue solid line represents intensity distribution for cloaked waveguides. Red dashed line represents intensity distribution for a single waveguide as a reference. Green shaded regions indicate the positions of the waveguides.

CHAPTER 7

AN INTEGRATED-NANOPHOTONIC POLARIZATION BEAMSPLITTER WITH 2.4 × 2.4 μm^2 FOOTPRINT

Reprinted and adapted with permission from [B. Shen, P. Wang, R. C. Polson, and R. Menon, "An integrated-nanophotonics polarization beamsplitter with 2.4 × 2.4 μm^2 footprint," Nature Photonics **9**, 378-382 (2015).].

7.1 Abstract

We have designed, fabricated and characterized an integrated-nanophotonics polarization beamsplitter with a footprint of $2.4 \times 2.4\ \mu m^2$, which is the smallest polarization beamsplitter ever demonstrated. A nonlinear optimization algorithm was used to design the device for $\lambda_0 = 1550$ nm. The polarization beamsplitter and the input/output waveguides can be fabricated in a single lithography step. Here, we experimentally show an average transmission efficiency of greater than 70% (peak transmission efficiency of ~80%) and an extinction ratio greater than 10 dB within a bandwidth of 32 nm. Simulation results indicate that our device is tolerant to fabrication errors of up to ±20 nm in the device thickness. We also designed, fabricated and characterized a mode-converting polarization beamsplitter, which not only separates the two polarization states but also connects one multimode input waveguide to two single-mode output waveguides.

7.2 Introduction

Silicon-on-insulator (SOI) is the main materials system used in integrated photonics because of the difference in refractive index between silicon and silicon dioxide. However, this feature results in strong birefringence, which leads to polarization-sensitive performance [1]. One solution to the problem is to compensate for polarization-mode dispersion, which requires a very challenging fabrication accuracy of 1 nm (ref. 2). A better solution is to use devices that process different polarization states separately. However, this requires an efficient and compact polarization beamsplitter (PBS). The working principle underpinning conventional PBS devices is based on either modal evolution [3, 4] or interferometry. The latter typically include multimode interference couplers (MMIs) [5, 6,] directional couplers (DCs) [2, 7, 8, 9, 10, 11, 12, 13] and Mach–Zehnder interferometers

(MZIs) [14, 15]. Among these, PBS devices based on DCs are preferred, because they generally provide the smallest footprint. DCs, in general, are composed of silicon waveguides [2, 10], photonic crystals [11, 13,] slot waveguides [9] or a combination of a silicon channel and slot waveguide [7]. For DCs composed of silicon channels, Fukuda and colleagues have demonstrated a PBS with dimensions of 7 μm × 16 μm that exhibited an extinction ratio of 15 dB (ref. 2). However, the fabrication precision required for the waveguides and the gap between the waveguides is very stringent due to its underlying phase-matching principle. In addition, the fundamentally small evanescent coupling prevents it from achieving large extinction ratios. Photonic-crystal-based DCs are a plausible alternative for compact PBS devices [11, 13], but light coupling between the commonly used silicon waveguides and photonic-crystal waveguides is challenging. DCs based on slot waveguides [9] or the combination of slot waveguides and silicon channels [7] could enable the fabrication of smaller devices due to the tighter mode confinement within the slot. Combining a slot waveguide and silicon channels, Dai and co-workers designed a PBS with a length of 6.9 μm and an extinction ratio larger than 10 dB (ref. 7). Again, strict requirements for the precision of fabrication are inevitable due to its underlying phase-matching principle. Recently, Guan and colleagues proposed a DC-based PBS composed of a hybrid plasmonic waveguide and a silicon nanowire [12]. This device has dimensions of 1.9 μm × 3.7 μm, but the incorporation of metal creates significant parasitic absorption losses and renders the process complementary metal–oxide–semiconductor (CMOS) incompatible.

In contrast to previous device designs, we make use of the concept of free-form metamaterials in our PBS device. Allowing the geometry of the metamaterials to be freely optimized enables devices that can be highly functional, but which occupy a small footprint [16, 17, 18]. Nanopatterning enables one to engineer the refractive index in space at a deep sub-wavelength scale. In this way, devices that achieve high-efficiency mode conversion in an extremely small area become feasible. Furthermore, these devices tend to rely on the coupling between a number of resonant nanophotonic modes, which promotes robustness to fabrication errors, as discussed later. Here, we have designed, fabricated and characterized an ultra-compact PBS with a footprint of only $2.4 \times 2.4\ \mu m^2$ for a design wavelength of 1.55 μm and an extinction ratio larger than 12 dB. As far as we know, this is the smallest-area PBS ever demonstrated. We refer to this device as a nanophotonic PBS (see Figure 7.1 (a) for its geometry). The PBS is patterned on an SOI substrate, in which the thicknesses of the silicon and oxide layers are 0.3 μm and 3 μm, respectively. Note that the device is also CMOS-compatible.

7.3 Methods

The device is composed of 20 × 20 pixels. One pixel is in the shape of a square, with sides of 120 nm, giving a device footprint of $2.4 \times 2.4\ \mu m^2$. Unpolarized light, excited at the far end of the left input waveguide (Figure 7.1), illuminates the PBS. Transverse magnetic (TM) and transverse electric (TE) components of the input light are coupled into the top and bottom output waveguides with calculated efficiencies of 89% and 81%, respectively. The simulated intensity distributions for both polarizations are shown in Figure 7.1. From the simulations we can clearly see that the incident light generates resonant modes within the nanophotonic device that are polarization-dependent. These guided resonant modes interact in such a manner as to satisfy the phase-matching conditions for the respective polarizations at the corresponding output waveguides. As a result, polarization splitting is achieved. In the device geometry in Figure 7.1, silicon is shown in black and the absence of silicon (air) as white. The device is designed such that the thickness of the silicon layer in the nanophotonic region is the same as that in the waveguides, that is, 300 nm. This implies that our design can be fabricated in a single lithography step along with the waveguides.

The nanophotonic PBS was designed using a nonlinear search algorithm that we refer to as ‘direct-binary search’ (DBS). Previously, we have applied different versions of the DBS algorithm to design solar concentrators [19], free-space polarizers [20], integrated-photonic devices [17] and nanostructures for enhanced light absorption [21, 22], as well as to enable computational microscopy [23]. The device under consideration is discretized into hundreds of 120 nm × 120 nm silicon/air pillars, which we call ‘pixels’. Because the device has dimensions of 2.4 μm × 2.4 μm, there are 20 × 20 pixels. Each such pixel can occupy two states: silicon or air. A randomly chosen pixel is first perturbed so as to switch its state, then a figure-of-merit (FOM) is calculated. The FOM is defined as the average transmission efficiency for TE and TM polarization states. The pixel state is retained if the FOM is improved. If not, the perturbation is reversed and the algorithm proceeds to the next pixel. A single iteration comprises such inspection of all pixels. The iterations continue until the FOM does not improve further. The algorithm seamlessly accounts for the limitations of the fabrication technologies because of the discrete pixels. Specifically, the fabrication process determines the size of the smallest feature, which, in our device, is the pixel. Although the computational cost of this step is high, we have previously reported a variety of approaches to parallelize and increase the computational efficiency [17]. In general, it took about 140 h to design one device. The electromagnetic fields within the device were simulated using a finite-difference time-domain (FDTD) method [24].

7.4 Experiment and results

As mentioned already, the device was patterned in the top silicon layer (thickness, 300 nm) of an SOI substrate. In principle, only one patterning step is required for the waveguides and the nanophotonic PBS, because their etch depths are the same. However, because we do not have access to high-resolution optical-projection lithography, we opted for a two-step process. Optical patterning was first used to define all features down to a size of 3 μm. Second, focused-ion-beam lithography was used to define all the smaller features. Alignment marks were used to ensure that the patterns defined by the two lithographic steps were aligned with one another. Further details of the fabrication process are provided in Supplementary Section 7.6. Reference devices that included the same tapers as the PBS devices for normalization, as well as an on-chip polarizer for polarization state alignment, were also fabricated on the same substrate.

A scanning electron micrograph of the fabricated device is shown in Figure 7.2. Light was input and output via butt-coupling of lensed fibres to multimode waveguides (Figure 7.2). To increase the coupling efficiency we incorporated tapers (4 μm length) between all single-mode waveguides and the multimode waveguides (width, 3 μm) [25]. The fibres used in the experiment were standard single-mode lensed fibres. Polarization controllers (PC1 and PC2) were first calibrated using the on-chip polarizer. The entire output path within the dotted frame in Figure 7.2 was first bypassed by connecting the output lensed fibre to the detector, and the on-chip polarizer was aligned. By adjusting PC1 and monitoring the output power, the input polarization state was set. The input lensed fibre was then moved to illuminate a straight waveguide, and the output path within the dotted frame was connected. The alignment between the output polarization plane and the polarizer was achieved by adjusting PC2. The polarization components of the output light could be selected by rotating the polarizer.

The experimental and simulated transmission efficiency and extinction ratio as a function of input wavelength are shown in Figure 7.3. The experimental data are normalized to those for a straight waveguide with the same tapers. The measured values consistently follow the simulated curves. The decrease in measured efficiencies can be primarily attributed to small errors introduced during fabrication, which include device thickness errors and line-edge roughness. The latter can cause out-of-plane scattering, which will reduce overall efficiencies. Improved fabrication processes can significantly reduce these effects. We believe that coherent interactions between light reflected from the lensed fibre and that from the waveguides cause the ripples in the measured spectra. We measured TE and TM coupling efficiencies of 71% and 80% at the design wavelength (1.55 μm), respectively. The measured TE and TM extinction ratios at the design wavelengths are 11.8 dB and 11.1 dB, respectively.

7.5 Discussion

The operational bandwidth of our device, where the transmission efficiency is within 1 dB of the peak value, is 83 nm (1510–1593 nm) (Figure 7.3). Such a large operating bandwidth is possible because the polarization-selection effect is the cumulative effect of a number of guided-mode resonances (rather than a single resonance).

To elucidate the tolerance of our device to small changes in device geometry, we simulated the impact of varying the top silicon thickness on device performance. The results for transmission efficiency and extinction ratio are illustrated in Figure 7.3. If the extinction ratio is allowed to fall 3 dB from the peak value, the devices can tolerate a variation in top silicon thickness of up to ±20 nm.

We also simulated the instantaneous field distributions within the PBS as a function of time. Both TE and TM modes in the input waveguide illuminate the PBS. The nanophotonic device is composed of geometries that are much smaller than the wavelength, so the excited modes are evanescent. However, power is coupled between the evanescent modes due to the close spacing. This results in multiple resonant modes that transfer power in a highly polarization-sensitive manner. Our design methodology essentially encourages the power transfer of one polarization into one waveguide, while the power in the orthogonal polarization is transferred to the second waveguide.

A closer look at the mode evolution with time shows that different mechanisms are responsible for guiding light in the two polarization states. For TE light (light polarized in-plane and vertical to the direction of light propagation), power is confined in the air gap between adjacent nanopillars and the slot–waveguide effect dominates due to boundary conditions. The silicon pillars actually act as the cladding layer and the air gaps act as the core layer to guide TE light. The opposite holds true for TM light (light polarized out-of-plane), in that the air gaps act as the cladding layer and the silicon pillars act as the core layer to guide TM light. The complementary guiding mechanisms are employed by the optimization algorithm to design the PBS to direct different polarization states to their corresponding output waveguides.

7.6 Mode-converting PBS

Complex nanophotonic structures allow one to design a single device that can implement multiple functions. To illustrate this concept, we designed, fabricated and characterized a device that not only coverts light from a multimode waveguide to a single-mode waveguide, but also splits the two polarizations. The device geometry is illustrated in Figure 7.4, and a scanning electron micrograph of the fabricated device is shown in Figure 7.4. A 3-μm-wide multimode waveguide is used as the input, and the output comprises two single-mode (440-nm-wide) waveguides. Due to the significant dimension mismatch between the input and output waveguides, mode conversion is required, which is typically achieved with a very long (hundreds of micrometres) adiabatic taper [16, 26]. For our device, however, polarization splitting and mode conversion are achieved simultaneously. The simulated intensity distributions for the two polarization states are summarized in Figure 7.4.

The simulated and measured properties of the device are summarized in Figure 7.5. The simulated transmission efficiencies at the design wavelength (1.55 μm) for TE and TM modes are calculated as 80% and 83%, respectively. The corresponding simulated extinction ratios are 15.2 dB and 14.4 dB for TE and TM. The measured transmission-efficiency and extinction-ratio spectra are lower than the simulated spectra, but substantially agree. The measured peak transmission efficiencies for TE and TM are 58% and 71%, and the measured extinction ratios are 13.88 dB and 13.77 dB, respectively. The measured efficiencies are lower than expected primarily due to errors in alignment between the PBS and the waveguides. With a single-step lithography process, such alignment will be unnecessary and these errors should not manifest. Note that both polarization separation and mode conversion are achieved within the 4 μm × 3 μm device area.

The impact of device geometry errors was also simulated to evaluate the tolerance of our design, and the results are summarized in Figure 7.5. Specifically, we varied the device (silicon layer) thickness and then evaluated its performance. The simulations indicate that if the extinction ratio is allowed to fall 3 dB from the peak, then the silicon layer thickness can vary by as much as ±17 nm.

7.7 Conclusion

In conclusion, we have designed an ultracompact integrated nanophotonic PBS using a nonlinear search algorithm based on direct-binary search. Our design methodology readily incorporates the limitations of fabrication, so our devices tend to be robust and can easily be made compatible with CMOS fabrication processes. We have characterized the devices and experimentally demonstrated TE and TM transmission efficiencies of 71% and 80%, respectively, with corresponding extinction ratios of 11.8 dB and 11.1 dB. The $2.4 \times 2.4\ \mu m^2$ footprint of our PBS makes it the smallest integrated PBS demonstrated to date [12]. Furthermore, our device demonstrates a larger operating bandwidth and higher tolerance to errors introduced during fabrication. Finally, we have also designed, fabricated and characterized a mode-converting PBS that not only separates the polarization states but also efficiently transforms the input power from a multimode waveguide to an output single-mode waveguide. The concept of free-form metamaterials demonstrated experimentally here can easily be applied to most photonic devices to drastically decrease their footprint without compromising their efficiency or functionality.

7.8 References

[1] C. Manolatou, S. G. Johnson, S. Fan, P. R. Villeneuve, H. A. Haus, and J. D. Joannopoulos, “High density integrated optics,” J. Lightwave Technol. **17**(9), 1682–1692 (1999).

[2] H. Fukuda, K. Yamada, T. Tsuchizawa, T. Watanabe, H. Shinojima, and S. Itabashi, "Ultrasmall polarization splitter based on silicon wire waveguides," Opt. Express

14(25), 12401-12408 (2006).

[3] W. Yuan, K. Kojima, B.Wang, T. Koike-Akino, K. Parsons, S. Nishikawa, and E. Yagyu, “Mode-evolution-based polarization rotator-splitter design via simple fabrication process,” Opt. Express **20**(9), 10163–10169 (2012).

[4] M. R. Watts, H. A. Haus, and E. P. Ippen, "Integrated mode-evolution-based polarization splitter," Opt. Lett. **30**(9), 967-969 (2005).

[5] J. M. Hong, H. H. Ryu, S. R. Park, J. W. Jeong, S. G. Lee, E.-H. Lee, S.-G. Park, D. Woo, S. Kim, and B.-H. O, “Design and fabrication of a significantly shortened multimode interference coupler for polarization splitter application,” IEEE Photon. Technol. Lett. **15**(1), 72–74 (2003).

[6] Z. Tu, Y. W. Huang, H. X. Yi, X. J. Wang, Y. P. Li, L. Li, and W. W. Hu, "A compact SOI polarization beam splitter based on multimode interference coupler," Proc. SPIE **8307**, 830707 (2011).

[7] D. Dai, Z. Wang, and J. E. Bowers, "Ultrashort broadband polarization beam splitter based on an asymmetrical directional coupler," Opt. Lett. **36**(13), 2590-2592 (2011).

[8] J. Feng and Z. Zhou, “Polarization beam splitter using a binary blazed grating coupler,” Opt. Lett. **32**(12), 1662–1664 (2007).

[9] Y. Yue, L. Zhang, J.-Y. Yang, R. G. Beausoleil, and A. E. Willner, “Silicon-on-insulator polarization splitter using two horizontally slotted waveguides,” Opt. Lett. **35**(9), 1364–1366 (2010).

[10] I. Kiyat, A. Aydinli, and N. Dagli, “A compact silicon-on-insulator polarization splitter,” IEEE Photon. Technol. Lett. **17**(1), 100–102 (2005).

[11] H. Fukuda, K. Yamada, T. Tsuchizawa, T. Watanabe, H. Shinojima, and S. Itabashi, “Ultrasmall polarization splitter based on silicon wire waveguides,” Opt. Express **14**(25), 12401–12408 (2006).

[12] T. Liu, A. R. Zakharian, M. Fallahi, J. V. Moloney, and M. Mansuripur, “Design of a compact photonic-crystal-based polarizing beam splitter,” IEEE Photon. Technol. Lett. **17**(7), 1435–1437 (2005).

[13] X. Guan, H. Wu, Y. Shi, L. Wosinski, and D. Dai, "Ultracompact and broadband polarization beam splitter utilizing the evanescent coupling between a hybrid plasmonic waveguide and a silicon nanowire," Opt. Lett. **38**(16), 3005-3008 (2013).

[14] M. Sesay, X. Jin, and Z. Ouyang, "Design of polarization beam splitter based on coupled rods in a square-lattice photonic crystal," J. Opt. Soc. Am. B **30**(8), 2043-2047

(2013).

[15] D. Dai, Z. Wang, J. Peters, and J. E. Bowers, “Compact polarization beam splitter using an asymmetrical mach–zehnder interferometer based on silicon-on-insulator waveguides,” IEEE Photon. Technol. Lett. **24**(8), 673–675(2012).

[16] L. B. Soldano, A. I. de Vreede, M. K. Smit, B. H. Verbeek, E. G. Metaal, and F. H. Green, “Mach-zehnder interferometer polarization splitter in ingaasp/inp,” IEEE Photon. Technol. Lett. **6**(3), 402–405 (1994).

[17] J. Lu and J. Vučković, “Nanophotonic computational design,” Opt. Express **21**(11), 13351–13367 (2013).

[18] B. Shen, P. Wang, R. Polson, and R. Menon, "Integrated metamaterials for efficient and compact free-space-to-waveguide coupling," Opt. Express **22**(22), 27175-27182 (2014).

[19] A. Y. Piggott, J. Lu, T. M. Babinec, K. G. Lagoudakis, J. Petykiewicz, J. Vučković, “Inverse design and implementation of a wavelength demultiplexing grating coupler,” Sci. Rep. **4**, 7210 (2014).

[20] G. Kim, J.-A. Dominguez-Caballero, H. Lee, D. J. Friedman, and R. Menon, “Increased photovoltaic power output via diffractive spectrum separation,” Phys. Rev. Lett. **110**(12), 123901 (2013).

[21] G. Kim and R. Menon, “An ultra-small three dimensional computational microscope,” Appl. Phys. Lett. **105**(6) 061114 (2014).

[22] B. Shen, P. Wang, R. Polson, and R. Menon, "Ultra-high-efficiency metamaterial polarizer," Optica **1**(5), 356-360 (2014).

[23] P. Wang and R. Menon, “Optimization of generalized dielectric nanostructures for enhanced light trapping in thin-film photovoltaics via boosting the local density of optical states,” Opt. Express **22**(S1), A99–A110 (2014).

[24] B. Shen, P. Wang, and R. Menon, “Optimization and analysis of 3D nanostructures for power-density enhancement in ultra-thin photovoltaics under oblique illumination,” Opt. Express **22**(S2), A311–A319 (2014).

[25] A. F. Oskooi, D. Roundy, M. Ibanescu, P. Bremel, J. D. Joannopoulos, and S. G. Johnson, “MEEP: A flexible free-software package for electromagnetic simulations by the FDTD method,” Comput. Phys. Commun. **181**(3), 687–702 (2010).

[26] L. Liu, Y. Ding, K. Yvind, and J. M. Hvam, "Efficient and compact TE–TM polarization converter built on silicon-on-insulator platform with a simple fabrication process," Opt. Lett. **36**(7), 1059-1061 (2011).

[27] W. Bogaerts, D. Taillaert, B. Luyssaert, P. Dumon, J. Van Campenhout, P. Bienstman, D. Van Thourhout, R. Baets, V. Wiaux, and S. Beckx, "Basic structures for photonic integrated circuits in Silicon-on-insulator," Opt. Express **12**(8), 1583-1591 (2004).

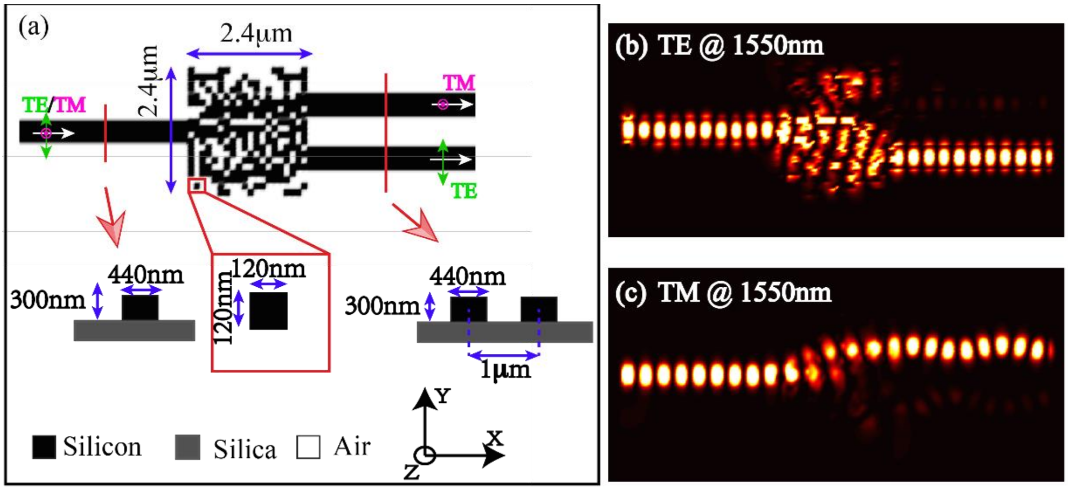

Figure 7.1. (a) Geometry of the device. (b) and (c) Simulated steady-state intensity distributions for TE (b) and TM (c) polarized light at the design wavelength of 1550 nm. TE is polarized in-plane and perpendicular to the propagation direction, as illustrated by the green arrows in a, and TM is polarized out-of-plane, as illustrated by red circles in (a).

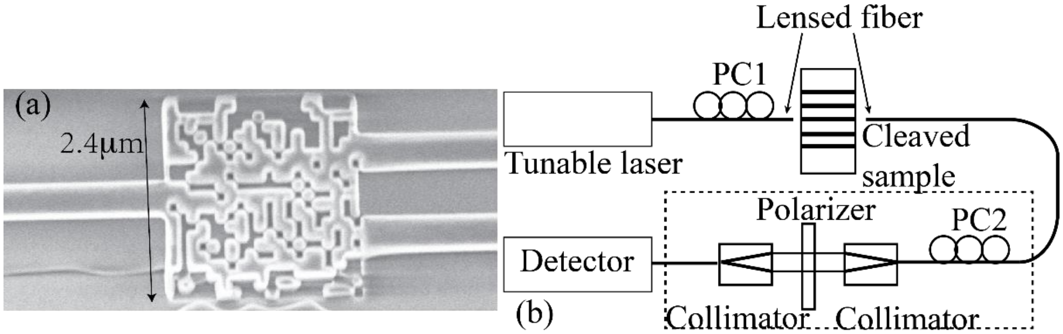

Figure. 7.2. (a) Scanning electron micrograph of the fabricated device. (b) Measurement system set-up.

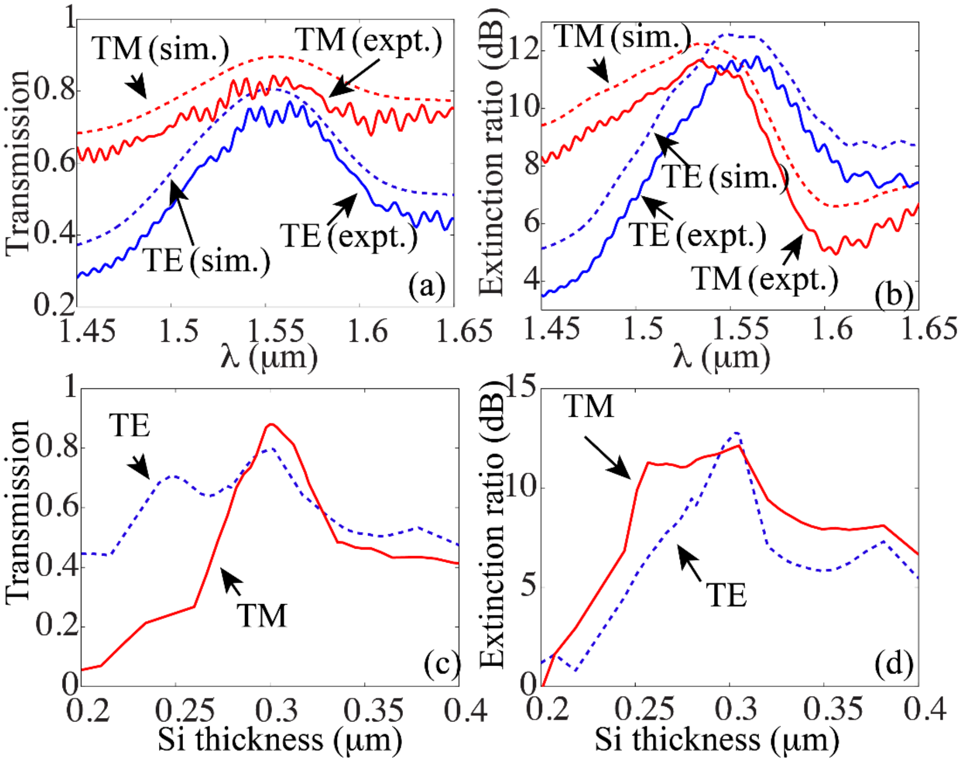

Figure. 7.3. Measured and simulated transmission efficiencies (a) and extinction ratios (b) of the PBS for both TE and TM polarization. Measured (expt.) and simulated (sim.) data are shown using solid and dashed lines, respectively. Simulated transmission efficiencies (c) and extinction ratios (d) as a function of device (silicon) thickness. For all figures, TE and TM polarizations are shown in blue and red, respectively.

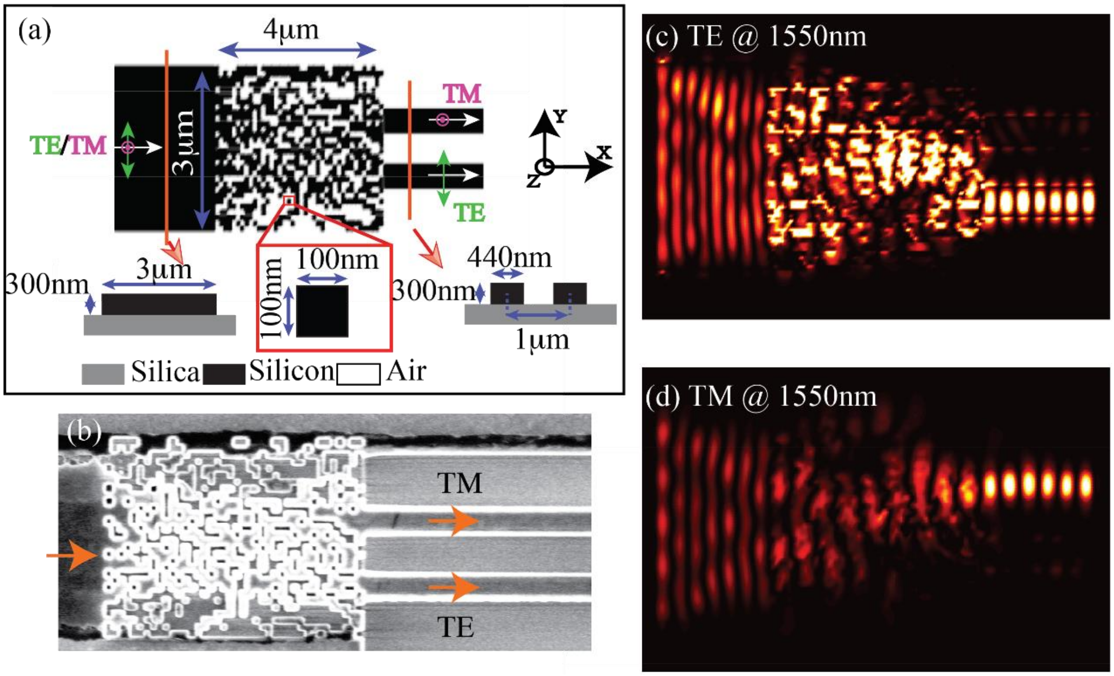

Figure 7.4. Configuration (a) and scanning electron micrograph (b) of the mode-converting PBS. Intensity distributions for TE (c) and TM (d) polarized light at 1550 nm.

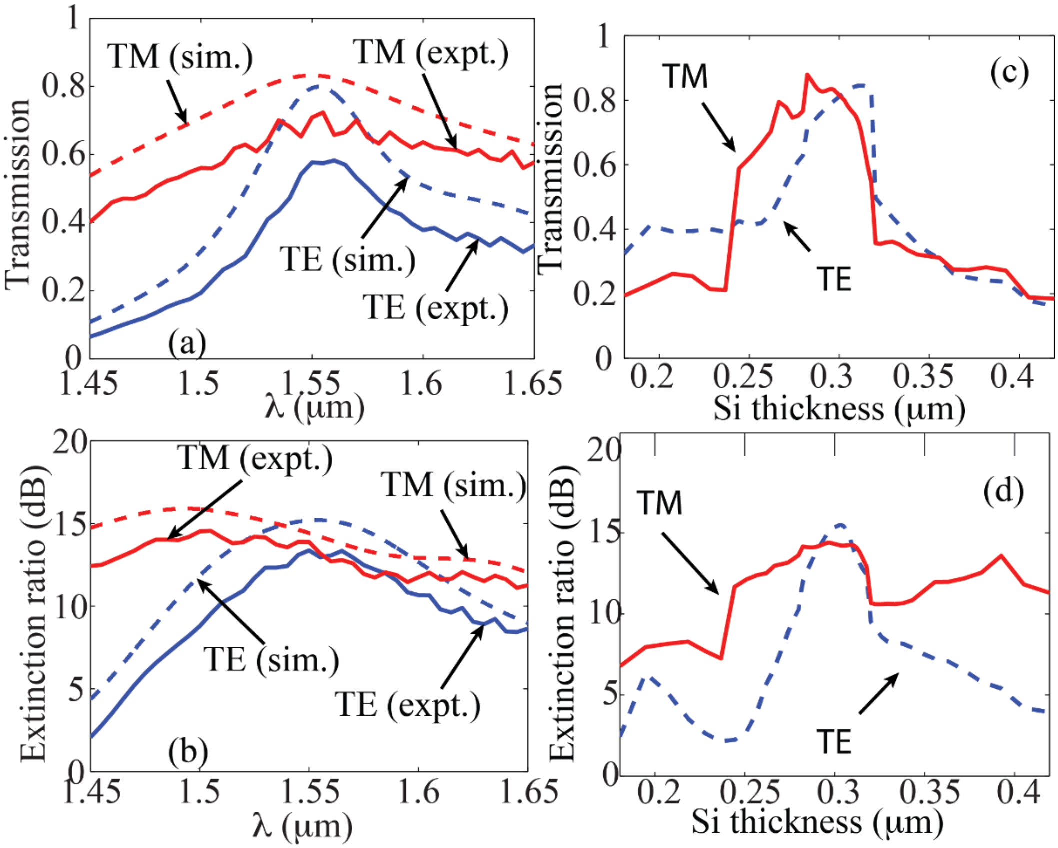

Figure 7.5. (a) Simulated and measured transmission efficiencies as a function of wavelength. (b) Simulated and measured extinction ratio as a function of wavelength. TE and TM are denoted by blue and red lines, and dashed and solid lines represent the corresponding simulation and experimental efficiencies. Simulated transmission efficiency (c) and extinction ratio (d) as a function of silicon thickness.

CHAPTER 8

BROADBAND ASYMMETRIC LIGHT TRANSMISSION VIA ALL-DIELECTRIC DIGITAL METASURFACES

Reprinted and adapted with permission from [B. Shen, R. C. Polson, and R. Menon, “Broadband asymmetric light transmission via all-dielectric digital metamaterials,” Opt. Express **23**(16) 20961-20970 (2015).]. ©2015 Optical Society of America.

8.1 Abstract

We demonstrate broadband asymmetric transmission or optical-diode behavior via a digital metasurface, that is, a surface that is digitally patterned at subwavelength dimensions. Enhanced light-matter interactions at the interfaces of the metasurface break the symmetry in the propagation direction, and enables high light-transmission in one direction, while strongly reflecting the light in the opposite direction. We measured a peak extinction ratio of 11.18 dB and peak forward transmission efficiency of 74.3% at the design wavelength of 1.55 μm. The operational bandwidth of the device was 201 nm. We further designed, fabricated and experimentally characterized a digital metasurface that enables polarization-independent optical-diode behavior, which we believe is the first device of its kind. Our digital metasurfaces enable the optical-diode behavior in a single layer of sub-wavelength thickness for several input modes and therefore, can perform as a passive, albeit imperfect optical isolator.

8.2 Introduction

Metamaterials are artificially structured materials that are engineered to exhibit extraordinary electromagnetic responses, e.g. asymmetric transmission [1,2], negative index [3] and ultraslow speed of light [4], that are not found in natural materials. Asymmetric transmission or optical-diode behavior is one such property that has recently been studied due to its potential applications in directionally-sensitive beam splitting [5], multiplexing [6], and optical interconnection [7]. The asymmetric transmission of both circular and linearly polarized light in three-dimensional (3D) volumetric metamaterials have been widely reported [8–12]. Bi-layered chiral metamaterials consisting of periodic split-rings were used to demonstrate asymmetric transmission of circular polarized light

[8]. 3D chiral metamaterials consisting of a layer of L-shaped metallic particles and another layer of straight nanowires were used to demonstrate asymmetric transmission of linearly polarized light [9]. A hyperbolic metamaterial that behaves as an optical diode for linear polarized light at visible frequencies was recently reported [10]. Besides volumetric metamaterials, bulky gratings were also employed to achieve asymmetric transmission [13–15]. The combination of a one-dimensional (1D) photonic bandgap structure and a two-dimensional (2D) periodic multilayer grating was employed to achieve unidirectional transmission [13]. In addition, employing four cascaded air-filled metal slits, Lockyear et al. showed asymmetric transmission [14]. However, fabrication and alignment associated with all these 3D devices are challenging. Besides, the parasitic absorption of metal significantly reduces their transmission efficiency. For the device proposed by Lockyear et al., the insertion loss is around −4 dB [14]. Another recent demonstration of optical-diode behavior utilized a planar chiral metamaterial (a chiral metasurface), which considerably simplified the fabrication and alignment challenges associated with the 3D metamaterials [16]. Other examples of 2D optical diodes for circular polarized light have also been reported [1,17,18]. These devices operate under the principle of symmetry breaking for circular polarized light in the transverse direction [1,2,18]. However, such symmetry breaking is more difficult for linearly polarized light, although it does not violate Lorentz's reciprocity theorem. Chiral metasurfaces preserves symmetry in the propagation direction and they are only chiral in the transverse plane [19]. Therefore, they do not exhibit asymmetric transmission for linear polarized light. However, it has been reported that the supporting substrate can break the mirror symmetry for any planar structure perpendicular to the propagation direction [20]. Furthermore, by introducing giant optical activity in

metasurfaces, it is possible to have them behave as effective 3D metamaterials [21–24]. The enhanced light-matter interaction results in significant nonlocal optical effects seeded by the small, but finite asymmetry at the air-metasurface and the metasurface-substrate interfaces. Using these ideas, polarization rotation of linearly polarized light using chiral metasurfaces have been demonstrated [21]. Broken time reversal of light propagation at chiral metasurfaces has also been demonstrated previously [23]. These demonstrations utilized metals or other lossy materials. However, the principle of symmetry breaking is valid for lossless systems as well [9], as long as giant optical activity is introduced. Recently, it was proposed that enhanced light-matter interactions are feasible at low-loss all-dielectric metasurfaces [25].

8.3 Methods

Here, we realize asymmetric transmission of linearly polarized light using a dielectric (lossless) metasurface employing the concept of digital metamaterials [26–28]. In fact, our device is not only lossless, but CMOS compatible as well. The insertion loss of previous such devices that incorporate metals is in the order of −10 dB [10]. While the insertion loss for our dielectric metasurface is estimated to be −1.3 dB. Furthermore, our device considerably simplifies the fabrication process, since only a single etch step is required, and metal deposition or precise alignment steps can be avoided. Asymmetric transmission in the THz or microwave regions have been widely reported, but not in the infra-red (IR). Our device operates at the very useful IR wavelength of ~1550 nm. Here, we note that our device is a passive device and hence does not break Lorentz symmetry. As a result, it works only for a limited incidence angle range (~15°, as discussed later). A perfect optical isolator, which exhibits asymmetric transmission for all incidence angles, requires nonlinearities. However, the divergence angle of Gaussian beams in many practical applications is typically less than 15° and our device could be quite useful in these cases. The basic premise of digital metamaterials is that via nanofabrication, one can control the local refractive index. By spatial engineering of the refractive index at subwavelength dimensions, it is possible to design structures, whose dispersion properties can be engineered efficiently, for instance to enable high-efficiency polarizers [27], ultracompact devices [26], or strong light-material interactions. Furthermore, these devices rely on the coupling between multiple resonant modes, which promotes robustness to fabrication errors, as discussed later. Here, we extend the idea of digital metamaterials to patterned 2D surfaces or digital metasurfaces. Specifically, we designed a digital metasurface that allows linearly polarized light to propagate in one direction but not in the opposite direction. Our device is made of etched silicon and is comprised of a unit cell that is tiled across the 2D plane. The designed structure of one unit cell is illustrated in Figure 8.1(a). For computational simplicity, we chose our unit cell to be 4 μm × 4 μm comprising of 20 × 20 pixels, each pixel of size 200 nm × 200 nm. The designed etch depth is 330 nm, which is considerably smaller than the design free-space wavelength, 1550 nm. The simulated steady-state intensity distributions at 1550 nm for the forward and the backward directions are shown in Figures 8.1(b) and 8.1(c), respectively. We calculated the extinction ratio, defined as the ratio of transmission efficiency in the forward direction to that in the backward direction, of 14.8 dB. The large extinction ratio warrants its practical applications. This is at least comparable to, if not better than, those previously reported for linear polarization [1,9–11]. Actually, device with even higher extinction ratio can be expected with careful selecting the parameters of our optimization algorithm.

8.4 Experiment and results

In order to characterize the digital metasurface, we illuminated it with collimated linearly polarized light from a NIR laser centered at 1550 nm. Opaque gold masks surrounded the metasurface, which blocked the incident light outside the device. The gold windows were slightly larger than the device for ease of alignment. The transmitted power was collected using an imaging lens and a standard photodiode germanium power sensor. A conventional polarizer was placed between the lens and the detector to select the polarization state of the signal. A half-wave plate and a polarizer were used at the input to first align the direction of polarization to the X-axis of the digital metasurface. The measurement setup is illustrated in Figure 8.2.

The digital metasurface was fabricated by etching into silicon using focused-ion-beam lithography. We used an ion beam energy of 30 kV and current of 7.7 pA to etch the structures with a target depth of 330 nm. Details of the fabrication process were previously reported in [26]. Figure 8.3(a) shows the scanning-electron micrograph of a fabricated device composed of 4 × 4 unit cells, where each unit cell is 4 μm × 4 μm (denoted by dashed red lines). A magnified view of one unit cell is shown in Figure 8.3(b).

Our metasurface is patterned on one side of a double-side polished Si substrate. We used an unpatterned double-side polished Si substrate as the reference. The measured and the simulated forward and backward transmission efficiencies, normalized to the transmitted intensities of the reference (we refer to this as the transmission enhancement), are shown in Figure 8.3(c). The experiments cover the tunable bandwidth of our laser source, while the simulations cover a much larger bandwidth. Although there are small discrepancies between the measured and the simulated values, they agree well overall. The discrepancies are likely due to the small polarization state misalignment and suboptimal light coupling between the metasurface and the detector. We measured an extinction ratio of 11.18 dB at 1550 nm. The transmission enhancement at the design wavelength (1.55 μm) is measured to be 1.07, which corresponds to an absolute transmission efficiency of 74.3% and an insertion loss of −1.3 dB. Note that the measured transmission enhancement is larger than 1 at some wavelengths. This means that light transmission is enhanced at the meta-surface when compared to the unpatterned Si wafer.

From the simulated transmission enhancement plot shown in Figure 8.3(c), the 3dB bandwidth (where the extinction ratio is higher than half of the peak value) of the metasurface is estimated to be 201 nm (1420 nm to 1621 nm). Compare this to a previously reported device, whose bandwidth is only tens of nanometers [10]. Our device exhibits larger bandwidth due to the fact that coherent interactions between multiple coupled guided modes is responsible for the asymmetric transmission. The multiple resonances enable the device to be less sensitive to wavelength shifts.

We also numerically investigated the device's sensitivity to fabrication errors. Specifically, we varied the etch depth of the metasurface and calculated the forward and backward transmission enhancement spectra as shown in Figure 8.3(d). If we can tolerate a 3 dB drop of extinction ratio from the peak value, we can allow the etch depth of the metasurface to vary by as much as 95 nm (−15 nm to 80 nm). Therefore, our digital metasurface is highly tolerant to fabrication errors as well.

Although our device was designed for normal incidence, we simulated the impact of oblique incidence (or higher order modes) on the performance of the device. Since the metasurface is anisotropic in transverse plane, we investigate its performance under oblique incidence with projection both on X axis and Y axis as illustrated in Figure 8.4. Figure 8.4(a) shows the extinction ratio as a function of incident angle for *k* vector projection both on X and Y axis. The two types of oblique incident angle are illustrated in Figure 8.4(b). For k_x, an angle variation of 15° about the normal would bring a 3 dB drop of the extinction ratio. While for k_y, the corresponding angle variation is 10°.

8.5 Explanation

We also simulated the time evolution of the electric field within the metasurface for linearly polarized light in order to visualize its performance. Due to the subwavelength structures within the device, guided resonance modes are excited within the metasurface. For forward direction, propagating modes are excited at the metasurface-silicon interface and propagate readily into silicon. For the backward direction, primarily evanescent modes are excited at the metasurface-air interface, and therefore, penetrate only a small distance into the air. This asymmetry gives rise to the drastic difference in transmission efficiencies in the two directions.

The specific arrangement of pixels in our digital metasurface interact with incident light such that the excited guided-mode resonances result in light propagation in only one direction. This can be contrasted against a completely random digital metasurface, where no such asymmetric-light transmission is observed, which is shown in Figure 8.5. Furthermore, the guided-mode resonances in the designed digital metasurface leads to giant light-matter interactions at the two interfaces, (see Figures 8.5(c)-8.5(d)) which results in strong nonlocal effects seeded by the small but finite asymmetry at the interfaces. Governed by the phase-matching condition at the air-metasurface interface, guided-mode resonances excite evanescent modes that penetrate a small distance into the air (as shown in Figure 8.5(b)). On the other hand, at the metasurface-Si interface, the guided-mode resonances excite propagating modes into Si as shown in Figure 8.5(a).

8.6 Polarization independent optical diode

We also designed and experimentally characterized a polarization independent optical diode using the concept of digital metasurfaces. Asymmetric transmission of light with either of the two linear orthogonal polarization states is achieved at the digital metasurface. Figure 8.6(a) shows the scanning-electron micrograph of the fabricated metasurface composed of 4 × 4 unit cells, each of size 4 μm × 4 μm. The measured as well as simulated transmission enhancement with respect to unpatterned Si as a function of wavelength for both polarizations are shown in Figure 8.6(b). The inset in Figure 8.6(b) shows the device design (one unit cell). The simulated steady-state intensity distributions at both polarizations for the forward and the backward propagation directions at the design wavelength (1.55 μm) are shown in Figures 8.6(c)-8.6 (f). The measurements confirm extinction ratios of 10.8 dB and 9.1 dB at $\lambda = 1.55$ μm for Ex and Ey, respectively. In comparison, the simulated extinction ratios are 13.3 dB and 12.3 dB for Ex and Ey, respectively. The discrepancies between simulations and measurements are likely due to a combination of the misalignment of the polarization state and suboptimal light coupling from metasurface to the receiver. As far as we are aware, this is the first report of a device that enables polarization-independent asymmetric transmission.

8.7 Conclusion

In conclusion, we introduce the concept of digital metasurfaces, 2D devices comprised of etched discrete pixels, whose photonic functionality can be tailored via fabrication constrained numerical optimization. Specifically, we designed, fabricated and characterized digital metasurfaces to exhibit optical-diode behavior or asymmetric transmission of linearly polarized light. The digital metasurfaces have no absorption losses, are relatively easy to fabricate (CMOS compatible and require only a single lithography step), are robust to fabrication errors, and exhibit excellent transmission efficiencies, extinction ratios and operational bandwidths. Polarization-independent asymmetric transmission is also demonstrated. Enhanced light-matter interactions are achieved via a directed design of the subwavelength structures, which when combined with the interfacial asymmetries result in the optical-diode behavior. It is important to point out that our devices are completely reciprocal in the Lorentz sense [35] and therefore, cannot be used a perfect optical isolator. Nevertheless, simulations indicate that the digital metasurface has an acceptance angle as large as 15°, and therefore, could be used for optical isolation as long as the incident modes are restricted. Furthermore, such optically asymmetric devices could have important applications in filters, direction sensitive beam splitters, circulators and sensor components [36,37].

8.8 References

[1] A. S. Schwanecke, V. A. Fedotov, V. V. Khardikov, S. L. Prosvirnin, Y. Chen, and N. I. Zheludev, “Nanostructured metal film with asymmetric optical transmission,” Nano Lett. **8**(9), 2940–2943 (2008).

[2] E. Plum, V. A. Fedotov, and N. I. Zheludev, “Asymmetric transmission: a generic property of two-dimensional periodic patterns,” J. Opt. **13**(2), 024006 (2011).

[3] R. A. Shelby, D. R. Smith, and S. Schultz, “Experimental verification of a negative index of refraction,” Science **292**(5514), 77–79 (2001).

[4] M. Scalora, R. J. Flynn, S. B. Reinhardt, R. L. Fork, M. J. Bloemer, M. D. Tocci, C. M. Bowden, H. S. Ledbetter, J. M. Bendickson, J. P. Dowling, and R. P. Leavitt, “Ultrashort pulse propagation at the photonic band edge: large tunable group delay with

minimal distortion and loss," Phys. Rev. E Stat. Phys. Plasmas Fluids Relat. Interdiscip. Topics **54**(2), R1078–R1081 (1996).

[5] S. Cakmakyapan, H. Caglayan, A. E. Serebryannikov, and E. Ozbay, "Experimental validation of strong directional selectivity in nonsymmetric metallic gratings with a subwavelength slit," Appl. Phys. Lett. **98**(5), 051103 (2011).

[6] S. Cakmakyapan, A. E. Serebryannikov, H. Caglayan, and E. Ozbay, "Spoof-plasmon relevant one-way collimation and multiplexing at beaming from a slit in metallic grating," Opt. Express **20**(24), 26636–26648 (2012).

[7] A. Cicek, M. B. Yucel, O. A. Kaya, and B. Ulug, "Refraction-based photonic crystal diode," Opt. Lett. **37**(14), 2937–2939 (2012).

[8] L. Wu, Z. Yang, Y. Cheng, M. Zhao, R. Gong, Y. Zheng, J. Duan, and X. Yuan, "Giant asymmetric transmission of circular polarization in layer-by-layer chiral metamaterials," Appl. Phys. Lett. **103**(2), 021903 (2013).

[9] C. Menzel, C. Helgert, C. Rockstuhl, E. B. Kley, A. Tünnermann, T. Pertsch, and F. Lederer, "Asymmetric transmission of linearly polarized light at optical metamaterials," Phys. Rev. Lett. **104**(25), 253902 (2010).

[10] T. Xu and H. J. Lezec, "Visible-frequency asymmetric transmission devices incorporating a hyperbolic metamaterial," Nat. Commun. **5**, 4141 (2014).

[11] M. Kang, J. Chen, H. X. Cui, Y. Li, and H. T. Wang, "Asymmetric transmission for linearly polarized electromagnetic radiation," Opt. Express **19**(9), 8347–8356 (2011).

[12] M. Mutlu, A. E. Akosman, A. E. Serebryannikov, and E. Ozbay, "Diodelike asymmetric transmission of linearly polarized waves using magnetoelectric coupling and electromagnetic wave tunneling," Phys. Rev. Lett. **108**(21), 213905 (2012).

[13] A. Mandatori, M. Bertolotti, and C. Sibilia, "Asymmetric transmission of some two-dimensional photonic crystals," J. Opt. Soc. Am. B **24**(3), 685–690 (2007).

14. M. J. Lockyear, A. P. Hibbins, K. R. White, and J. R. Sambles, "One-way diffraction grating," Phys. Rev. E Stat. Nonlin. Soft Matter Phys. 74(5), 056611 (2006). [CrossRef] [PubMed]

[15] M. Stolarek, D. Yavorskiy, R. Kotyński, C. J. Zapata Rodríguez, J. Łusakowski, and T. Szoplik, "Asymmetric transmission of terahertz radiation through a double grating," Opt. Lett. **38**(6), 839–841 (2013).

[16] V. A. Fedotov, P. L. Mladyonov, S. L. Prosvirnin, A. V. Rogacheva, Y. Chen, and N. I. Zheludev, "Asymmetric propagation of electromagnetic waves through a planar chiral structure," Phys. Rev. Lett. **97**(16), 167401 (2006).

[17] A. V. Novitsky, V. M. Galynsky, and S. V. Zhukovsky, "Asymmetric transmission in planar chiral split-ring metamaterials: microscopic Lorentz-theory approach," Phys. Rev. B **86**(7), 075138 (2012).

[18] R. Singh, E. Plum, C. Menzel, C. Rockstuhl, A. K. Azad, R. A. Cheville, F. Lederer, W. Zhang, and N. I. Zheludev, "Terahertz metamaterial with asymmetric transmission," Phys. Rev. B **80**(15), 153104 (2009).

[19] L. R. Arnaut, "Chirality in multi-dimensional space with application to electromagnetic characterization of multi-dimensional chiral and semi-chiral media," J. Electromagn. Waves Appl. **11**(11), 1459–1482 (1997).

[20] S. I. Maslovski, D. K. Morits, and S. A. Tretyakov, "Symmetry and reciprocity constraints on diffraction by gratings of quasi-planar particles," J. Opt. A, Pure Appl. Opt. **11**(7), 074004 (2009).

[21] A. Papakostas, A. Potts, D. M. Bagnall, S. L. Prosvirnin, H. J. Coles, and N. I. Zheludev, "Optical manifestations of planar chirality," Phys. Rev. Lett. **90**(10), 107404 (2003).

[22] T. Vallius, K. Jefimovs, J. Turunen, P. Vahimaa, and Y. Svirko, "Optical activity in subwavelength-period arrays of chiral metallic particles," Appl. Phys. Lett. **83**(2), 234–236 (2003).

[23] A. S. Schwanecke, A. Krasavin, D. M. Bagnall, A. Potts, A. V. Zayats, and N. I. Zheludev, "Broken time reversal of light interaction with planar chiral nanostructures," Phys. Rev. Lett. **91**(24), 247404 (2003).

[24] M. Kuwata-Gonokami, N. Saito, Y. Ino, M. Kauranen, K. Jefimovs, T. Vallius, J. Turunen, and Y. Svirko, "Giant optical activity in quasi-two-dimensional planar nanostructures," Phys. Rev. Lett. **95**(22), 227401 (2005).

[25] S. Liu, M. B. Sinclair, T. S. Mahony, Y. C. Jun, S. Campione, J. Ginn, D. A. Bender, J. R. Wendt, J. F. Ihlefeld, P. G. Clem, J. B. Wright, and I. Brener, "Optical magnetic mirrors without metals," Optica **1**(4), 250–256 (2014).

[26] B. Shen, P. Wang, R. Polson, and R. Menon, "Integrated metamaterials for efficient and compact free-space-to-waveguide coupling," Opt. Express **22**(22), 27175–27182 (2014).

[27] B. Shen, P. Wang, R. Polson, and R. Menon, "Ultra-high-efficiency metamaterial polarizer," Optica **1**(5), 356–360 (2014).

[28] A. Y. Piggott, J. Lu, T. M. Babinec, K. G. Lagoudakis, J. Petykiewicz, and J. Vučković, "Inverse design and implementation of a wavelength demultiplexing grating coupler," Sci. Rep. **4**, 7210 (2014).

[29] G. Kim, J.-A. Dominguez-Caballero, H. Lee, D. J. Friedman, and R. Menon, "Increased photovoltaic power output via diffractive spectrum separation," Phys. Rev. Lett. **110**(12), 123901 (2013).

[30] G. Kim and R. Menon, "An ultra-small three dimensional computational microscope," Appl. Phys. Lett. **105**(6), 061114 (2014).

[31] B. Shen, P. Wang, R. Polson, and R. Menon, "An integrated-nanophotonics polarization beamsplitter with 2.4×2.4 μm^2 footprint," Nat. Photonics **9**(6), 378–382 (2015).

[32] P. Wang and R. Menon, "Optimization of generalized dielectric nanostructures for enhanced light trapping in thin-film photovoltaics via boosting the local density of optical states," Opt. Express **22**(S1Suppl 1), A99–A110 (2014).

[33] B. Shen, P. Wang, and R. Menon, "Optimization and analysis of 3D nanostructures for power-density enhancement in ultra-thin photovoltaics under oblique illumination," Opt. Express **22**(102), A311–A319 (2014).

[34] A. F. Oskooi, D. Roundy, M. Ibanescu, P. Bermel, J. D. Joannopoulos, and S. G. Johnson, "MEEP: A flexible free-software package for electromagnetic simulations by the FDTD method," Comput. Phys. Commun. **181**(3), 687–702 (2010).

[35] D. Jalas, A. Petrov, M. Eich, W. Freude, S. Fan, Z. Yu, R. Baets, M. Popović, A. Melloni, J. D. Joannopoulos, M. Vanwolleghem, C. R. Doerr, and H. Renner, "What is and what is not an optical isolator," Nat. Photonics **7**(8), 579–582 (2013).

[36] M. Stolarek, D. Yavorskiy, R. Kotyński, C. J. Zapata Rodríguez, J. Łusakowski, and T. Szoplik, "Asymmetric transmission of terahertz radiation through a double grating," Opt. Lett. **38**(6), 839–841 (2013).

[37] R. Singh, E. Plum, C. Menzel, C. Rockstuhl, A. K. Azad, R. A. Cheville, F. Lederer, W. Zhang, and N. I. Zheludev, "Terahertz metamaterial with asymmetric transmission," Phys. Rev. B **80**(15), 153104 (2009).

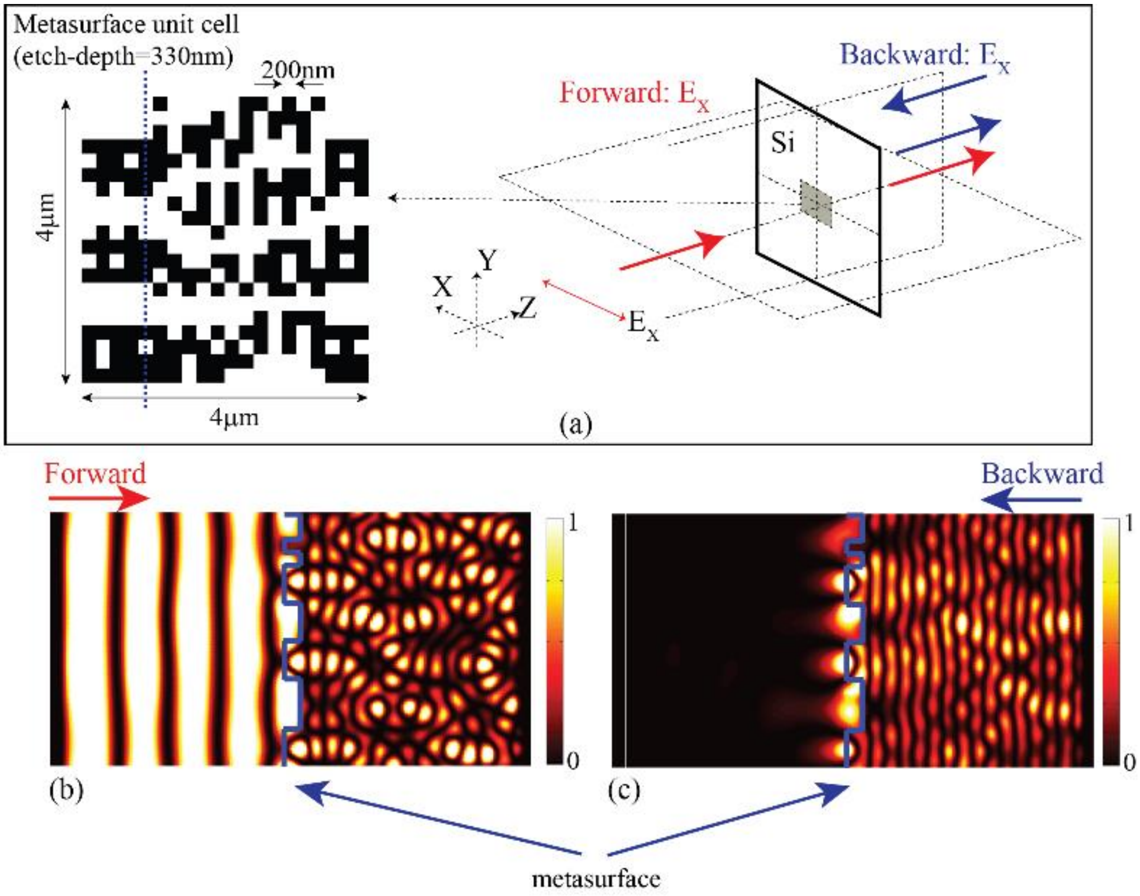

Figure 8.1. (a) Metasurface design for asymmetric transmission of linearly polarized light. The design (left) is composed of etched square pixels in silicon. Simulated steady-state intensity distributions in the YZ plane for (b) forward and (c) backward propagation directions. Blue dashed line in (a) indicates the location of the YZ cut plane. The blue solid lines in (b) and (c) indicate the location of the metasurface.

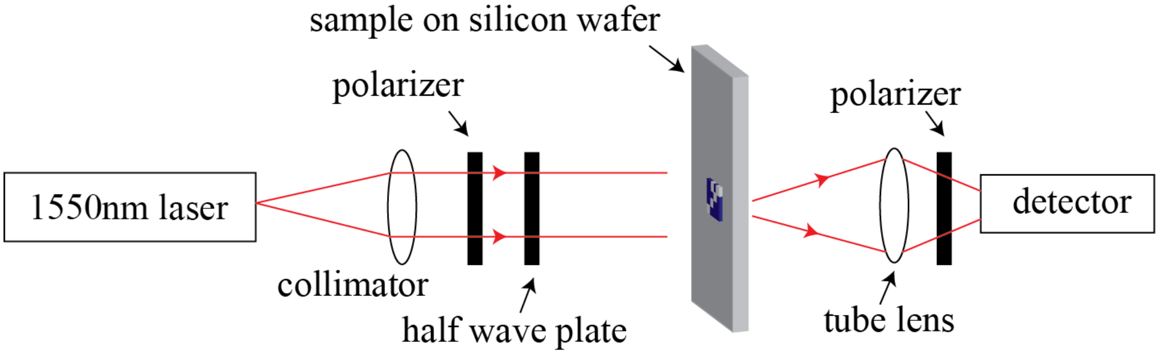

Figure 8.2. Schematic of the experimental setup for the asymmetric transmission metasurface measurements in transmission.

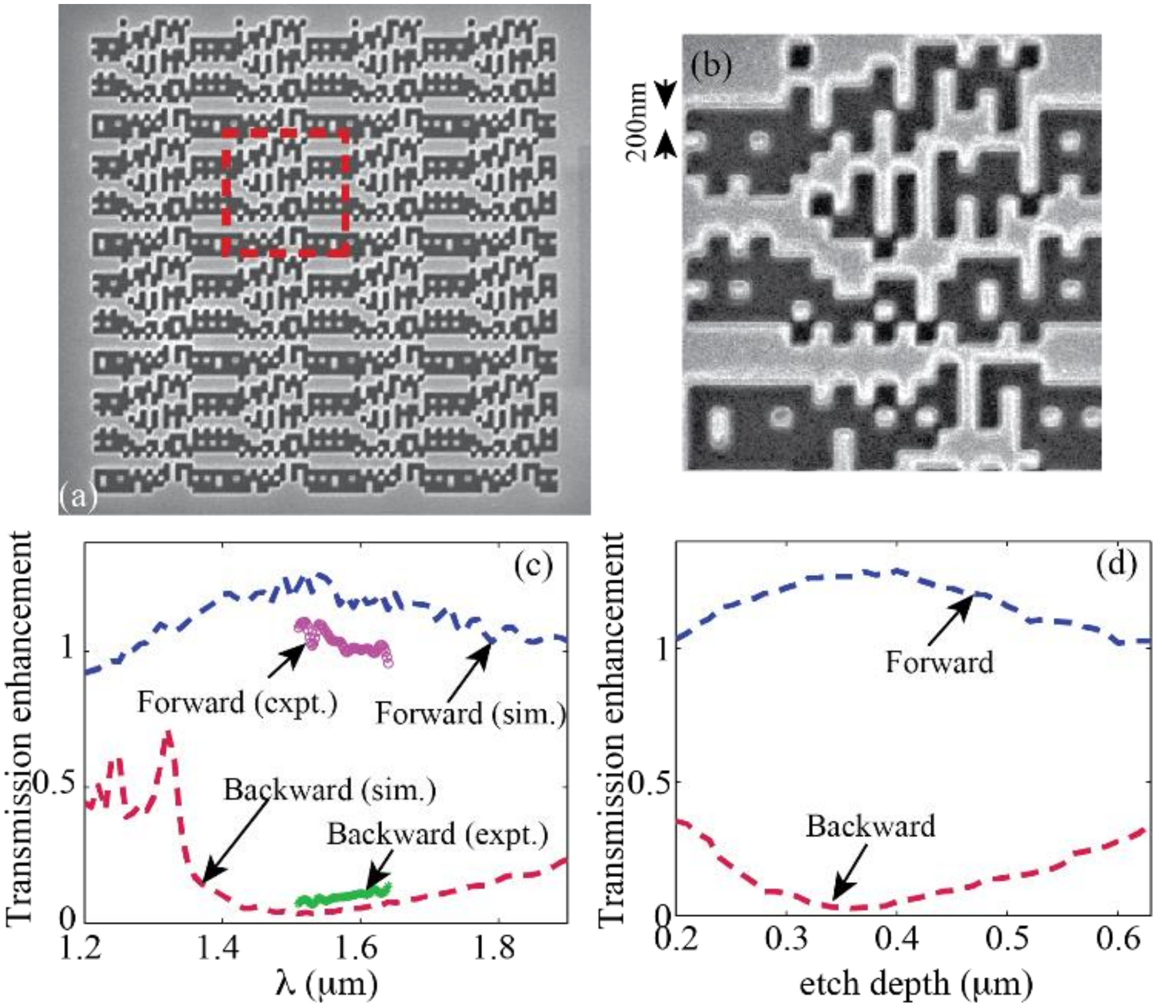

Figure 8.3. (a) Scanning-electron micrograph of the fabricated metasurface. One unit cell is 4 μm × 4 μm as shown by the red dashed lines, and the device consists of 4 × 4 unit cells. (b) Scanning-electron micrograph of one unit cell. (c) Measured and simulated transmission enhancement with respect to an unpatterned Si substrate as a function of wavelength. (d) Simulated transmission enhancement with respect to an unpatterned Si substrate as a function of the etch depth.

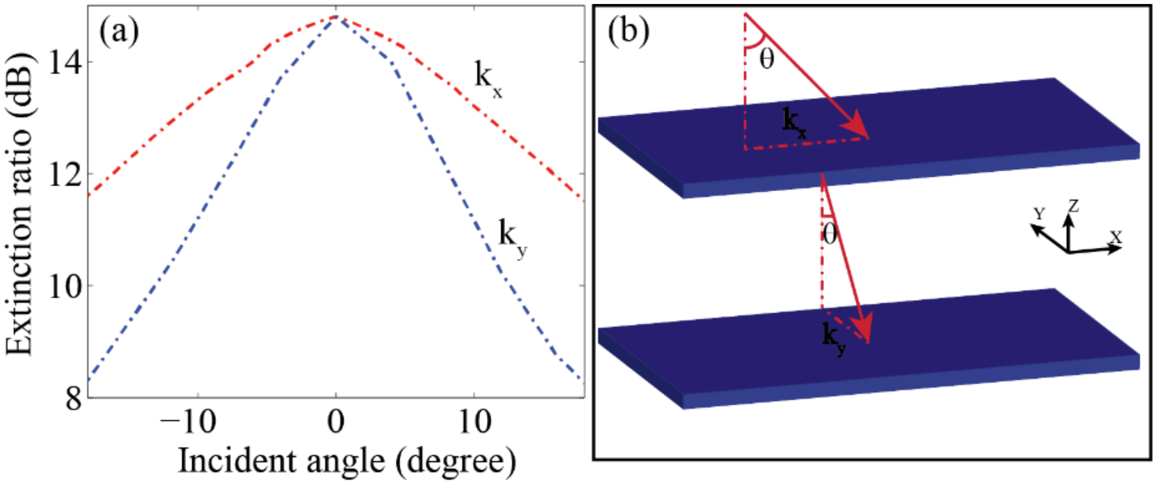

Figure 8.4. Performance analysis under oblique illumination for metasurface for linearly polarized light. (a) Extinction ratio as a function of incident angles for k_x and k_y. (b) Illustration of two types oblique illumination: k_x and k_y.

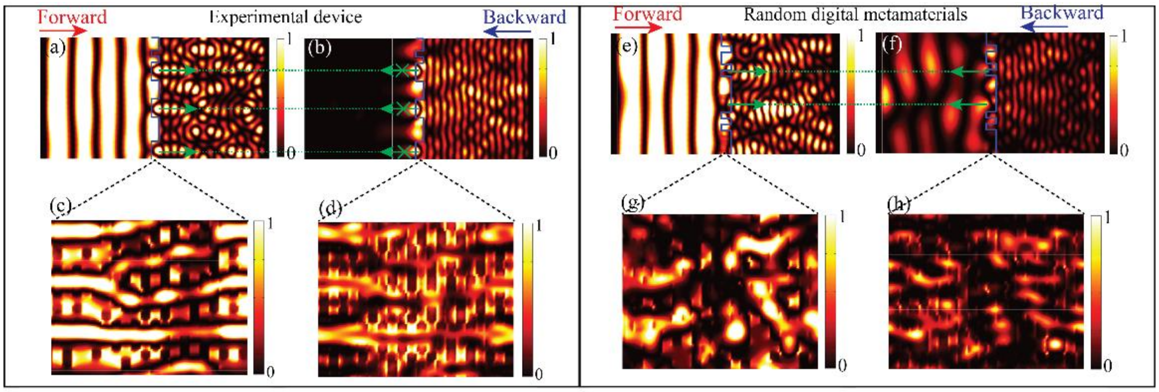

Figure 8.5. Simulated steady-state electric intensity pattern for experimental device (for linearly polarized light) and random digital metamaterials. Field pattern in YZ plane for (a) forward and (b) backward direction of experimental device. Field pattern at (c) air-metamaterial and (d) metamaterial-silicon interface (XY plane) for experimental device. Field pattern in YZ plane for (e) forward and (f) backward direction of random digital metamaterials. Field pattern in (g) air-metamaterial and (h) metamaterial-silicon interface (XY plane) for random digital metamaterials. In all the plot, Z is the light propagation direction. Green arrows indicate light propagation direction and cross at arrows means that light decays fast after the metasurface. Blue solid line indicates the epsilon distribution of the metasurface.

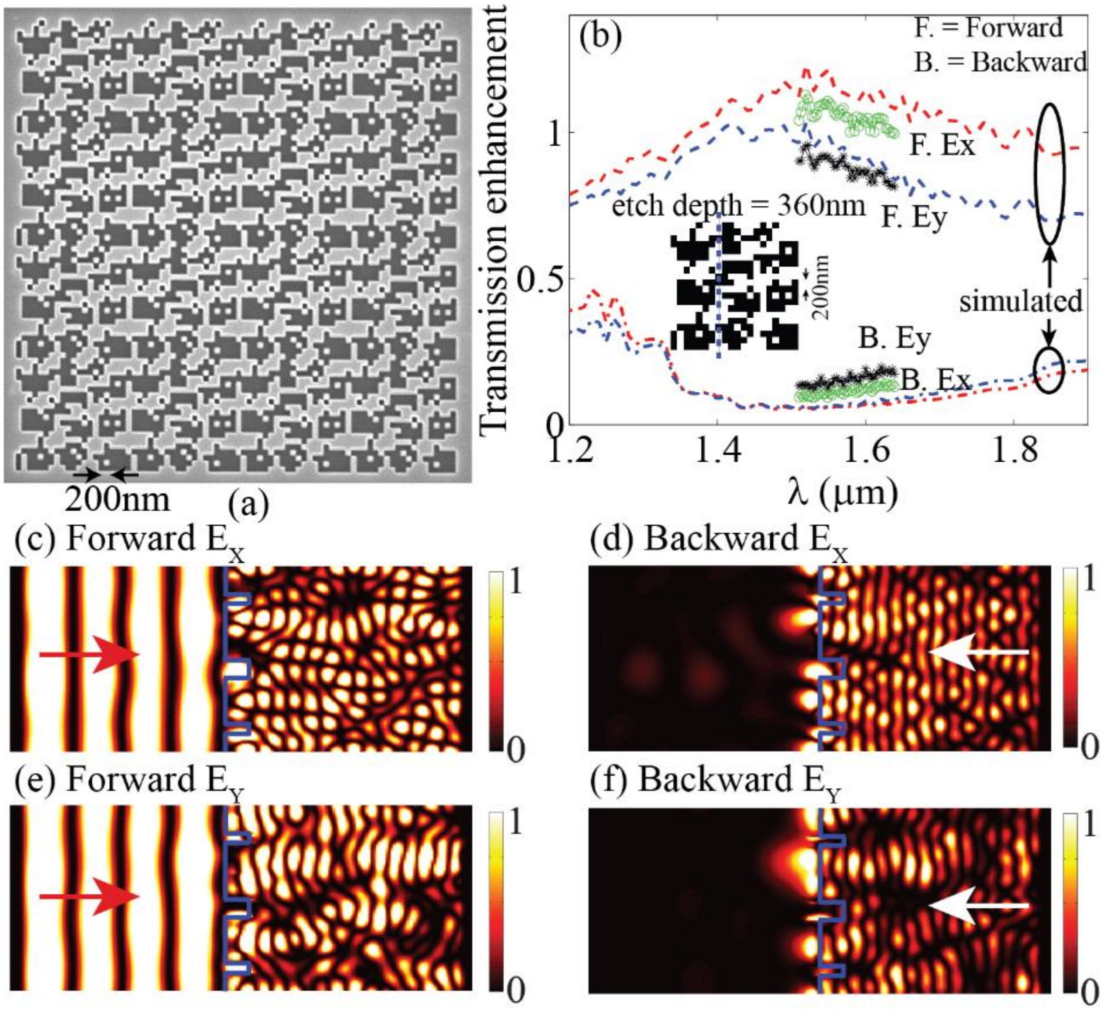

Figure 8.6. Polarization independent asymmetric transmission. (a) Scanning-electron micrograph of the fabricated digital metasurface. The fabricated device consists of 4 by 4 unit cells, each of size, 4 μm × 4 μm. (b) Measured and simulated transmission enhancement with respect to unpatterned Si as a function of wavelength. Lines with markers represent measurement data, while lines without markers represent simulation data. Red and blue lines represent the calculated transmission-enhancement spectra for Ex and Ey, respectively. Inset shows the design of the digital metasurface. (c)-(f) Simulated steady-state intensity distributions in the YZ plane of Ex and Ey polarized light in the forward and backward directions. The blue dashed line in (b) indicates the YZ cut-plane used for the simulations in (c)-(f). The blue solid lines in (c)-(f) indicate the location of the digital metasurface.

CHAPTER 9

AN ULTRA-HIGH EFFICIENCY METAMATERIAL POLARIZER

Reprinted and adapted with permission from [B. Shen, P. Wang, R. C. Polson, and R. Menon, “An ultra-high efficiency Metamaterial Polarizer,” Optica **1**(5) 356-360 (2014).].

9.1 Abstract

Conventional polarizers operate by rejecting undesired polarization, which limits their transmission efficiency to much less than 50% when illuminated by unpolarized light. We designed, fabricated, and characterized a multilevel metamaterial linear polarizer that rotates light with polarization perpendicular to its principal axis by 90 deg. Light with polarization parallel to its principal axis is transmitted undisturbed. Thereby, such a polarizer is able to output linearly polarized light from unpolarized input with a transmission efficiency that is substantially higher than the theoretical upper limit of 50%. A nonlinear optimization algorithm was used to design the polarizer, while multilevel focused-ion-beam lithography was used to fabricate it in silicon for the vacuum wavelength, λ_0 = 1550 nm. We experimentally confirmed that the fabricated device enhances the transmission of the desired linear polarization by 100% compared to an unpatterned film, corresponding to a transmission efficiency of ∼74% at the design wavelength. Since our method allows for the generalized manipulation of the amplitude, phase, and polarization of light with high transmission efficiency using ultrathin elements, it should enable the efficient generation of complex vector distributions of light.

9.2 Introduction

Manipulation of the polarization of light is extremely important for a variety of applications ranging from communications [1] to imaging [2–4]. Conventional polarization selection devices (or polarizers) use absorption or reflection to discard the unwanted polarization [5]. In these polarizers, the maximum achievable transmission efficiency of the desired polarization is 50%. Commercial polarizers typically demonstrate transmission efficiencies that are lower [6]. In this article, we apply a new approach to designing a metamaterial polarizer that rotates one polarization by 90 deg, while the orthogonal polarization is transmitted undisturbed. Thereby, such a polarizer allows for substantially higher transmission efficiencies in the desired polarization. Furthermore, we show that our design methodology is applicable to metamaterials in general, and could enable unique and diverse photonic functions in lossless dielectric substrates.

Most conventional polarizers are based upon form birefringence [7] or total internal reflection effects in crystals or polymers, which cause phase retardation between the two orthogonal polarizations. Recently, a variety of novel approaches to polarization rotation have been proposed. Some of these employ surface gratings, whose scattering vectors are different from the polarization state of the incident light to achieve polarization manipulation [8,9]. Other devices achieve polarization manipulation using metasurfaces, i.e., carefully designed antennae that impart an abrupt phase change at an interface [10-12]. An alternative approach is to use subwavelength structures to manipulate polarization across a wavefront (inhomogeneous polarization) [13]. Polarization-manipulation devices have been utilized for a variety of applications [14-17]. Recently, these ideas have been generalized by combining conventional computer-generated holography [18] with subwavelength control for manipulation of the phase, amplitude, and polarization of light [19,20]. Related work described optical transmission by reflectionless metasurfaces. Polarization rotation of zero-order transmitted light through a perforated metal film was also recently demonstrated [21]. Experimental demonstration in the microwave regime was also given [22,23]. These approaches utilize metallic antennae on a single surface, which suffer from parasitic absorption. Nevertheless, only one polarization is manipulated in all previous devices, resulting in less than 50% transmission efficiency, when illuminated by both polarizations.

In contrast, our device is based upon an all-dielectric material that is patterned at subwavelength dimensions so as to enable independent manipulation of both polarizations. To illustrate the principle, we designed, fabricated, and characterized a metamaterial polarizer that operates by allowing one polarization to transmit undisturbed while rotating the orthogonal polarization.

9.3 Methods

Our design goal is to determine the etch depth of each pixel such that a desired phase, amplitude, and polarization distribution of light is obtained upon transmission through the device. We constrained our pixel size to 200 nm × 200 nm to enable fabrication. For computational expediency, we limited the device size to 20×20 pixels, corresponding to a total dimension of 4 μm × 4 μm. Furthermore, periodic boundary conditions were applied along the X and Y directions that allowed the unit to be repeated in 2D. We also constrained the maximum aspect ratio for ease of fabrication.

The design was performed by a modified version of the direct-binary-search (DBS) algorithm. Previously, we have successfully utilized this algorithm to design nanophotonic light-trapping geometries [24,25] as well as broadband nonimaging diffractive optics [26-28]. Here, our optimization variables are the etch depths of each of the 200 nm × 200 nm pixels in our device. The algorithm attempts to maximize a figure of merit, which we define as the transmission efficiency at the desired polarization (Ex in Figure 9.1), when the polarizer is illuminated by both polarizations (Ex and Ey) with equal amplitude. The optimized design is shown on the top left of Figure 9.1(a). Although the design was performed using periodic boundary conditions, our fabricated device was composed of 4 ×

4 unit cells (total size of 16 µm × 16 µm). In other words, the polarizer was surrounded by unpatterned silicon. We simulated the performance of this fabricated device and summarized the results in Figures 9.1(b)–9.1(e). When illuminated by collimated linearly polarized light with polarization along the Y axis (Ey source), the output light intensity in Ey decreases [Figure 9.1(b)], while that in Ex increases as shown in Figure 9.1(c). In other words, the input field oriented along the Y axis after propagation through the polarizer is substantially rotated such that it is oriented along the X axis. On the other hand, when the device is illuminated with light polarized along the X axis (Ex source), it transmits mostly undisturbed as shown in Figures 9.1(d) and 9.1(e). Small perturbations of the fields in the output are due to diffraction at the boundary of the polarizer, where the periodic boundary conditions are not satisfied. Spatial nonuniformity of the transmitted fields is expected, since the unit cell does not exhibit any symmetry. We further confirmed using simulations that only 13% of the incident light is reflected, while 74% of the incident light is transmitted into the desired Ex polarization. Compared to the surrounding unpatterned silicon, the transmission of Ex is enhanced by 110%, and the ratio of the transmitted power at Ex to that at Ey at the output is calculated to be 8.8.

9.4 Experiment and results

The device was fabricated by etching into silicon using focused-ion-beam lithography using gallium ions. Different etch depths are achieved by varying the deposited energy or exposure dose at each location. Figure 9.2(a) shows the scanning-electron micrograph of a fabricated device composed of 4 × 4 unit cells, where each unit cell is 4 µm × 4 µm (denoted by dashed yellow lines). A magnified view of one unit cell in Figure 9.2(b) shows the multiple etch depths and the square pixels.

In order to characterize the polarizer, we illuminated it with collimated linearly polarized light from a 1550 nm laser (Hewlett Packard model No. 8168E). The transmitted power was measured using a lens and a photodetector from a spot of size 14 μm on the sample. A conventional polarizer was placed at the output to measure the power at the two orthogonal polarizations separately. A half-wave plate and a polarizer were used at the input to first align the direction of polarization to the Y axis of the metamaterial polarizer. Then, the device was stepped in the X–Y plane using a stage, while the photodetector registered the transmitted signal. The resulting image is shown in Figure 9.2(c). The dashed white square shows the location of the metamaterial polarizer. Behind the device, the power in the Ex polarization is dramatically increased while that in the Ey polarization is correspondingly reduced. The experiment was repeated after aligning the incident polarization to the X axis of our polarizer. As shown in Figure 9.2(c), the transmitted power is almost entirely in the Ex polarization, since the electric field oriented along the X axis is transmitted undisturbed. Figure 9.2(d) schematically compares the transmitted power between the metamaterial polarizer and unpatterned silicon. When illuminated by both polarizations, the metamaterial polarizer transmits a total of 88.8 nW in Ex compared to just 44.2 nW for unpatterned silicon. This increase is primarily due to the incident power in Ey being rotated 90 deg into Ex upon transmission. The measured results agree well with the simulated enhancement of 110%. The measured ratio of the transmitted power at Ex to that at Ey at the output is 7.8, which agrees with the simulated value of 8.8.

9.5 Discussion

It has been reported that polarization rotation occurs when the scattering vector is different from the polarization of the incident light [8,9]. The scattering structure, defined by our design, consists of a large number of locally varying scattering vectors. The scattering vectors vary with position not only in the planes perpendicular to the propagation direction but also along the propagation direction. The transmitted light after the metamaterial polarizer is the superposition of light scattered from all these elements. The optimization process is thus attempting to create a distribution of scattering vectors such that the cumulative effect after transmission is that one polarization state ($\mathrm{E}x$) is allowed to pass through with low loss, while the orthogonal polarization state ($\mathrm{E}y$) is rotated by 90 deg. We analyzed the electric fields within the device and show that the rotation of the $\mathrm{E}y$ modes is primarily due to the near-field coupling between multiple resonant-guided modes that are excited upon illumination, similar to what has been reported in photonic crystals [29,30]. By analyzing the time-averaged intensity distribution in each layer of our device, we can readily show that when illuminated by a source polarized along the Y axis, dipoles that are polarized along the X axis are excited at the corners of each isolated pillar in the first layer. Such dipoles then couple energy into the structures in the adjacent layers of the metamaterial polarizer. Eventually, the last (third) layer of the polarizer radiates energy into the far field, still maintaining the polarization along the X axis. This is further confirmed by analyzing the time-dependent field variation in the X–Z and Y–Z planes in the vicinity of the hot.

It is interesting to note that there is an apparent decrease in entropy due to the conversion of randomly polarized input light into linearly polarized output with high efficiency [31]. This is not really true, since the decrease of the polarization degree of freedom is accompanied by a larger increase in the spatial frequencies of the output wavefront. In other words, although the incident light is collimated, the transmitted light radiates in multiple directions.

We also performed careful analysis of the tolerance of the metamaterial polarizer to fabrication errors. We show that the devices are robust to fabrication errors corresponding to about 8% of the pixel size. Small slopes in the sidewalls of the pixels also introduce only minor changes to the performance of the device. Although our device was designed for a single wavelength, we calculated the bandwidth to be ~ 20 nm. By incorporating a broadband source during design, it is possible to increase the device bandwidth further.

In order to ensure ease of fabrication, we applied a constraint on the maximum aspect ratio (defined as the ratio of the maximum etch depth to the pixel size). For the fabricated device, the maximum aspect ratio was 2.6. We performed a series of designs with higher maximum aspect ratios and realized that the performance of the device can be enhanced. Figure 9.3(a) shows the transmission efficiency at Ex and the selection ratio (power in Ex to power in Ey) as a function of the maximum aspect ratio. As the aspect ratio is increased, the transmission efficiency at Ex under unpolarized input can increase to almost 80%. The design for a maximum aspect ratio of 5.7 is shown in Figure 9.3(b). The simulated electric-field distributions in the X–Z and Y–Z planes after transmission through the metamaterial polarizer are shown in Figures 9.3(c) and 9.3(d) for the Ex source, and in Figures 9.3(e) and 9.3(f) for the Ey source. Figures 9.3(c) and 9.3(e) show the electric-field distributions polarized along X, while Figures 9.3(d) and 9.3(f) show the electric-field distributions polarized along Y. As expected, the polarizer rotates the incident Ey fields into Ex at the output, while the incident Ex fields transmit undisturbed. Note that no attempt was made to control amplitude in this case, and, hence, the transmitted intensity shows nonuniformity in the X-Y plane.

As we mentioned earlier, our design can be extended to control the phase, amplitude, and polarization of light. To demonstrate this capability, we designed a device that spatially separates and localizes fields according to their polarization in the plane normal to the direction of propagation. In order to simplify the computation, this device was designed in 2D, and the optimized design is illustrated in Figure 9.3(g). When this device is illuminated by an unpolarized source from above propagating from top to bottom, the electric fields are spatially separated along the X axis as shown by the intensity distributions in Figure 9.3(h). The input field was uniform along the X axis for both polarizations. However, at the output, Ex becomes confined to a 0.45-μm-wide region on the left half (red line), while Ey is confined to a 0.44-μm-wide region on the right half (blue line). Note that this polarization separation is achieved within a propagation distance of only 1500 nm (less than the free-space wavelength of 1550 nm).

9.6 Conclusion

We designed, fabricated, and characterized a new metamaterial polarizer that rotates one polarization by 90 deg, while allowing the orthogonal polarization to transmit unperturbed. We experimentally showed that this polarizer is able to enhance the transmission of one polarization by 100% compared to an unpatterned film. Appropriate design of these devices can achieve absolute transmission efficiencies at one desired polarization of almost 80% at the design wavelength (1.55 μm). Our approach is readily generalized to manipulate the phase, amplitude, and polarization state of electromagnetic fields at the subwavelength scale. The demonstrated device could have significant implications in imaging systems and displays (when extended to visible wavelengths). Although the extinction ratio for our device is smaller than conventional polarizers, the metamaterial polarizer could be useful where transmission efficiency is particularly important. Other interesting applications include the ability to efficiently generate complex modes that may be useful in quantum entanglement [32] and expanded bandwidth in telecommunications [33].

9.7 References

[1] J. N. Damask, *Polarization Optics in Telecommunications* (Springer, 2004).

[2] D. S. Kliger, J. W. Lewis, and C. E. Randall, *Polarized Light in Optics and Spectroscopy* (Academic, 1990).

[3] V. V. Tuchin, L. V. Wang, and D. A. Zimnyako, *Optical Polarization in Biomedical Applications* (Springer, 2006).

[4] Y. P. Svirko and N. I. Zheludev, *Polarization of Light in Nonlinear Optics* (Wiley, 1998).

[5] S. W. Ahn, K. D. Lee, J. S. Kim, S. H. Kim, J. D. Park, S. H. Lee, and P. W. Yoon, "Fabrication of a 50 nm half-pitch wire grid polarizer using nanoimprint lithography," Nanotechnology **16**, 1874–1877 (2005).

[6] Commercial polarizers in Thorlabs, http://www.thorlabs.us/newgrouppage9.cfm?objectgroup_id=4984.

[7] R. C. Tyan, A. A. Salvekar, H. P. Chou, C. C. Cheng, A. Scherer, P. C. Sun, F. Xu, and Y. Fainman, "Design, fabrication, and characterization of form-birefringent multilayer polarizing beam splitter," J. Opt. Soc. Am. A **14**, 1627–1636 (1997).

[8] N. K. Grady, J. E. Heyes, D. R. Chowdhury, Y. Zeng, M. T. Reiten, A. K. Azad, A. J. Taylor, D. A. R. Dalvit, and H. T. Chen, "Terahertz metamaterials for linear polarization conversion and anomalous refraction," Science **340**, 1304–1307 (2013).

[9] J. Elliott, I. I. Smolyaninov, N. I. Zheludev, and A. V. Zayats, "Polarization control of optical transmission of a periodic array of elliptical nanoholes in a metal film," Opt. Lett. **29**, 1414–1416 (2004).

[10] Y. N. Fang, P. Genevet, M. A. Kats, F. Aieta, J. P. Tetienne, F. Capasso, and Z. Gaburro, "Light propagation with phase discontinuities: generalized laws of reflection and refraction," Science **334**, 333–337 (2011).

[11] F. Aieta, P. Genevet, N. Yu, M. A. Kats, Z. Gaburro, and F. Capasso, "Out-of-plane

reflection and refraction of light by anisotropic optical antenna metasurfaces with phase discontinuities," Nano Lett. **12**, 1702–1706 (2012).

[12] N. Yu, F. Aieta, P. Genevet, M. A. Kats, Z. Gaburro, and F. Capasso, "A broadband, background-free quarter-wave plate based on plasmonic metasurfaces," Nano Lett. 12, 6328–6333 (2012).

[13] S. Pancharatnam, "Generalized theory of interference, and its applications," Proc. Ind. Acad. Sci. A **44**, 247–262 (1956).

[14] A. Niv, G. Biener, V. Kleiner, and E. Hasman, "Spiral phase elements obtained by use of discrete space-variant subwavelength gratings," Opt. Commun. **251**, 306–314 (2005).

[15] A. Niv, G. Biener, V. Kleiner, and E. Hasman, "Propagation-invariant vectorial Bessel beams obtained by use of quantized Pancharatnam–Berry phase optical elements," Opt. Lett. **29**, 238–240 (2004).

[16] G. Biener, A. Niv, V. Kleiner, and E. Hasman, "Geometrical phase image encryption obtained with space-variant subwavelength grating," Opt. Lett. **30**, 1096–1098 (2005).

[17] G. Biener, A. Niv, V. Kleiner, and E. Hasman, "Near-field Fourier transform polarimetry by use of a quantized space-variant subwavelength grating," J. Opt. Soc. Am. A **20**, 1940–1948 (2003).

[18] P. Hariharan, *Optical Holography: Principles, Techniques and Applications* (Cambridge University, 1996).

[19] J. Lin, P. Genevet, M. A. Kats, N. Antoniou, and F. Capasso, "Nanostructured holograms for broadband manipulation of vector beams," Nano Lett. **13**, 4269–4274 (2013).

[20] X. Ni, A. V. Kildishev, and V. M. Shalaev, "Metasurface holograms for visible light," Nat. Commun. **4**, 1–6 (2013).

[21] S. Wu, Z. Zhang, Y. Zhang, K. Zhang, L. Zhou, X. Zhang, and Y. Y. Zhu, "Enhanced rotation of the polarization of a light beam transmitted through a silver film with an array of perforated S-shaped holes," Phys. Rev. Lett. **110**, 207401 (2013).

[22] C. Pfeiffer and A. Grbic, "Metamaterial Huygens' surfaces: tailoring wave fronts with reflectionless sheets," Phys. Rev. Lett. **110**, 197401 (2013).

[23] F. Monticone, N. M. Estakhri, and A. Alu, "Full control of nanoscale optical transmission with a composite metascreen," Phys. Rev. Lett. **110**, 203903 (2013).

[24] P. Wang and R. Menon, "Optimization of generalized dielectric nanostructures for enhanced light trapping in thin-film photovoltaics via boosting the local density of optical states," Opt. Express **22**, A99–A110 (2014).

[25] P. Wang and R. Menon, "Optimization of periodic nanostructures for enhanced light-trapping in ultra-thin photovoltaics," Opt. Express **21**, 6274–6285 (2013).

[26] G. Kim, J. A. Dominguez-Caballero, and R. Menon, "Design and analysis of multi-wavelength diffractive optics," Opt. Express **20**, 2814–2823 (2012).

[27] G. Kim, J. A. Dominguez-Caballero, H. Lee, D. Friedman, and R. Menon, "Increased photovoltaic power output via diffractive spectrum separation," Phys. Rev. Lett. **110**, 123901 (2013).

[28] P. Wang and R. Menon, "Three-dimensional lithography via digital holography," in Frontiers in Optics 2012/Laser Science XXVIII, OSA Technical Digest (online) (Optical Society of America, 2012), paper FTu3A.4.

[29] V. Liu, D. A. B. Miller, and S. Fan, "Ultra-compact photonic crystal waveguide spatial mode converter and its connection to the optical diode effect," Opt. Express **20**, 28388–28397 (2012).

[30] J. Lu and J. Vučković, "Objective-first design of high-efficiency, small-footprint couplers between arbitrary nanophotonic waveguide modes," Opt. Express **20**, 7221–7236 (2012).

[31] C. Brosseau, *Fundamentals of Polarized Light: A Statistical Optics Approach* (Wiley, 1998).

[32] S. Franke-Arnold, L. Allen, and M. Padgett, "Advances in optical angular momentum," Laser Photonics Rev. **2**, 299–313 (2008).

[33] N. Bozinovic, Y. Yue, Y. Ren, M. Tur, P. Kristensen, H. Huang, A. E. Willner, and S. Ramachandran, "Terabit-scale orbital angular momentum mode division multiplexing in fibers," Science **340**, 1545–1548 (2013).

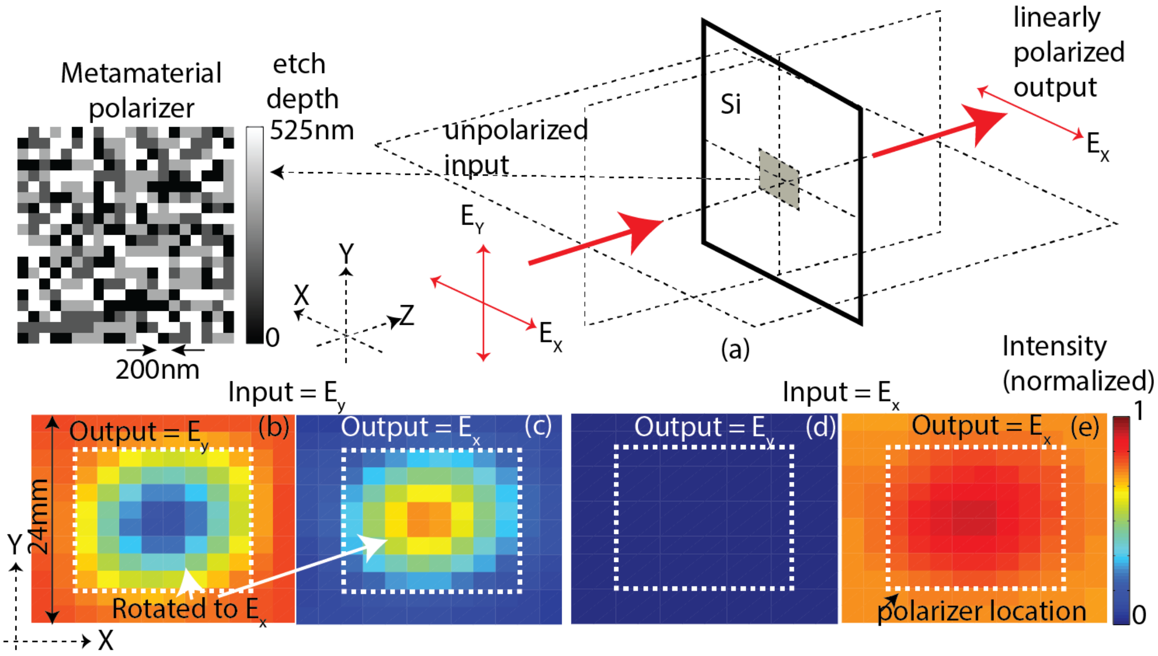

Figure 9.1. (a) High-efficiency metamaterial polarizer. The design (left) is composed of etched square pixels in silicon. (b)–(e) Simulated light intensity distributions after transmission through the polarizer for (b) Ey and (c) Ex under Ey input and for (d) Ey and (e) Ex for Ex input. The white dashed lines in (b)–(e) indicate the boundaries of the finite device.

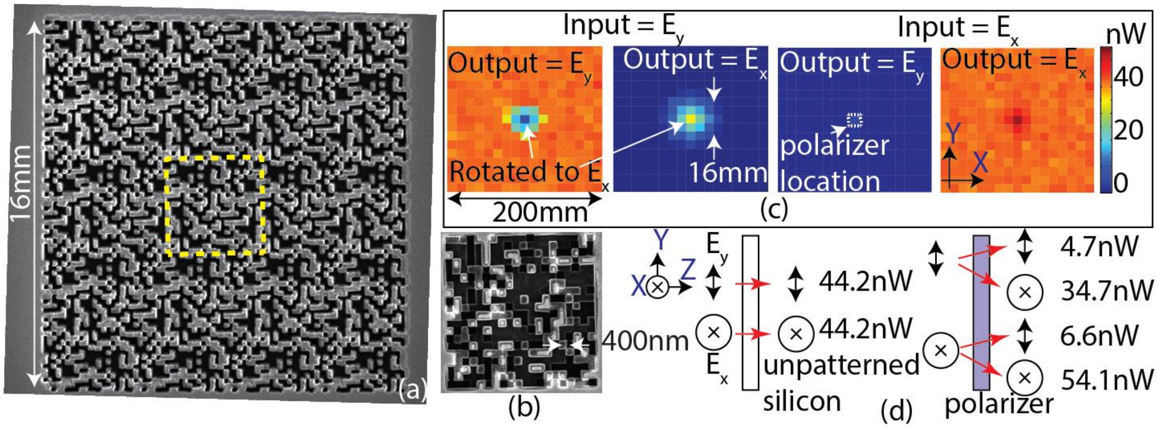

Figure 9.2. (a) Scanning-electron micrograph of the metamaterial polarizer. One unit cell is 4 µm × 4 µm (yellow dashed lines). (b) Magnified view shows pixels with a period of 400 nm. (c) Measured transmitted power as a function of position in the X–Y plane. The left two images correspond to the Ey source, while the right two images correspond to the Ex source. Within the device area (dashed white square), Ey is rotated to Ex. (d) Comparison of the measured peak transmitted power in Ex and Ey between unpatterned silicon and the metamaterial polarizer.

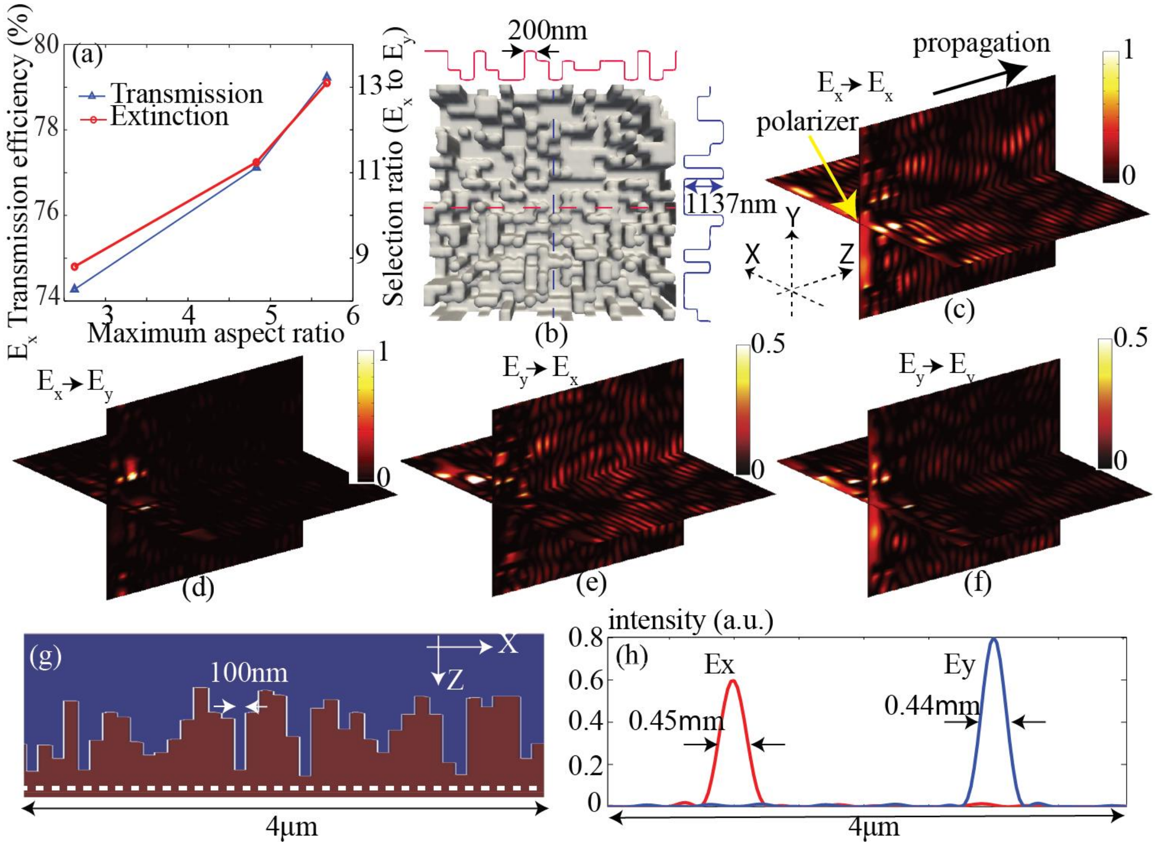

Figure 9.3. (a) Transmission efficiency (at E_x) and selection ratio (power in E_x to power in E_y) as a function of maximum aspect ratio. (b) Device with transmission efficiency of 80% and maximum aspect ratio of 5.7. (c)-(f) Time-averaged intensity distributions after the device for (c), (d) E_x source and (e), (f) E_y source. The polarizer is located in the X-Y plane at the left edge. (g) 2D device designed for polarization separation and focusing. (h) Intensity distribution along the dashed white line in (g) when the device is illuminated by E_x and E_y simultaneously.

CHAPTER 10

CONCLUSION

10.1 Summary of previous work

Digital metamaterials based integrated/free-space devices are designed and experimentally demonstrated in this dissertation. Via introducing the concept of digital metamaterials, the optical devices of interest are discretized into hundreds of pixels, each sized ~100 nm. For each pixel there can be two possible states: silicon denoted as “1” and air where silicon is etched away and denoted as “0.” As a result, a particular device design can be exclusively represented by a binary sequence, and a computational method is used to find the particular binary sequence offering the best performance. The basic premise of this approach is that, via nanofabrication, one can control the local refractive index of the device. By spatial engineering of the refractive index, it is possible to design devices with better performance or novel functions that are otherwise impossible.

Applying the algorithm mentioned above, we have experimentally demonstrated a library of passive silicon based integrated devices. In addition, free-space silicon based devices are demonstrated as well. Particularly, we have demonstrated digital metamaterials based free-space to waveguide couplers. One coupler offers an ultra-high coupling efficiency without back-reflector. Another coupler offers two functions simultaneously, including mode-conversion and light coupling which downscales the footprint. The last coupler works simultaneously as a polarization splitter and a light coupler. In addition, we have also demonstrated an integrated diode with footprint 3 × 3 μm^2 with comparable, if not higher than, transmission and extinction ratios, when compared to alternatives. An integrated polarization beamsplitter with footprint 2.4 × 2.4 μm^2 is also demonstrated. Waveguide bends that redirecting light by 180 deg with simulated transmission efficiency approaching 90% is demonstrated as well. It offers a high transmission as well as an compact footprint. The last integrated device we have demonstrated is a metamaterial cloak that enables the neighboring devices to be invisible to each other and therefore enhances the integration density of PICs.

We have also demonstrated a few free-space optical components applying the concept of digital metamaterials. A high-efficiency metamaterial free-space polarizer is demonstrated. The polarizer works to allow the desired polarization state to transmit efficiently while recycling the orthogonal polarization state via a 90 deg rotation of the error polarization state. In addition, a metasurface offering unidirectional transmission is also demonstrated. Such free-space devices offer a better performance, compact footprint, or unique functions when compared to their alternatives.

10.2 Future work

As mentioned earlier, our previous work is focused on passive optical devices since they are relatively easy to fabricate and design. However, the area of active devices is equally, if not even more, interesting to explore. Our future work mainly lies in investigating the application of digital metamaterials in active integrated optical devices. In the current stage, we are more focused on silicon based modulators and switches. Carrier injection induced refractive index change in silicon is employed to achieve the switch between on and off states.

10.2.1 Silicon modulator

In the past few decades, silicon has proven to be an ideal platform for photonic chips due to its negligible absorption in the wavelength for data communication and compatibility with the CMOS process. A lot of silicon based integrated devices have been demonstrated including interferometer [1,2], polarization splitter and rotator [3,4], grating coupler [5,6] etc. However, the silicon modulator has long been a problem due to its negligible absorption and therefore shallow modulation depth. Previous versions of the on-chip modulator are based on III-V materials and wafer-bonding to the silicon wafer. Direct deposition of III-V materials on silicon is a problem due to the large lattice mismatch between the two crystals. A complicated fabrication procedure and precise alignment is required in the wafer-bonding.

The first integrated silicon modulator was demonstrated in 2005 by Xu et al. [7]. It was based on microring resonators to enhance the absorption length and thus offered considerable modulation depth. However, one problem associated with microring resonators based on a silicon modulator is their ultra-small bandwidth and sensitivity to wavelength shift. For the modulator mentioned here, the bandwidth is less than 1 nm, which requires a complicated drive to stabilize the system. Here, we show that we can possibly achieve a broadband integrated silicon modulator employing the concept of digital metamaterials.

The design for the digital metamaterials based silicon modulator is shown in Figure 10.1. The device is designed so that light is transmitted efficiently under no voltage bias while totally blocked with voltage bias. The refractive contrast is assumed to be 1×10^{-2}, which is a little larger than the refractive contrast ever experimentally demonstrated. The simulated extinction ratio is larger 10 dB and the insertion loss is approaching -0.97 dB. Perhaps the most obvious significance of the device is its potential ultra-large bandwidth that is tens of nanometers, while the microring based silicon modulator is less than 1 nm. The future work lies in developing a process to achieve a large refractive index with carrier injection in silicon that is approaching our desired value. In addition, a doping process in silicon should also be optimized to achieve the designed transmission and extinction ratio.

10.2.2 Switch

With the desire to increase capacity of data communication, a multichannel switch with less insertion loss is needed. Currently, hundreds of channels are desired. However, with the increasing number of channels, insertion loss is increased exponentially. Seok et al. proposed broadband digital silicon photonic switches with vertical adiabatic couplers, which minimize the insertion loss via mechanically lifting waveguides to avoid the loss at waveguide crossing [8]. An insertion loss as low as 3.7 dB is experimentally observed in a 64 × 64 switch. However, a complicated fabrication procedure and precise alignment is required. For our case, we proposed a switch based on a photo-switchable molecule we used in our lab. It is totally transparent to one wavelength while opaque to the other wavelength. As a result, we may use one of the wavelengths as the signal carrier and the other wavelength as the control signal, which is actually all-optical switch free from the complex and bulky electrical components. The insertion loss is expected to be ultralow since the absorption of the photochromic material in the transparent state is negligible. An ultraefficient all-optical switch can be envisioned in this way.

10.3 Reference

[1] G. Yurtsever, B. Považay, A. Alex, B. Zabihian, W. Drexler, and R. Baets, “Photonic integrated Mach-Zehnder interferometer with an on-chip reference arm for optical coherence tomography,” Biomed. Opt. Express **5**(4), 1050–1061 (2014).

[2] C. DeRose, D. Trotter, W. Zortman, and M. Watts, “High speed travelling wave carrier depletion silicon Mach-Zehnder modulator,” in *Optical Interconnects Conference*, (IEEE, 2012), pp. 135–136.

[3] Y. Ding, L. Liu, C. Peucheret, and H. Ou, “Fabrication tolerant polarization splitter and rotator based on a tapered directional coupler,” Opt. Express **20**(18), 20021–20027 (2012).

[4] D. H. Kwon and D. H. Werner, “Polarization splitter and polarization rotator designs based on transformation optics,” Opt. Express **16**(23), 18731–18738 (2008).

[5] D. Taillaert, W. Bogaerts, P. Bienstman, D. D. Zutter, and R. Baets, “An out-of-plane grating coupler for efficient butt-coupling from photonic crystal waveguides to single-mode fibers,” IEEE J. Quantum Electron. **38**, 949 (2002).

[6] D. Taillaert, F. Van Laere, M. Ayre, W. Bogaerts, D. Van Thourhout, P. Bienstman, and R. Baets, “Grating couplers for coupling between optical fibers and nanophotonic waveguides,” Jap. J. Appl. Phys. **45**, 6071–6077 (2006).

[7] Q. Xu, B. Schmidt, S. Pradhan, and M. Lipson, “Micrometre-scale silicon electro-optic modulator,” Nature **435**,325–327 (2005).

[8] T. J. Seok, N. Quack, S. Han, R. S. Muller, and M. C. Wu, “Large-scale broadband digital silicon photonic switches with vertical adiabatic couplers,” Optica **3**(1), 64–70 (2016).

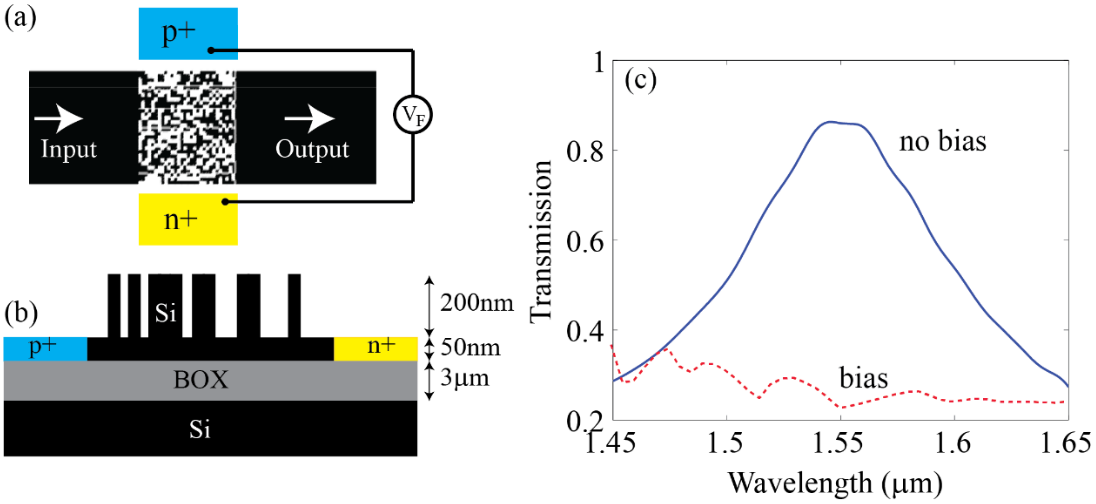

Figure 10.1. Silicon based modulator. (a) Schematic layout of the silicon modulator. (b) Cross-section of the nanostructure. (e) Simulated transmission spectra.